

NORTHROP TECHNICAL REPORT

ANALYSIS OF POROUS LAMINATES IN THE PRESENCE OF  
PLY DROP-OFFS AND FASTENER HOLES

CONTRACT N00019-82-C-0156  
CONTRACT N00019-82-C-0063

FINAL TECHNICAL REPORT

D. F. Adams  
R. L. Ramkumar  
D. E. Walrath

May 1984

Prepared for:

DEPARTMENT OF THE NAVY  
NAVAL AIR SYSTEMS COMMAND  
WASHINGTON, DC 20361

DEPARTMENT OF DEFENSE  
PLASTICS TECHNICAL EVALUATION CENTER  
ARRADCOM, DOVER, N. J. 07801

Northrop Corporation  
Aircraft Division  
One Northrop Avenue  
Hawthorne, California 90250

and

University of Wyoming  
Composite Materials Research Group  
Mechanical Engineering Department  
Laramie, Wyoming 82071

NORTHROP TECHNICAL REPORT

Approved for Public Release; Distribution Unlimited

DTIC QUALITY INSPECTED 1

PLASTED  
11/16/88

19960319 134

# DISCLAIMER NOTICE



**THIS DOCUMENT IS BEST QUALITY AVAILABLE. THE COPY FURNISHED TO DTIC CONTAINED A SIGNIFICANT NUMBER OF PAGES WHICH DO NOT REPRODUCE LEGIBLY.**

Unclassified

SECURITY CLASSIFICATION OF THIS PAGE

## REPORT DOCUMENTATION PAGE

|  |       |  |   |                    |
|--|-------|--|---|--------------------|
| 1a. REPORT SECURITY CLASSIFICATION<br>Unclassified   |       |  | 1b. RESTRICTIVE MARKINGS  |                    |
| 2a. SECURITY CLASSIFICATION AUTHORITY  |       |  | 3. DISTRIBUTION/AVAILABILITY OF REPORT<br>Approved for public release;<br>distribution unlimited  |                    |
| 2b. DECLASSIFICATION/DOWNGRADING SCHEDULE  |       |  |   |                    |
| 4. PERFORMING ORGANIZATION REPORT NUMBER(S)<br>NOR 84-113  |       |  | 5. MONITORING ORGANIZATION REPORT NUMBER(S)   |                    |
| 6a. NAME OF PERFORMING ORGANIZATION<br>University of Wyoming<br>College of Engineering   |       | 6b. OFFICE SYMBOL<br>(If applicable)                           | 7a. NAME OF MONITORING ORGANIZATION<br>Department of the Navy<br>Naval Air Systems Command (AIR 5304-C)                                 |                    |
| 6c. ADDRESS (City, State and ZIP Code)<br>University Station, Box 3295<br>Washington, D.C. 20361   |       |  | 7b. ADDRESS (City, State and ZIP Code)<br>Washington, D.C. 20361  |                    |
| 8a. NAME OF FUNDING/SPONSORING ORGANIZATION  |       | 8b. OFFICE SYMBOL<br>(If applicable)                           | 9. PROCUREMENT INSTRUMENT IDENTIFICATION NUMBER<br>N00019-82-C-0063<br>N0019-82-C-0156  |                    |
| 8c. ADDRESS (City, State and ZIP Code)   |       |  | 10. SOURCE OF FUNDING NOS.  |                    |
| 11. TITLE (Include Security Classification) Analysis of Porous Laminates in the Presence of Ply Drop-Offs and Fastener Holes (Unclassified)<br>12. PERSONAL AUTHOR(S) D. F. Adams, R. L. Ramkumar and D. E. Walrath  |       |  | PROGRAM ELEMENT NO.   |                    |
|  |       |  | PROJECT NO.   |                    |
| 13a. TYPE OF REPORT Final<br>Technical Report  |       |  | 13b. TIME COVERED<br>FROM June 82 TO May 84   |                    |
| 14. DATE OF REPORT (Yr., Mo., Day)<br>May 1984   |       |  | 15. PAGE COUNT<br>129   |                    |
| 16. SUPPLEMENTARY NOTATION   |       |  |   |                    |
| 17. COSATI CODES   |       |  | 18. SUBJECT TERMS (Continue on reverse if necessary and identify by block number)   |                    |
| FIELD  | GROUP | SUB. GR.   | Finite element analysis; porosity; ply drop-off; fastener holes; environmental effects; 2-D and 3-D elements; AS1/3501-6 graphite/epoxy |                    |
|  |       |  |   |                    |
| 19. ABSTRACT (Continue on reverse if necessary and identify by block number)   |       |  |   |                    |
| <p>Finite element analyses were carried out to predict the effects of microporosity, ply drop-offs and fastener holes on the compression behavior of AS1/3501-6 graphite/epoxy laminates. Both two dimensional (2-D) and three dimensional (3-D) analyses were performed. The validity of the analyses were established by comparing their predictions with available experimental results. The analysis of the ply drop-offs predicted little influence of their presence on the compressive strength. It also predicted that the laminate containing the 0° ply drop-offs should have about the same compressive strength in either the room temperature wet or dry states, which was also correlated experimentally. Likewise, the predicted strength reduction due to the presence of a circular hole in a specific laminate correlated well with available experimental data.</p> |       |  |   |                    |
| 20. DISTRIBUTION/AVAILABILITY OF ABSTRACT<br>UNCLASSIFIED/UNLIMITED <input checked="" type="checkbox"/> SAME AS RPT. <input type="checkbox"/> DTIC USERS <input type="checkbox"/>  |       |  | 21. ABSTRACT SECURITY CLASSIFICATION<br>Unclassified  |                    |
| 22a. NAME OF RESPONSIBLE INDIVIDUAL<br>D. F. Adams   |       | 22b. TELEPHONE NUMBER<br>(Include Area Code)<br>(307) 766-2371 |   | 22c. OFFICE SYMBOL |

SECURITY CLASSIFICATION OF THIS PAGE

19. ABSTRACT (Continued)

The analysis of microporosity was perhaps the most interesting of all. It permitted a 2-D analysis, and hence a very refined grid representation, and also crack initiation and propagation. Thus, it was a very physically realistic model. Only one assumed micropore geometry was studied here, as a demonstration of feasibility. Yet the predicted loss of transverse strength due to porosity correlated with the measured response very well. Neither the analysis nor available experimental data indicated a loss of longitudinal shear strength due to porosity.

In summary, acknowledging that additional developmental analytical work needs to be done, the preliminary results presented here clearly indicate the value of existing analytical tools in understanding the response of composites to variations of geometry, loading, and environment.

## TABLE OF CONTENTS

| <u>SECTION</u> |   | <u>PAGE</u> |
|----------------|---|-------------|
| 1              | INTRODUCTION.....                               | 1           |
| 2              | SUMMARY.....                                    | 4           |
| 3              | SYNOPSIS OF PRIOR WORK.....                     | 6           |
|                | 3.1 Micromechanics Analyses.....                | 7           |
|                | 3.2 Laminate Analyses.....                      | 8           |
|                | 3.3 Ply Drop-Off Analyses.....                  | 9           |
| 4              | CONSTITUENT AND LAMINA MATERIAL PROPERTIES..... | 11          |
|                | 4.1 Micromechanics Analysis.....                | 11          |
|                | 4.2 Constituent Properties.....                 | 13          |
|                | 4.3 Lamina Material Properties.....             | 17          |
|                | 4.4 Effective Stress-Strain Behavior.....       | 29          |
|                | 4.5 Summary.....                                | 40          |
| 5              | MICROMECHANICAL ANALYSIS OF POROSITY.....       | 42          |
|                | 5.1 2-D Analysis Capabilities.....              | 42          |
|                | 5.2 Porosity Model.....                         | 42          |
|                | 5.3 Predicted Response.....                     | 44          |
|                | 5.3.1 Longitudinal Tension.....                 | 46          |
|                | 5.3.2 Transverse Tension.....                   | 53          |
|                | 5.3.3 Longitudinal Shear.....                   | 57          |
|                | 5.4 Discussion.....                             | 63          |
| 6              | LAMINATE WITH PLY DROP-OFFS.....                | 64          |
|                | 6.1 Analysis Capabilities.....                  | 64          |
|                | 6.2 Finite Element Model.....                   | 64          |
|                | 6.3 Predicted In-Plane Stresses.....            | 67          |
|                | 6.3.1 Cooldown Thermal Residual Stresses.....   | 67          |
|                | 6.3.2 Moisture-Induced Stresses.....            | 74          |
|                | 6.3.3 Axial Compressive Loading.....            | 78          |
|                | 6.3.3.1 Room Temperature, Dry Condition.....    | 78          |
|                | 6.3.3.2 Room Temperature, Wet Condition.....    | 83          |

|    |         |   |     |
|----|---------|---|-----|
|    | 6.4     | Interlaminar Stresses.....                              | 88  |
| 7  |         | LAMINATE CONTAINING A HOLE.....                         | 95  |
|    | 7.1     | Finite Element Model.....                               | 98  |
|    | 7.2     | Predicted Response.....                                 | 98  |
|    | 7.2.1   | Cooldown Thermal Residual Stresses.....                 | 98  |
|    | 7.2.2   | Moisture-Induced Stresses.....                          | 102 |
|    | 7.2.3   | Axial Compressive Loading.....                          | 108 |
|    | 7.2.3.1 | Room Temperature, Dry Condition.....                    | 108 |
|    | 7.2.3.2 | Room Temperature, Wet Condition.....                    | 111 |
| 8  |         | DISCUSSION OF ANALYTICAL/EXPERIMENTAL CORRELATIONS..... | 118 |
|    | 8.1     | Microporosity.....                                      | 118 |
|    | 8.1.1   | Longitudinal Tensile Loading.....                       | 118 |
|    | 8.1.2   | Transverse Tensile Loading.....                         | 119 |
|    | 8.1.3   | Longitudinal Shear Loading.....                         | 120 |
|    | 8.1.4   | Summary of Microporosity Results.....                   | 122 |
|    | 8.2     | Laminate with Ply Drop-Offs.....                        | 122 |
|    | 8.3     | Laminate with Hole.....                                 | 124 |
| 9  |         | CONCLUSIONS.....  | 126 |
| 10 |         | REFERENCES.....   | 128 |

## SECTION 1

### INTRODUCTION

The present study is a continuation of prior investigations of the response of a composite laminate to compressive static and fatigue loadings [1-3]. The composite material used throughout these consecutive studies has been Hercules AS/3501-6 graphite/epoxy. Attention has been focused on a 30-ply laminate, viz,  $[0_{16}/(\pm 45)_5/90_4]$ , representative of the skin panel configuration near the root of the vertical stabilizer of the F-18A fighter aircraft.

In the first-year study [1], in addition to the evaluation of the F-18 laminate, unidirectional composites were also analyzed and tested in axial and transverse static tension and compression, and  $[\pm 45]$  laminates were analyzed and tested in axial static tension. Compression fatigue was also performed using these same material configurations. Testing, including axial compression static and fatigue testing of the F-18 laminate, was performed at room temperature, dry (RTD), room temperature wet (RTW), elevated temperature, dry (ETD), and elevated temperature, wet (ETW) test conditions. The elevated temperature was 218°F, and the wet condition corresponded to one weight percent moisture absorption of the composite. This temperature is representative of that encountered in supersonic flight, and the moisture content is representative of the quasiequilibrium moisture absorption achieved in a tropical environment. In the first-year study, only defect-free composites were considered.

In the second-year study [2], only the F-18 laminate was used. Two different ply drop-off configurations were tested, viz, either two 0° plies were abruptly ended within the specimen gage length, or two sets of  $(\pm 45)$  plies were dropped off. This resulted in a transition from a 30-ply laminate to either a 28-ply laminate or a 26-ply laminate. Axial static and fatigue compression loadings were applied to these two ply drop-off specimen configurations, as well as to plain laminates (i.e.,

continuous 30-ply laminates containing no ply drop-offs). Testing at -65°F in the wet condition (-65°F<sub>W</sub>) was also performed along with the four other test conditions previously defined.

The third-year study [3] focused on the influence of deliberately induced uniform porosity in the graphite/epoxy composite. Unidirectional, [ $\pm 45$ ], and F-18 laminates were fabricated containing 1.5 to 2.0 percent voids. These were tested under axial static and fatigue compression loadings, at room temperature, dry and wet, and elevated temperature, wet conditions. Static tensile testing at the RTD condition was also included.

A limited number of F-18 laminates containing a delamination at the midplane were also tested at the RTD condition, in both static compression and compression fatigue. This delamination, 0.5" long and extending across the full width of the test specimen, was induced by imbedding a piece of Teflon film at the midplane.

The results of these three prior studies, fully reported in References [1-3], formed the basis of the study being reported here. A 16-ply unidirectional laminate was fabricated of the same Hercules AS/3501-6 graphite/epoxy material used in the prior studies, and tested in axial tension and short beam shear at room temperature and 250°F, as a quality control check. This laminate, fabricated using standard procedures, contained less than 0.7 percent voids. Two F-18 laminates were also fabricated, each containing two 0° ply drop-offs, as in the second study [2]. One laminate contained a negligible number of voids (the average measured void content was 0.033 percent). The other F-18 laminate contained an average 2.5 percent voids based upon chemical analysis, and 4.5 percent based upon optical image analysis. The difference is related to the inherent inaccuracies of each measurement technique, and variations in the densities of the fiber and matrix constituents (which influenced the chemical analysis results). Nevertheless, there is reasonable confidence that the actual porosity was in the 2.5 to 4.5 percent range, comparable to that obtained in Reference [3] also.

These nonporous and porous F-18 laminates with 0° ply drop-offs were static compression and compression fatigue tested under room temperature, wet (1.3 weight percent moisture) conditions. In addition



to the ply drop-offs, some test specimens also contained either an open or partially loaded hole centered at the ply drop-offs, to evaluate the interaction effect. These data are presented in detail in Reference [4].

All of the experimental data generated by Northrop Corporation during the four studies for the Naval Air Systems Command, and all of the failed test specimens, were sent to the University of Wyoming for analysis purposes. During the prior three studies, a considerable amount of scanning electron microscopic examination of fracture surfaces was performed at Wyoming on the failed specimens. Also, various analysis methods and related computer programs were used to model the composite materials and loading conditions, in an attempt to better understand the composite performance under load. This involved the continual development and use of state-of-the-art analysis tools.

The fourth-year study reported here followed these same directions. A newly revised and updated two-dimensional (2-D) finite element micromechanics analysis was used to model local microporosity around individual fibers. The 3-D nonlinear, orthotropic finite element analysis introduced and used briefly in the prior-year study [3] was used more extensively, to model the ply drop-off and hole in the F-18 laminate.

## SECTION 2

### SUMMARY

The present study was focused on the analysis of microporosity present around individual fibers in a laminate ply, ply drop-offs, and round through-the-laminate-thickness fastener holes.

During this time, the Composite Materials Research Group's 2-D finite element micromechanics analysis and associated computer program was completely revised and updated. This included the combining of the previously developed longitudinal shear loading capability [5], which had been used extensively in the second-year work [2], with a crack propagation analysis [6], which had not been used in any of the prior NASC studies. Incorporation of a frontal solution technique greatly increased the size of physical models which can now be analyzed. The PATRAN pre- and post- processing graphics package also is now available for use in input grid generation, and presentation of results.

The 3-D finite element analysis conceptually introduced in the second-year report [2], and used in a very preliminary manner in the prior study [3], was further developed during the past year. This analysis and associated computer program represents state-of-the-art analysis technology, and as such is taxing the capabilities of current computer systems. Thus, it is still not possible to model composite laminates in the full detail desired. Nevertheless, major advances were made during the past year, and some of the results obtained are presented here.

Specifically, it was found that the predicted influence of microporosity in reducing the transverse tensile strength of a unidirectional ply did correlate with the available experimental data. Also, the micromechanics analysis indicated no loss of longitudinal shear strength, which agreed with the experimental observations as well. Longitudinal tensile strength reductions due to porosity which were experimentally measured were not adequately predicted, suggesting that a

full 3-D analysis is required. This will be the topic of a future investigation.

In the experimental work of both References [2] and [4] it had been established that ply drop-offs reduced the axial compressive strength of the F-18 laminate relatively little. The present 3-D finite element analysis of the  $0^\circ$  ply drop-off geometry correlated well with these experimental observations. Further, the analysis provided detailed internal stress states, ply by ply, which indicated why the laminate responded as it did under various combinations of curing residual stresses, moisture-induced stresses, and mechanical loadings. This capability provides valuable insight into why composite laminates behave as they do, and even more importantly, what can be done in the future to improve their performance.

The strength degradation of the F-18 laminate due to the presence of a fastener hole, observed experimentally, was also correlated well by the 3-D finite element analysis of this geometry. The stress concentrations in the dominating  $0^\circ$  plies due to the hole, particularly the high transverse tensile stresses induced by the axial compressive loading, were predicted to initiate composite fracture.

Although much more analytical work remains to be done, including the further development of the analysis methods themselves, the current study has demonstrated that significant insights can be gained by performing such analyses. Not only can they aid in understanding experimentally observed behavior, they can also be used very effectively to suggest modifications of composite properties which would improve performance. It is this predictive capability which will be most valuable in future studies.

### SECTION 3

#### SYNOPSIS OF PRIOR WORK

The present analytical study was a direct outgrowth of the three prior investigations, detailed results of which were presented in References [1-3]. Since the analysis of compressive loading (static or fatigue) of the same Hercules AS/3501-6 graphite/epoxy was the central thrust of all three prior studies, as well as of the current investigation, it is useful to summarize this prior analytical work. This analytical work paralleled the experimental work performed by Northrop personnel, as also presented in detail in References [1-3]. A brief summary of the types of experiments performed was included in the Introduction of the present report.

During the first year [1], a detailed literature survey was conducted, focused on compressive failure modes in graphite/epoxy composites, and fatigue loadings. A very extensive scanning electron microscopy (SEM) study of the failure modes exhibited by the various unidirectional, [ $\pm 45$ ], and F-18 laminates (all defect-free, i.e., no ply drop-offs, porosity, delaminations, or fastener holes) fabricated and tested by Northrop was also performed. A total of 59 SEM specimens were mounted and examined, representing all of the layup configurations, environmental conditions, and loadings. Of the large number of SEM photographs taken, 20 were included and discussed in Reference [1] to document the failure modes observed. Fiber-matrix debonding, ply interface debonding, and fiber microbuckling were all commonly noted, along with matrix lacerations indicative of matrix shear failures.

General trends were noted. Fiber microbuckling was common in the static axial compression failures of the unidirectional composites. The axial compression fatigue failures exhibited less fiber microbuckling, and more axial splitting and macrobuckling. The compression static and fatigue failures of the [ $\pm 45$ ] laminates were mutually similar, being dominated by interlaminar failures, and limited fiber microbuckling.

The F-18 laminates, containing  $0^\circ$ ,  $\pm 45^\circ$ , and  $90^\circ$  plies, exhibited most of the several failure modes simultaneously, although delaminations between plies were observed more frequently, and axial splits within plies were nonexistent. No influence of moisture preconditioning or test temperature on failure mode was observed.

During the second-year study [2], 71 additional SEM specimens were mounted and examined. Thirteen SEM photographs of failure surfaces were included and described in Reference [2]. These specimens contained ply drop-offs, as described in Section 1, which undoubtedly were the fracture initiation sites. Unfortunately, these ply drop-offs could not be readily identified in the SEM, because of the extensive shattering which had occurred at failure. In fact, the presence of ply drop-offs had little influence on the failure modes observed, indicating the very forgiving nature of composite materials. As in the first-year study, no significant influence of elevated temperature or moisture was observed. However, in the second-year study, a  $-65^\circ\text{F}$ , wet test condition was added. At  $-65^\circ\text{F}$ , the graphite/epoxy composites did tend to fail in a more brittle manner, and exhibit higher strengths, than at room or elevated temperatures.

As a result of these first- and second-year SEM studies, the compressive failure modes which occur in graphite/epoxy composites were well-established.

These SEM observations indicated that the local state of stress in the matrix material surrounding individual fibers, and in particular the normal and shear stresses at the fiber-matrix interface, have a dominant influence on the response of even a complex laminate such as the F-18 layup. Thus, extensive use was made of the University of Wyoming's micromechanics analysis and associated computer program [7,8] during the first- and second-year studies, to determine these stress states as a function of the hygrothermal environment.

### 3.1 Micromechanics Analyses

The micromechanics analysis available at the beginning of the first-year study was a two-dimensional (2-D), generalized plane strain (i.e., the normal strain in the fiber axis direction,  $\epsilon_z$ , is constant across the cross section, but need not be zero), elastoplastic (Prandtl-Reuss flow rule and octahedral shear stress yield and failure

criteria) analysis, capable of modeling temperature- and moisture-dependent matrix material properties, and anisotropic fibers [7,8]. During the second year, a longitudinal shear loading capability was added [5]. The finite element solution technique, incorporating constant strain triangular elements and a Gaussian elimination procedure, was retained.

The Hercules AS graphite fiber properties needed as input data for this analysis were taken from the literature. The properties of the Hercules 3501-6 epoxy matrix were measured at Wyoming. All of these constituent material property data are summarized in Reference [5].

During the first year, attention was focused on the axial and transverse compression loadings of the unidirectional composite, as being the simplest system to analyze. The four test conditions defined in Section 1, viz, room temperature, dry (RTD), room temperature, wet (RTW), elevated temperature, dry (ETD), and elevated temperature, wet (ETW), were analyzed for both axial and transverse compression loadings. In addition, the axial and transverse tensile loading data at the RTD condition were also analyzed.

The correlations between theory and experiment were good for stiffness properties, i.e., moduli and Poisson's ratios. Strengths were not predicted well, due to the lack of an adequate failure criterion. Of the greatest significance perhaps was the fact that complete stress distributions were predicted by the micromechanics analysis, which permitted detailed insights into why the composite failed as observed in the SEM examinations. For example, the predicted high interface tensile stresses induced by axial compressive loading suggested potential interface debonding, leading to microbuckling of the unsupported fibers.

### 3.2 Laminate Analyses

The [ $\pm 45$ ] and F-18 laminates were modeled during the first-year study using a conventional point stress analysis [1]. This analysis approach models each ply as a linearly elastic, orthotropic, but homogeneous material. That is, individual fibers in the matrix are not recognized, and only ply stacking geometry (but not boundary effects, local defects, or similar discontinuities) is modeled. Nevertheless, such an analysis is very useful in estimating average ply stresses, and it does predict composite stiffness properties very well.

During the second-year study [2], a combined micromechanics/point stress analysis of laminate response was developed. This was possible because a longitudinal shear loading capability had been added to the micromechanics analysis [5]. Although the point stress laminate analysis was linearly elastic, the micromechanics analysis was able to model material nonlinearities. Thus, the average ply stresses predicted by the point stress analysis were used as input loadings for the micromechanics analysis. The micromechanics analysis then accounted for local nonlinear response of the matrix, providing modified ply stiffness properties as input for the next loading increment of the point stress analysis.

Both [ $\pm 45$ ] laminates and F-18 laminates were analyzed in this manner, for the various environmental conditions, with good predictions of the experimentally observed nonlinear stress-strain responses being obtained [2]. No attempt was made to predict strengths, because of the lack of an adequate failure criterion.

It was proposed that in future studies, as 3-D finite element laminate analyses became available, that they be used to replace the point stress laminate analysis. These 3-D analyses would be nonlinear, and capable of modeling interlaminar stresses as well as in-plane stresses. Combined with the (nonlinear) micromechanics analysis, a very accurate physical modeling of the laminate response would be possible.

During the second-year study, such a 3-D finite element analysis [9] was briefly introduced as a potential tool for analyzing stress states around ply drop-offs. It was not until the third-year study that the first attempt was made to actually perform such an analysis, as described in the following paragraphs.

### 3.3 Ply Drop-Off Analyses

Ply drop-offs were studied experimentally during the second-year study [2], as discussed in Section 1 of the present report. Preliminary photomicrographs of polished cross sections of actual laminates were prepared, to define the ply drop-off geometries present. It was observed that the  $0^\circ$  plies ended abruptly, with a small but distinct pocket of matrix material forming at the end of the dropped-off ply. The adjacent  $90^\circ$  ply on one side was able to deform sufficiently to fill the gap left by the  $0^\circ$  ply end, accounting for only a small matrix

pocket being formed. The  $+45^\circ$  and  $-45^\circ$  plies were dropped off in a staggered manner, with approximately one-half inch between ends of these adjacent plies. Since each ply is on the order of only 0.005 inches thick, the ply ends were on the order of 100 ply thicknesses apart, i.e., a large distance on the microlevel. For both dropped-off  $45^\circ$  plies, the other adjacent ply was a  $0^\circ$  ply. Since  $0^\circ$  plies have little ability to deform laterally to fill the space created by the adjacent  $45^\circ$  ply drop-off, and the other adjacent ply is a  $45^\circ$  ply, also much less deformable than the  $90^\circ$  ply of the  $0^\circ$  ply drop-off configuration, an elongated matrix pocket was formed at the end of each dropped-off  $45^\circ$  ply.

In addition to the two photomicrographs of ply drop-offs included in Reference [2], seven additional photomicrographs, of much better quality, were included in Reference [3]. All of this information was used to construct finite element models of the ply drop-off regions. Because of computer size limitations, it was not possible to construct grids having the degree of refinement desired. Thus, for demonstration purposes, as fine a grid as possible was used to model each geometry. These grids, for no drop-off,  $0^\circ$  ply drop-off, and  $45^\circ$  ply drop-off cases, were included in Reference [3]. Eight-node isoparametric elements were used in all cases. The orthotropic ply properties were modeled, of course, but nonlinear response was not.

The actual numerical results obtained and presented in the third-year report [3] were of limited practical use, but did demonstrate the potential of 3-D finite element analyses for such applications. As computer facilities continue to improve, these large-scale 3-D finite element analyses will become primary analysis tools within the composite materials community. This could possibly occur within the next five years.



## SECTION 4

### CONSTITUENT AND LAMINA MATERIAL PROPERTIES

A major thrust of this research effort was to model conventional aircraft composite material constructions under uniaxial compressive loadings. Parameters in these analyses included nonlinear stress-strain behavior as well as hygrothermally (temperature and moisture) dependent material properties. As the models examined were three-dimensional, material properties for all three principal material coordinate directions were required. A data bank containing the nonlinear material properties for AS1/3501-6 graphite/epoxy as functions of temperature and moisture content does not, to the authors' knowledge, exist in the current published literature. It was therefore necessary to predict the required AS1/3501-6 lamina properties using previously developed numerical micromechanics techniques.

#### 4.1 Micromechanics Analysis

The Composite Materials Research Group (CMRG) at the University of Wyoming has developed a numerical (finite element) micromechanics model to predict the loading response of a unidirectional fiber reinforced composite lamina [5]. This analysis allows for nonlinear stress-strain behavior in the constituent components of a composite system as well as for temperature- and moisture-dependent material properties. The analysis technique has been described in detail in Reference [5]; therefore, only a brief description will be included here.

The model is based on a generalized plane strain finite element analysis of a typical repeating unit of matrix material containing a single fiber within a unidirectional continuous fiber composite. The region to be analyzed is shown in Figure 1. If a rectangular fiber packing arrangement is assumed, the region of interest reduces to the quadrant depicted in Figure 2 via symmetry arguments. Other geometric arrays may be assumed, but previous work has shown that assuming a square array provides good correlation with experiment [10,11].

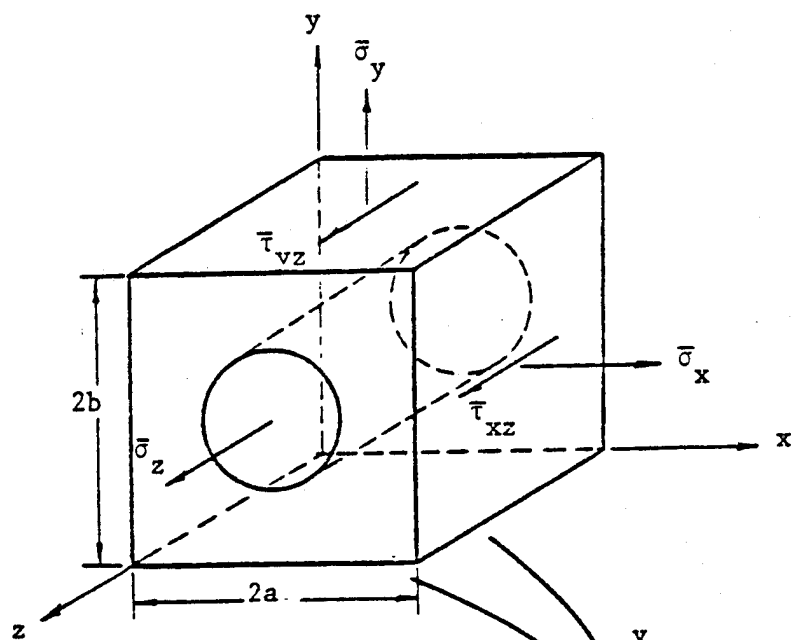


Figure 1 Unit cell of the fiber arrangement

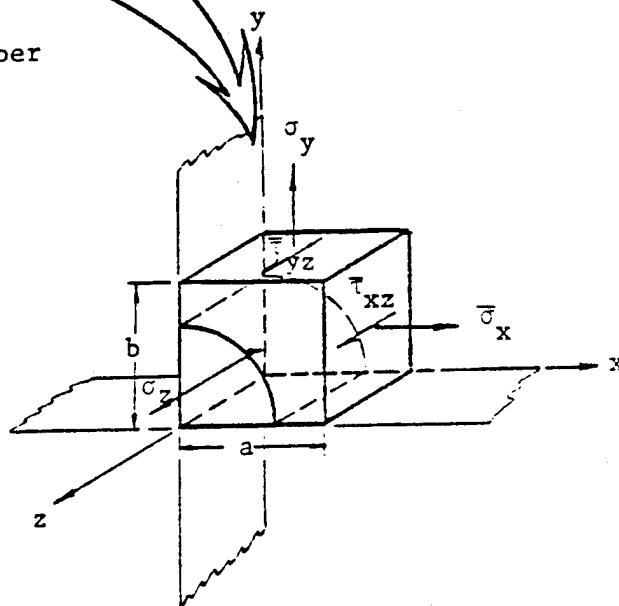


Figure 2 Quadrant to be analyzed

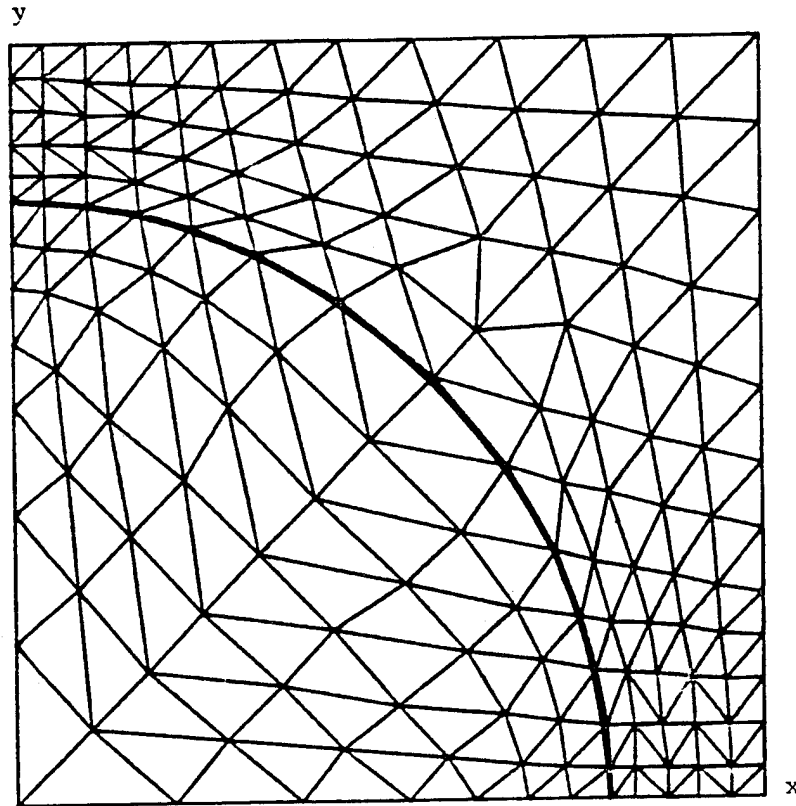
Further discussion of the rationale in choosing this model is contained in References [5,8]. The finite element grid used in the present micromechanics analysis is shown in Figure 3. By changing the radius of the fiber relative to the unit cell boundary, different fiber volumes within the composite material can be simulated. A typical grid is pictured in Figure 3.

Generalized plane strain, for purposes of this analysis, assumes displacements may occur in all three coordinate directions. Specifically, each displacement is dependent upon the  $x$  and  $y$  coordinates, and the displacement in the  $z$ -direction (fiber direction) has an additional linear dependence in the  $z$ -direction, the axial (fiber) coordinate of the composite ply. Including  $x$  and  $y$  dependence of the  $z$ -displacements allows a special form of axial (longitudinal) shear deformation corresponding to the generalized plane strain treatment. Therefore, although the analysis is basically two-dimensional in nature, five components of applied stress can be modeled, specifically  $\bar{\sigma}_x$ ,  $\bar{\sigma}_y$ ,  $\bar{\sigma}_z$ ,  $\bar{\tau}_{xz}$  and  $\bar{\tau}_{yz}$ . The model is therefore capable of predicting stress-strain response due to any one or any combination of these loading modes.

Material behavior of the fiber constituent is assumed to be transversely isotropic, in order to model anisotropic fibers such as graphite. The matrix material is assumed to be isotropic and elastoplastic, the plastic response being modeled by the Prandtl-Reuss flow rule. As previously noted, temperature and moisture effects on the constituent material properties are also included.

#### 4.2 Constituent Properties

Constituent material properties for the Hercules AS fiber were obtained from Reference [12] where possible. Transverse fiber properties are very difficult to measure directly; therefore it was necessary to estimate these values based on previous experience with other graphite fibers [13]. The fiber properties used in the present analysis are listed in Table 1.



FINITE ELEMENT MESH

Figure 3. Finite Element Model of One Quadrant of the Typical Repeating Unit Cell of a Unidirectional Composite Material in a Square Fiber Packing Array.

TABLE 1. MATERIAL PROPERTIES FOR HERCULES AS GRAPHITE FIBER [12].

|                                |   |
|--------------------------------|---|
| Longitudinal Modulus           | $E_{\ell} = 34 \text{ Msi}$                             |
| Transverse Modulus             | $E_t = 2.0 \text{ Msi}$                                 |
| Major Poisson's Ratio          | $\nu_{\ell t} = 0.20^*$                                 |
| In-Plane Poisson's Ratio       | $\nu_{tt} = 0.25^*$                                     |
| Longitudinal Shear Modulus     | $G_{\ell t} = 4 \text{ Msi}^*$                          |
| Longitudinal Thermal Expansion | $\alpha_{\ell} = -0.36 \times 10^{-6}/^{\circ}\text{C}$ |
| Transverse Thermal Expansion   | $\alpha_t = 18 \times 10^{-6}/^{\circ}\text{C}$         |

---

\*estimated

The graphite fibers were assumed to be linearly elastic and not affected by temperature or moisture changes. For the limited temperature range of this study (21° to 177°C) this is a reasonable assumption.

Hercules 3501-6 epoxy resin material properties were used to model the matrix material. These data were measured at Wyoming as part of a research program conducted for the Army Research Office [14]. Tension and torsion tests were conducted to measure the tensile and shear properties of the neat (unreinforced) 3501-6 epoxy resin at three test temperatures and two absorbed moisture conditions. In addition, the thermal expansion and moisture expansion coefficients were measured [15]. These properties, particularly the shear properties have been used during the previous years of the present research effort [1-4].

As the shear stress-strain response of the 3501-6 epoxy is nonlinear, it is necessary to input the entire stress-strain curve into the micromechanics analysis. This is done by using a three-parameter experimental equation of the form first suggested by Richard and Blacklock [16], i.e.,

$$\tau = \frac{G\gamma}{[1 + |\frac{G\gamma}{\tau_0}|^n]^{\frac{1}{n}}} \quad (1)$$

where

$G$  = initial shear modulus

$n$  = curvature parameter

$\tau_0$  = asymptotic shear stress value

$\gamma$  = shear strain

Three parameters,  $G$ ,  $n$ , and  $\tau_0$  describe the stress-strain response of the epoxy in a particular temperature and moisture environment. By then using regression techniques, each parameter may be described as a polynomial function in temperature and moisture by using equations of the form

$$P = C_1T + C_2M + C_3TM + C_4 \quad (2)$$

where  $P$  = property of interest (e.g.,  $G$ ,  $n$ ,  $\tau_0$ , etc)

$C_1 - C_4$  = regression coefficients for that property.

Therefore, the entire shear stress-strain response of the 3501-6 epoxy is prescribed by three equations for  $G$ ,  $n$  and  $\tau_0$ . The coefficients describing the shear stress-strain behavior of the 3501-6 epoxy resin as well as the thermal and moisture expansion coefficients are shown in Table 2. Families of curves representing the shear stress-strain response based on these equations for six different environmental conditions are plotted in Figure 4.

TABLE 2. HERCULES 3501-6 NEAT EPOXY RESIN MATERIAL PROPERTIES EXPRESSED AS FUNCTIONS OF TEMPERATURE AND MOISTURE (T in °C, M in Wt.%).

$$\text{Property} = C_1 T + C_2 M + C_3 TM + C_4$$

| Property            | $C_1$                 | $C_2$                 | $C_3$                   | $C_4$                 |
|---------------------|-----------------------|-----------------------|-------------------------|-----------------------|
| G (psi)*            | $-1.14 \times 10^3$   | $-2.49 \times 10^3$   | $-3.38 \times 10^1$     | $2.60 \times 10^5$    |
| $n^*$               | $2.56 \times 10^{-3}$ | $2.78 \times 10^{-3}$ | $1.65 \times 10^{-4}$   | $1.54 \times 10^0$    |
| $\tau_o$ (psi)*     | $-1.50 \times 10^2$   | $-1.36 \times 10^3$   | $6.46 \times 10^0$      | $2.67 \times 10^4$    |
| $\tau_{ult}$ (psi)* | $-8.73 \times 10^1$   | $-6.03 \times 10^2$   | $1.86 \times 10^0$      | $1.66 \times 10^4$    |
| $\alpha$ (in/in/°C) | $1.22 \times 10^{-7}$ | $1.04 \times 10^{-6}$ | $-5.90 \times 10^{-10}$ | $3.83 \times 10^{-5}$ |
| $\beta$ (in/in/%M)  | 0                     | 0                     | 0                       | $3.20 \times 10^{-3}$ |
| $\nu$               | 0                     | 0                     | 0                       | $0.34 \times 10^0$    |

\*Based on solid rod torsion shear data

#### 4.3 Lamina Material Properties

Material properties for an individual AS/3501-6 lamina were calculated using the finite element micromechanics model described earlier. Property computation consisted of applying a series of incremental loadings to the micromechanics model to simulate longitudinal tension, transverse tension, longitudinal shear, and transverse shear. These loadings are illustrated in Figure 5. Transverse shear loading, Figure 5d, was simulated by applying tension and compression stresses in the 2 and 3 directions of the material to induce a pure shear stress on a plane at 45° from either axis. Strictly speaking, this would be a  $\bar{\tau}_{23}$  shear stress loading on a unit cell with a different packing geometry than the loadings depicted in Figures 5a through c. However, it was assumed that the resulting error in using this different packing geometry could be neglected for the present work. As discussed previously, the differences in assuming different fiber packing geometries are small [10,11].

All loading cases were initiated at a reference temperature of 177°C, the curing temperature for the laminate. The model was then incrementally cooled to room temperature; therefore, the effects of thermally-induced curing stresses are included in the model. At this point, the model was reheated or moisture was absorbed to attain the

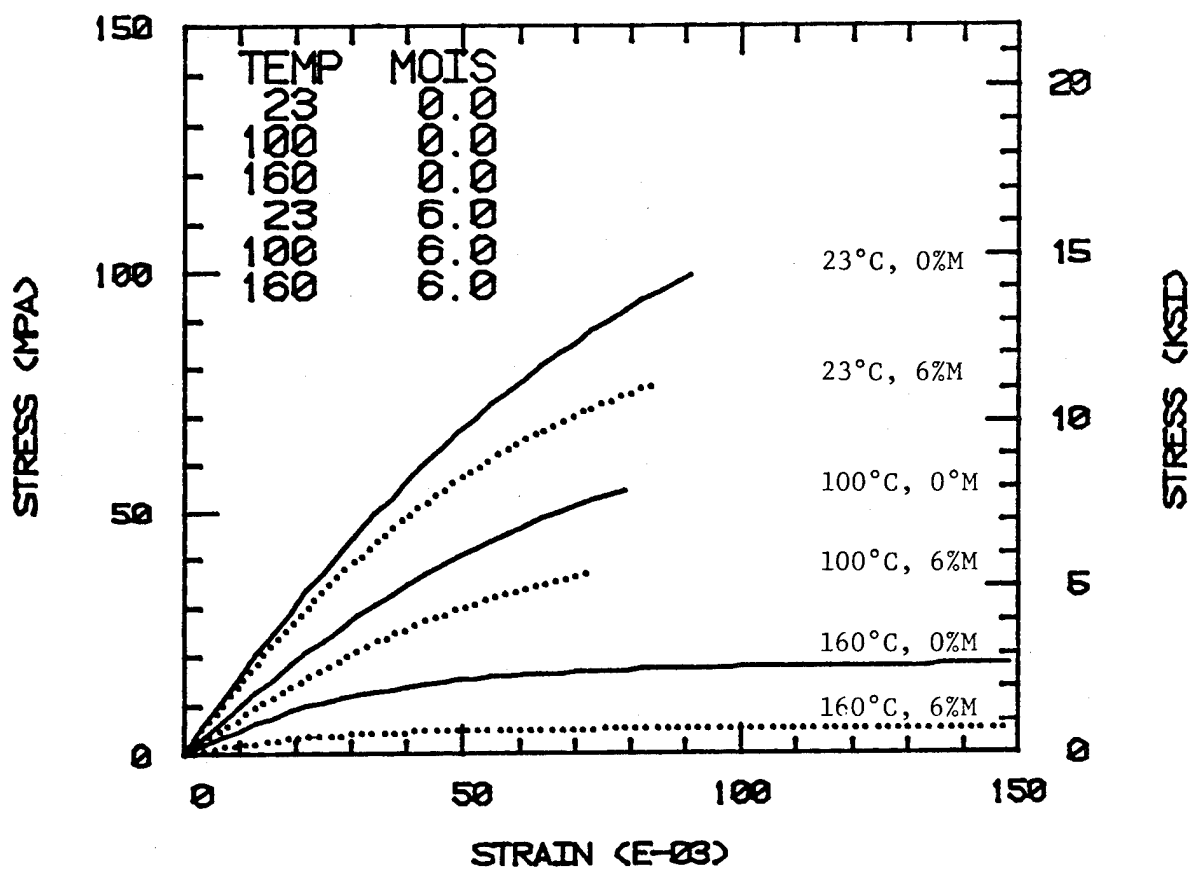


Figure 4. Calculated Shear Stress-Strain Response for Hercules 3501-6 Epoxy Resin at Six Different Hygrothermal Conditions. (Temperature, °C; Moisture, Weight Percent)



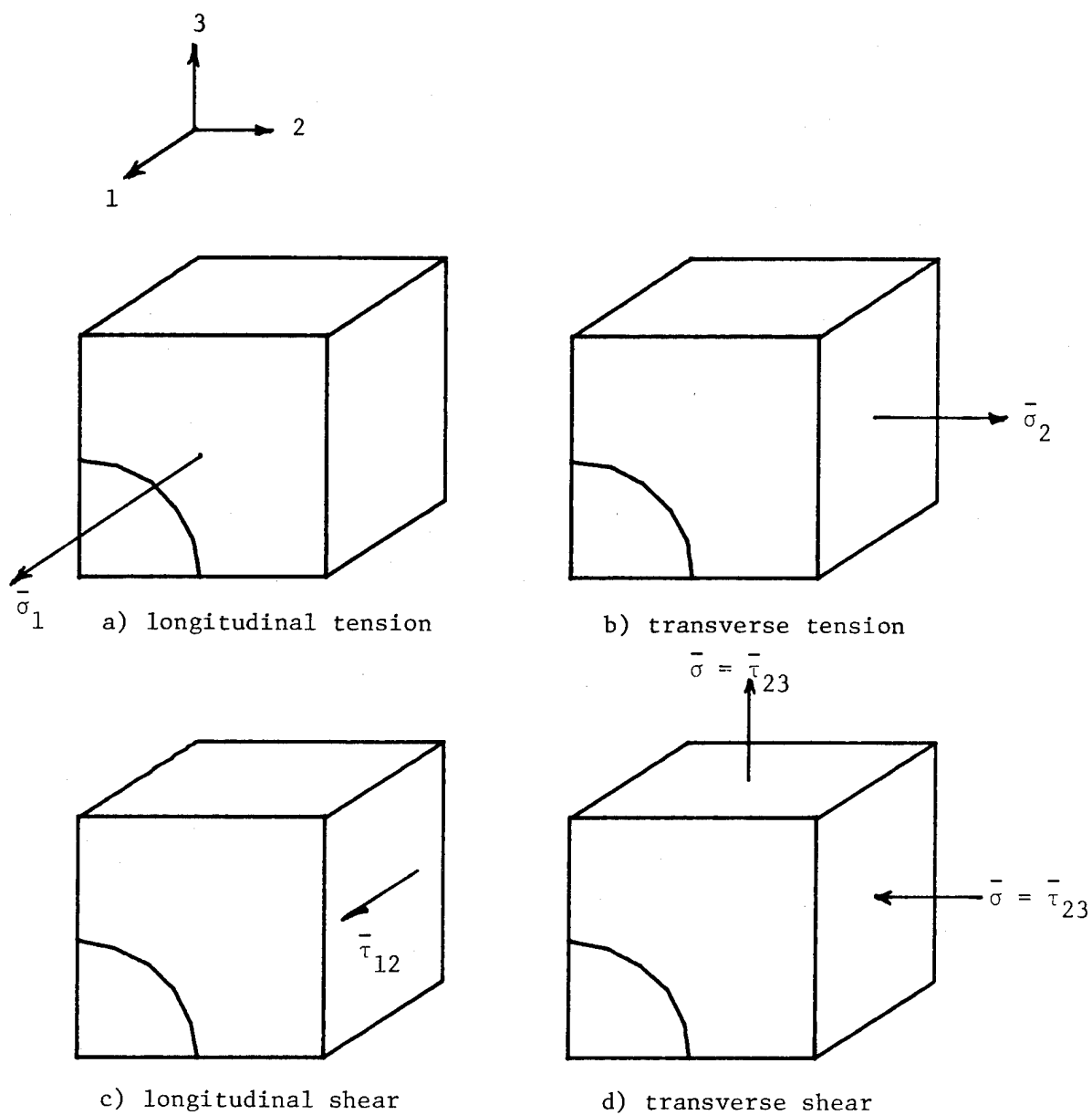


Figure 5. Micromechanics Applied Loads for Unidirectional Composite Lamina Stress-Strain Characterization.

desired environmental conditioning at which the mechanical loadings were to be applied. These conditions duplicate the procedures which would be used in a laboratory when fabricating, environmentally conditioning, and then testing specimens. Computer runs were made to calculate the four mechanical properties in four environments, a total of 16 runs. An additional two computer runs were used to calculate the composite thermal and moisture expansion coefficients.

Stress-strain behaviors for each of the four mechanical loading cases were calculated for room temperature, 80°C and 160°C, dry, and room temperature, 1%M moisture environments. In all cases, the fiber volume was assumed to be 60 percent. At the time this analysis was performed, crack propagation routines did not yet exist as part of this finite element micromechanics model. (These routines were added later, and used to perform the porosity studies described in Section 5.) Therefore, no attempt was made to predict the lamina strength properties with these early micromechanics calculations; only stress-strain behavior prior to failure was of interest.

Predicted stress-strain response for an AS/3501-6 composite lamina for each of the four loading cases and four environments are shown in Figures 6 through 9. Looking first at the longitudinal tension (fiber direction) loading case, it can be seen that the different environments did not affect the stress-strain response of the composite lamina at all. This is to be expected as the fiber properties were assumed to be constant at all temperature and moisture conditions and this loading case is fiber-dominated.

An environmental effect is noted in the stress-strain curves for transverse tension depicted in Figure 7. Increasing temperature or moisture content resulted in decreasing transverse modulus. Pronounced nonlinear behavior is evident for the 160°C temperature case. Again it will be noted that no attempt was made to predict strengths. Therefore, the apparent constancy of strength in Figure 7 is artificial. A more sophisticated analysis can now be performed to predict strength using the crack propagation analysis, but was not used here.

Longitudinal shear (in-plane) stress-strain curves are plotted in Figure 8. Pronounced nonlinearity exists for all environmental conditions. This is consistent with observed experimental behavior for

AS /3501-6 LONGITUDINAL TENSION  
21, 80, 100, 21 DEG. C 0, 1 % MOIS.  
FIBER VOLUME 60%

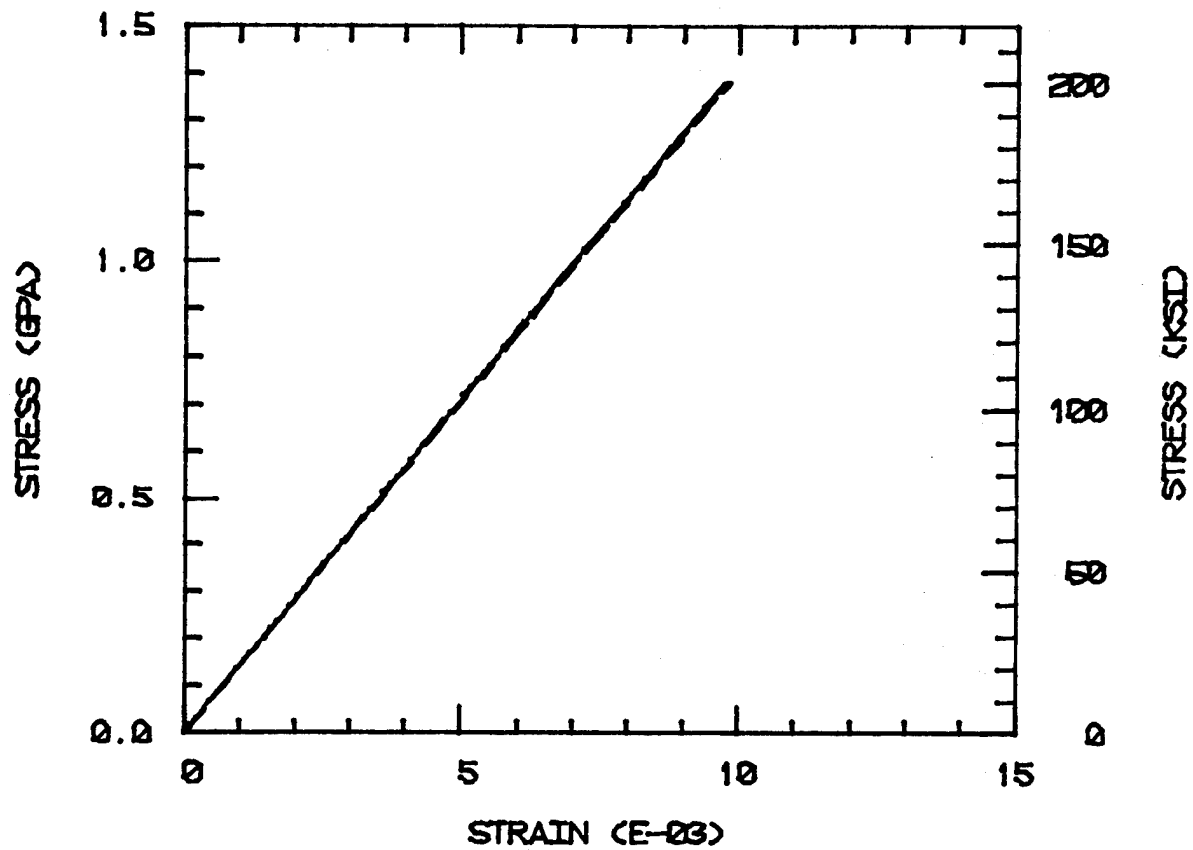


Figure 6. Micromechanics Predictions of Longitudinal Tensile Stress-Strain Behavior for AS/3501-6 Unidirectional Graphite/Epoxy Composite.

AS /3501-6 TRANSVERSE TENSION  
 21, 80, 160, 21 DEG. C 0, 1% MOIS.  
 FIBER VOLUME 60%

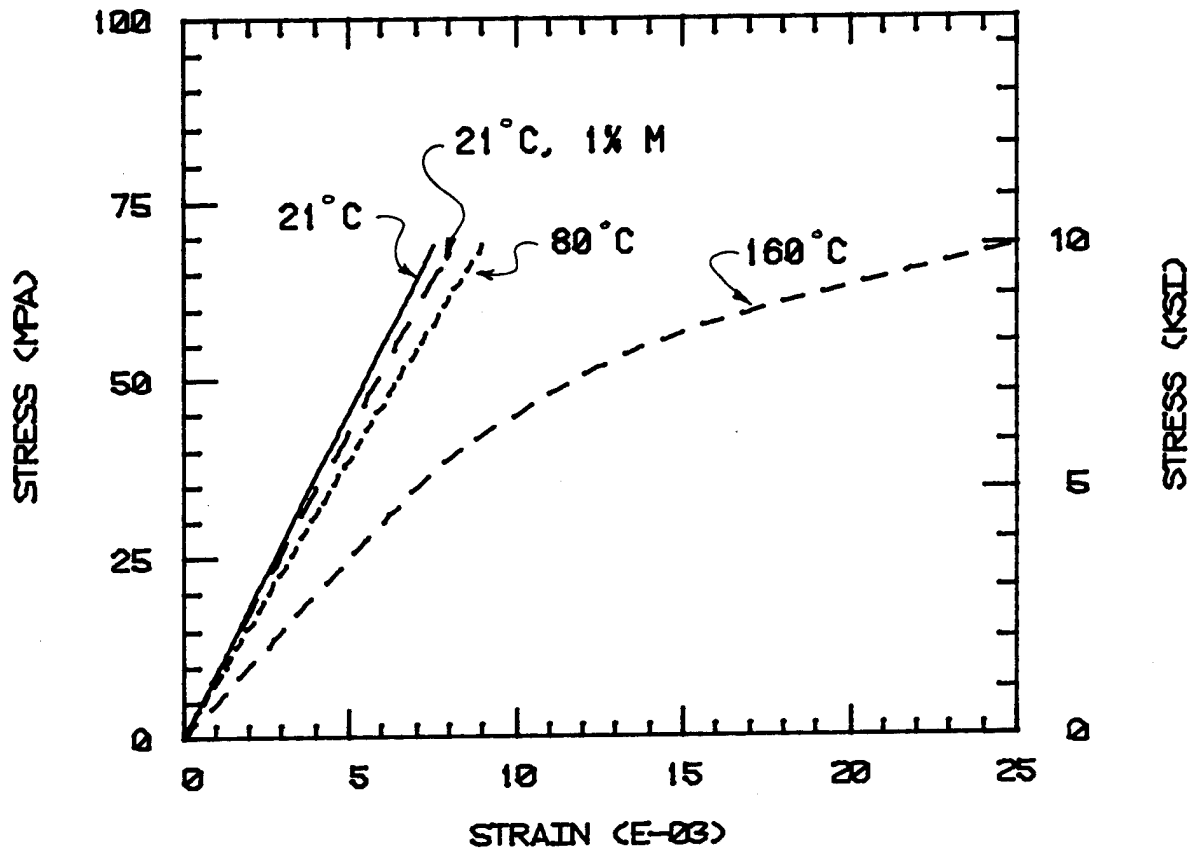


Figure 7. Micromechanics Predictions of Transverse Tensile Stress-Strain Behavior for AS/3501-6 Unidirectional Graphite/Epoxy Composite.

AS /3501-6 LONG. SHEAR  
 21, 80, 160, 21 DEG. C 0, 1 % MOIS.  
 FIBER VOLUME 60%

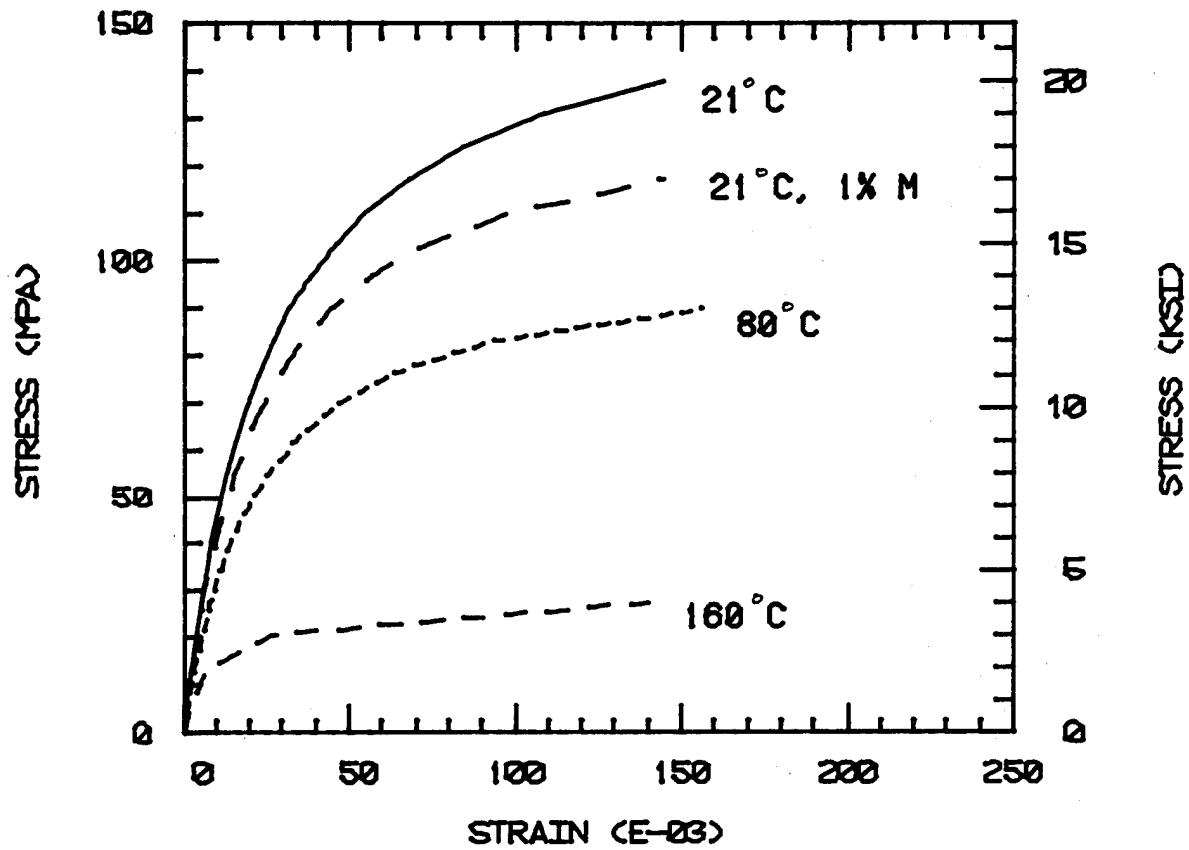


Figure 8. Micromechanics Predictions of Longitudinal Shear Stress-Strain Behavior for AS/3501-6 Unidirectional Graphite/Epoxy Composite.

AS /3501-6 TRAN. SHEAR  
 21, 80, 160, 21 DEG. C 0, 1 MOIS.  
 FIBER VOLUME 60%

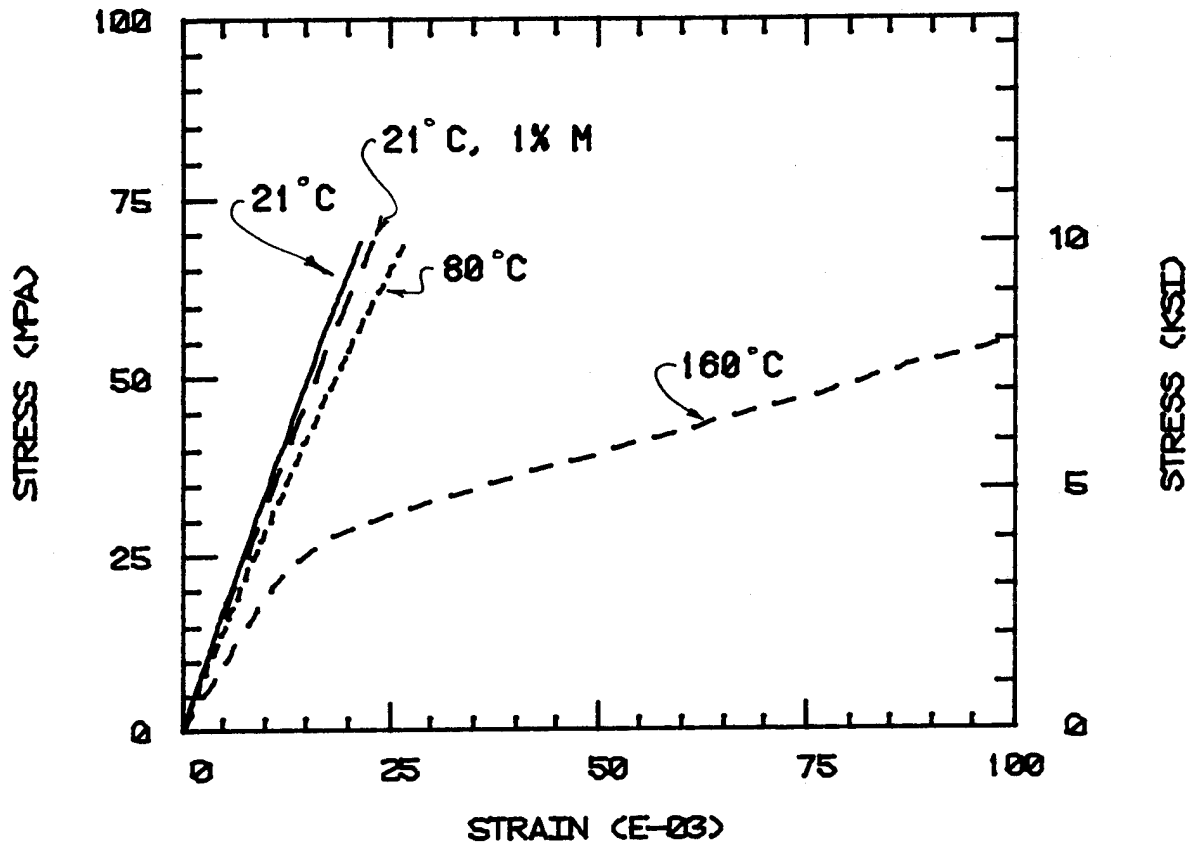


Figure 9. Micromechanics Predictions of Transverse Shear Stress-Strain Behavior for AS/3501-6 Unidirectional Graphite/Epoxy Composite.

this material as well [5]. The decreasing stiffness resulting from elevated temperature or absorbed moisture will be noted.

Transverse shear (interlaminar) stress-strain curves are plotted in Figure 9. Only slight nonlinearity is present for the room temperature, dry and 1% moisture cases, or even for the 80°C case, and the small stiffness reductions will be noted. However, as the temperature is increased the nonlinear behavior becomes quite pronounced for the 160°C case.

A summary of the calculated material properties at the various temperature and moisture environments is presented in Table 3. Transverse isotropy was assumed; therefore, all necessary 3-D properties may be calculated. Standard composite material coordinate notation is used, where the 1-direction is parallel to the fibers, the 2-direction is perpendicular to the fibers in the plane of the lamina, and the 3-direction is perpendicular to the plane of the lamina.

Predictions of thermal expansion and moisture expansion coefficients are also shown in Table 3. These properties were calculated by applying thermal and/or moisture loadings to the model and computing the resulting strains. Thermal expansion was calculated for a dry lamina. Moisture expansion was calculated for a lamina at room temperature.

Moisture expansion was assumed to occur as a linear function of moisture content. Therefore, the values of  $\beta_{11}$  and  $\beta_{22}$  are constant with increasing moisture content. However, the thermal expansion was not linear with increasing temperature, and was better represented as a quadratic in temperature. Thus, the thermal expansion coefficients  $\alpha_{11}$  and  $\alpha_{22}$  are linearly dependent on temperature. Plots of these two coefficients are shown in Figures 10 and 11. Note in Figure 10 that the longitudinal thermal expansion coefficient  $\alpha_{11}$  is predicted to be less than zero only at temperatures below 125°C, after which the coefficient becomes positive. Understanding this thermal behavior may be important when designing thermally stable structures such as telescope mirror mounts.

The transverse thermal expansion coefficient  $\alpha_{22}$  is only slightly temperature dependent over the modeled temperature range and is, of

TABLE 3. PREDICTED ELASTIC CONSTANTS FOR AN AS/3501-6 GRAPHITE/EPOXY COMPOSITE LAMINA.

| Loading Case                             | Property   | Environment      |           |            |           |
|--|--|------------------|-----------|------------|-----------|
|  |  | 21°C, dry        | 82°C, dry | 160°C, dry | 21°C, 1%M |
| Long. tension                            | $E_{11}$ (Msi)   | 20.6             | 20.5      | 20.4       | 20.5      |
|  | $\nu_{12} = \nu_{13}$  | 0.25             | 0.26      | 0.25       | 0.25      |
| Trans. tension                           | $E_{22} = E_{33}$ (Msi)  | 1.32             | 1.13      | 0.72       | 1.24      |
| Long. shear                              | $G_{12} = G_{13}$ (Msi)  | 0.75             | 0.53      | 0.28       | 0.73      |
|  | $G_{23}$ (Msi)   | 0.49             | 0.42      | 0.27       | 0.45      |
| <hr/>                                    |  |                  |           |            |           |
| Thermal Expansion<br>(°C) <sup>-1</sup>  | $\nu_{23} = \frac{E_{22}}{2G_{23}} - 1$                                    | 0.35             | 0.35      | 0.33       | 0.38      |
|  | $\alpha_{11} = 2.146 \times 10^{-9}T - 2.658 \times 10^{-7}$               | dry              |           |            |           |
|  | $\alpha_{22} = \alpha_{33} = 4.634 \times 10^{-8}T + 3.112 \times 10^{-5}$ |                  |           |            |           |
| Moisture Expansion<br>(%M) <sup>-1</sup> | $\beta_{11} = 1.432 \times 10^{-4}$  | room temperature |           |            |           |
|  | $\beta_{22} = \beta_{33} = 5.120 \times 10^{-3}$                           |                  |           |            |           |



AS /3501-6

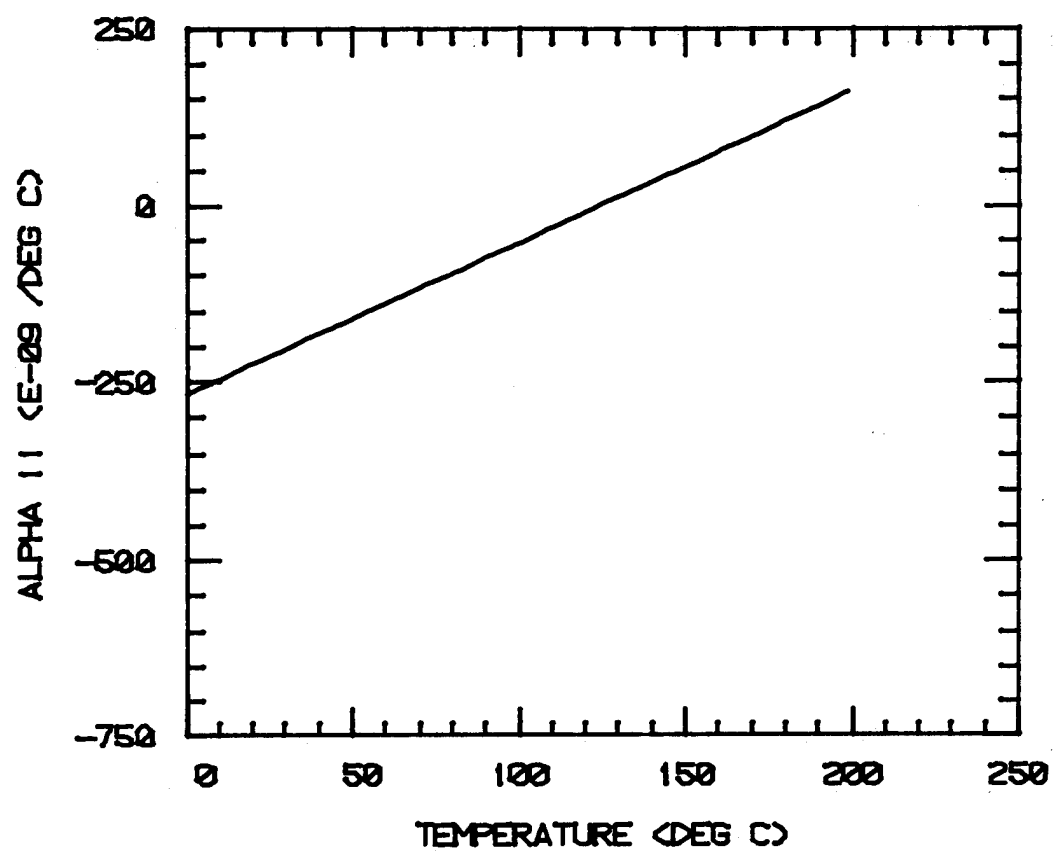


Figure 10. Micromechanics Prediction of Longitudinal Thermal Expansion Coefficient  $\alpha_{11}$  versus Temperature for AS/3501-6 Unidirectional Graphite/Epoxy Composite.

AS /3501-6

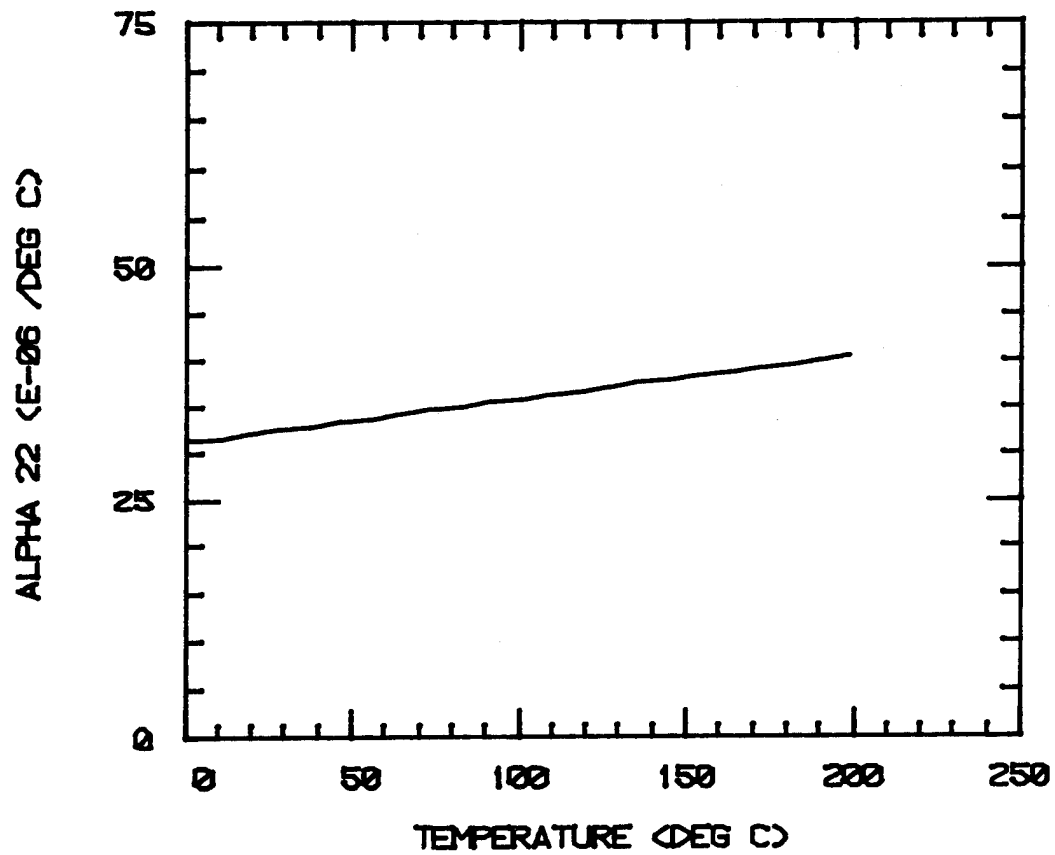


Figure 11. Micromechanics Prediction of Transverse Thermal Expansion Coefficient  $\alpha_{22}$  versus Temperature for AS/3501-6 Unidirectional Graphite/Epoxy Composite.

course, always positive as shown in Figure 11.

The numerical micromechanics analyses described here represent the bases for determining the 3-D properties used during the remainder of this research program.

#### 4.4 Effective Stress-Strain Behavior

The rigorous analysis of ply drop-offs and plates containing holes requires an approach which includes anisotropic (orthotropic or transversely isotropic) inelastic material behavior. While a number of 2-D and 3-D anisotropic elastic and isotropic inelastic finite element analyses exist, anisotropic, inelastic analyses have not been available. Such an analysis has been developed by the CMRG at the University of Wyoming.

The analysis method has been described in detail elsewhere [9] and has also been summarized in previous reports to NASC [2,3]. Therefore a detailed explanation will not be repeated here. The portion of the method which must be discussed is the use of an "effective stress-strain" constitutive relation to represent inelastic behavior in an anisotropic ply. A quadratic form in the six components of stress, similar to Hill's yield condition [18], can be chosen in the form

$$\begin{aligned} 2f(\sigma_{ij}) = & F(\sigma_2 - \sigma_3)^2 + G(\sigma_3 - \sigma_1)^2 + H(\sigma_1 - \sigma_2)^2 \\ & + 2L \tau_{23}^2 + 2M \tau_{13}^2 + 2N \tau_{12}^2 = 1 \end{aligned} \quad (3)$$

where F, G, H, L, M, and N are parameters characteristic of the current state of anisotropy. In the present study, these parameters of anisotropy are allowed to vary with changes in temperature and/or moisture content.

The form of Eq. (3) is valid only when the principal axes of anisotropy are taken to be the axes of reference; otherwise the stress components must be transformed. The functional dependence of the parameters of anisotropy on temperature and moisture follows directly when the yield stresses are expressed as functions of temperature and moisture content.

The obvious association, implied by the term "work-hardening," between the work used to produce plastic flow and the hardening created,

suggests the hypothesis that the degree of hardening is a function only of the total plastic work, and is otherwise independent of the strain path. In order for plastic work to be performed, the state of stress must be on the yield surface, i.e., the stress state must also satisfy the condition given by Eq. (3). To enforce this constraint, the Lagrange multiplier  $d\lambda$  is used [19].

Relating the six parameters of anisotropy to the strain history is a complicated problem. It can be simplified, however, by the assumption that the yield stresses must increase in proportion with strain hardening. This assumption is justified by the fact that the directions of anisotropy in fibrous composites remain effectively the same during deformation. By analogy with the von Mises criterion for isotropic materials, Hill [18] suggested that if there is a functional relation between the equivalent stress  $\bar{\sigma}$  and the work  $W$ , there must be one between  $\bar{\sigma}$  and the effective (or equivalent) strain increment  $d\bar{\epsilon}$ . This is the analogue of the equivalent stress-equivalent strain curve for isotropic materials, the area under which is equal to the work per unit volume. These equations are of the form

$$\begin{aligned} \bar{\sigma}^2 &= \left[ \frac{3}{2} \frac{h^2}{F + G + H} \right] \\ &= \frac{3}{2} \left[ \frac{F(\sigma_2 - \sigma_3)^2 + G(\sigma_3 - \sigma_1)^2 + H(\sigma_1 - \sigma_2)^2}{F + G + H} \right. \\ &\quad \left. + \frac{2L\tau_{23}^2 + 2M\tau_{13}^2 + 2N\tau_{12}^2}{F + G + H} \right] \end{aligned} \quad (4)$$

and

$$\begin{aligned} d\bar{\epsilon} &= \left[ \frac{2}{3}(F + G + H) \right]^{1/2} \left[ \frac{F(Gd\epsilon_2 - Hd\epsilon_3)^2 + G(Hd\epsilon_3 - Fd\epsilon_1)^2 + H(Fd\epsilon_1 - Gd\epsilon_2)^2}{(FG + GH + HF)^2} \right. \\ &\quad \left. + \frac{2(d\gamma_{23})^2}{L} + \frac{2(d\gamma_{13})^2}{M} + \frac{2(d\gamma_{12})^2}{N} \right]^{1/2} \end{aligned} \quad (5)$$

If an effective stress-effective plastic strain curve is then constructed, the slope of such a curve at any point will be

$$H' = \frac{d\bar{\sigma}}{d\bar{\epsilon}^P} \quad (6)$$

Continuing in this manner [9] yields the desired form for the stress-strain relation

$$\{d\sigma\} = [C^P] \{d\epsilon\} \quad (7)$$

where

$$[C^P] = \begin{bmatrix} C_{11} - \frac{A_1^2}{B} & C_{12} - \frac{A_1 A_2}{B} & C_{13} - \frac{A_1 A_3}{B} & C_{14} - \frac{A_1 A_4}{B} & C_{15} - \frac{A_1 A_5}{B} & C_{16} - \frac{A_1 A_6}{B} \\ & C_{22} - \frac{A_2^2}{B} & C_{23} - \frac{A_2 A_3}{B} & C_{24} - \frac{A_2 A_4}{B} & C_{25} - \frac{A_2 A_5}{B} & C_{26} - \frac{A_2 A_6}{B} \\ & & C_{33} - \frac{A_3^2}{B} & C_{34} - \frac{A_3 A_4}{B} & C_{35} - \frac{A_3 A_5}{B} & C_{36} - \frac{A_3 A_6}{B} \\ & \text{Symmetric} & & C_{44} - \frac{A_4^2}{B} & C_{45} - \frac{A_4 A_5}{B} & C_{46} - \frac{A_4 A_6}{B} \\ & & & & C_{55} - \frac{A_5^2}{B} & C_{56} - \frac{A_5 A_6}{B} \\ & & & & & C_{66} - \frac{A_6^2}{B} \end{bmatrix} \quad (8)$$

is the plastic stiffness matrix, and

$$B = \frac{4}{9} \bar{\sigma}^2 H' + A_1^* \bar{\sigma}_1 + A_2^* \bar{\sigma}_2 + A_3^* \bar{\sigma}_3 \\ + 2A_4^* \bar{\tau}_{23} + 2A_5^* \bar{\tau}_{13} + 2A_6^* \bar{\tau}_{12} \quad (9)$$

where the  $A_i$  ( $i = 1, \dots, 6$ ) are elements of the  $\{A\}$  vector, and

$$\begin{aligned}
 \sigma_1^* &= [H(\sigma_1 - \sigma_2) + G(\sigma_1 - \sigma_3)]/(F + G + H) \\
 \sigma_2^* &= [F(\sigma_2 - \sigma_3) + H(\sigma_2 - \sigma_1)]/(F + G + H) \\
 \sigma_3^* &= [G(\sigma_3 - \sigma_1) + F(\sigma_3 - \sigma_2)]/(F + G + H) \\
 \tau_{23}^* &= L\tau_{23}/(F + G + H) \\
 \tau_{13}^* &= M\tau_{13}/(F + G + H) \\
 \tau_{12}^* &= M\tau_{12}/(F + G + H)
 \end{aligned} \tag{10}$$

For an orthotropic material, i.e., a material with three planes of symmetry,

$$\{A\} = \left\{ \begin{array}{c} C_{11}\sigma_1^* + C_{12}\sigma_2^* + C_{13}\sigma_3^* \\ C_{12}\sigma_1^* + C_{22}\sigma_2^* + C_{23}\sigma_3^* \\ C_{13}\sigma_1^* + C_{23}\sigma_2^* + C_{33}\sigma_3^* \\ 2C_{44}\tau_{23}^* \\ 2C_{55}\tau_{13}^* \\ 2C_{66}\tau_{12}^* \end{array} \right\} \tag{11}$$

To apply this method of analysis to fibrous composites, the material properties in the 1, 2, and 3 directions are needed. If the material is transversely isotropic, the properties in the 2 and 3 directions are the same. For mathematical consistency with the formulation, a relation between the effective stress and the effective strain is required. Furthermore, the dependence of the material properties on temperature and moisture content is required if hygrothermal loadings are to be handled, and the actual material

response under varying conditions of environment is to be considered. These data were generated with the 2-D micromechanics analysis presented earlier.

Richard and Blacklock [16] have developed a three-parameter model which was found to fit stress-strain curves very accurately. This model is of the form shown previously in Eq. (1) for shear stress-strain response. Since the shape of an effective stress-effective strain curve is similar to a uniaxial tensile or shear stress-strain curve, a similar equation for the effective stress-effective strain can be written as

$$\bar{\sigma} = \frac{\bar{E}\bar{\epsilon}}{[1 + |\frac{\bar{E}\bar{\epsilon}}{\bar{\sigma}_0}|^n]^{\frac{1}{n}}} \quad (12)$$

where  $\bar{\sigma}$  is the effective stress and  $\bar{\epsilon}$  is the effective strain as defined previously. The two independent parameters  $\bar{\sigma}_0$  and  $n$ , together with the third parameter  $\bar{E}$ , which is the initial slope of the curve, are selected to best fit the experimental data.

By fitting Eq. (12) to the effective stress-effective strain curves obtained for different temperatures and moisture contents, a functional relationship of the parameters  $\bar{E}$ ,  $\bar{\sigma}_0$ , and  $n$  to temperature and moisture can be established. In a similar manner, functional relationships can also be found for all other material properties.

The 2-D micromechanics analysis was used to predict stress-strain curves for longitudinal tension, transverse tension, longitudinal shear and transverse shear at room temperature, dry conditions (Figures 6 through 9). These are plotted as effective stress-effective strain curves in Figure 12. The anisotropy parameters  $F$ ,  $G$ ,  $H$ ,  $L$ ,  $M$  and  $N$  were calculated as in Reference [9], i.e.,

$$\begin{aligned} 2F &= \frac{1}{(\sigma_2^y)^2} + \frac{1}{(\sigma_3^y)^2} - \frac{1}{(\sigma_1^y)^2} \\ 2G &= \frac{1}{(\sigma_3^y)^2} + \frac{1}{(\sigma_1^y)^2} - \frac{1}{(\sigma_2^y)^2} \\ 2H &= \frac{1}{(\sigma_1^y)^2} + \frac{1}{(\sigma_2^y)^2} - \frac{1}{(\sigma_3^y)^2} \end{aligned} \quad (13)$$

AS /3501-6 EFF. STRESS  
 21 DEG. C 0.0% MOIS.  
 FIBER VOLUME 60%

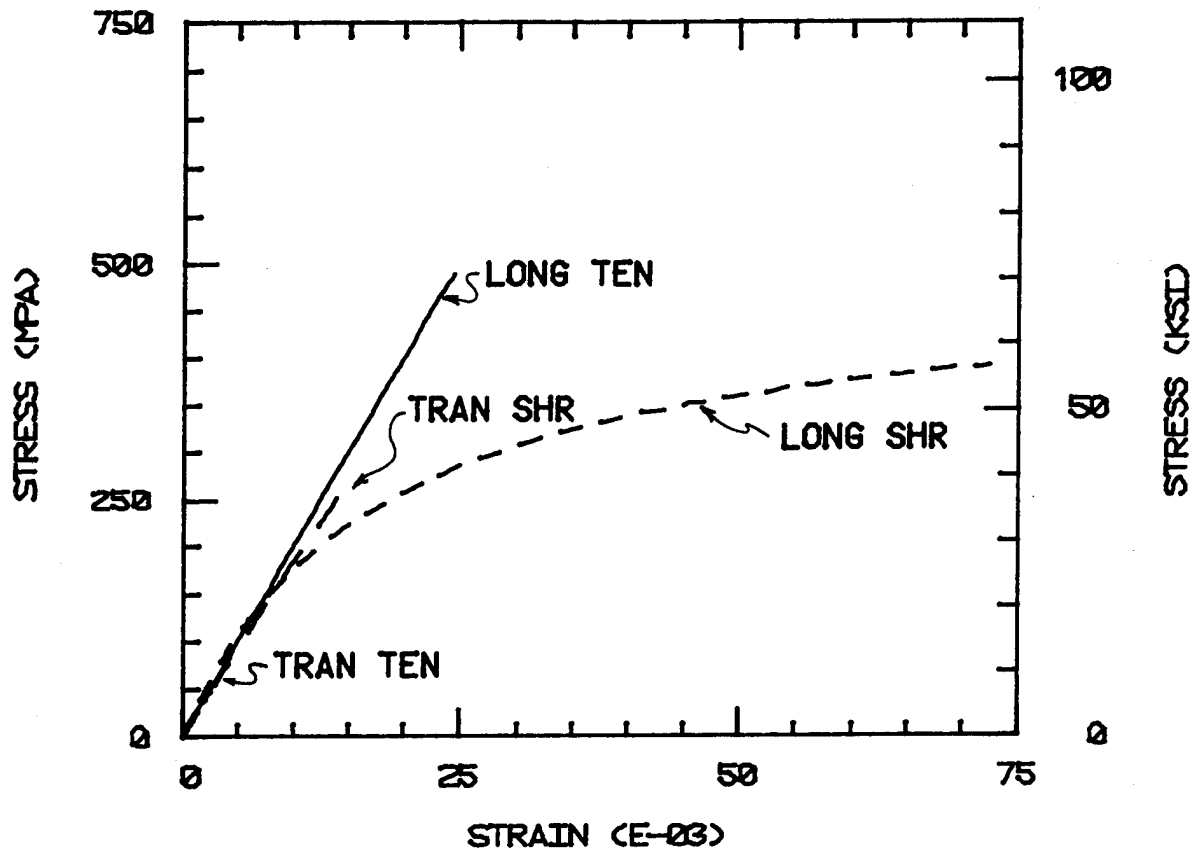


Figure 12. Effective Stress-Effective Strain Plots, Room Temperature, Dry Conditions.



$$2L = \frac{1}{(\tau_{23}^y)^2} , \quad 2M = \frac{1}{(\tau_{13}^y)^2} , \quad 2N = \frac{1}{(\tau_{12}^y)^2} \quad (13 \text{ cont.})$$

where  $\sigma_i^y$ ,  $\tau_i^y$  are the yield stresses with respect to the material coordinate axes. Ideally, the four curves, representing four different types of loading, should merge into one effective stress-effective strain curve with the proper selection of the anisotropy parameters of Eq. (13). Yield stress values used to compute the anisotropy parameters for Figure 13 are listed in Table 4. These so-called yield values in Table 4 were arbitrarily selected to produce the most consistent effective stress-effective strain plot. Comparing the yield stresses in Table 4 to the stress-strain curves plotted in Figures 6 through 9, one can see that the selected values are reasonable, but definitely arbitrary. As used in this work, these yield values represent the anisotropy of the yield surface only. Obviously the longitudinal tension results exhibit no apparent yield behavior.

Effective stress-effective strain plots for the remaining three environmental conditions are plotted in Figures 13 through 15. As in Figure 12, the four loading cases coincide as one effective stress-effective strain plot only during the initial portion of the curve. Longitudinal and transverse tension curves remain linear when plotted as effective stress-effective strain, while longitudinal and transverse shear curves plot as nonlinear effective stress-effective strain.

At least two possible sources for this difficulty exist. First, there may be a problem in the 2-D micromechanics analysis which precludes obtaining a self-consistent set of composite property data. However, the 2-D micromechanics data is elastically self consistent and the predicted stress-strain response does tend to emulate available experimental data. The second possible source of error may lie in the assumption of proportional hardening. As the longitudinal tension results exhibit little or no inelastic behavior, the application of any hardening is probably in error. Other causes of this anomaly in

TABLE 4. YIELD VALUES USED TO CALCULATE THE ANISOTROPIC  
YIELD PARAMETERS. (ALL VALUES IN KSI)

| Stress<br>Component     | 21°C, dry | 80°C, dry | 160°C, dry | 21°C, 1% M |
|-------------------------|-----------|-----------|------------|------------|
| $\sigma_1$              | 80        | 100       | 110        | 110        |
| $\sigma_2 = \sigma_3$   | 25        | 30        | 25         | 25         |
| $\tau_{23}$             | 10        | 10        | 10         | 10         |
| $\tau_{13} = \tau_{12}$ | 9         | 9         | 9          | 9          |

AS /3501-6 EFF. STRESS  
80 DEG. C 0.0% MOIS.  
FIBER VOLUME 60%

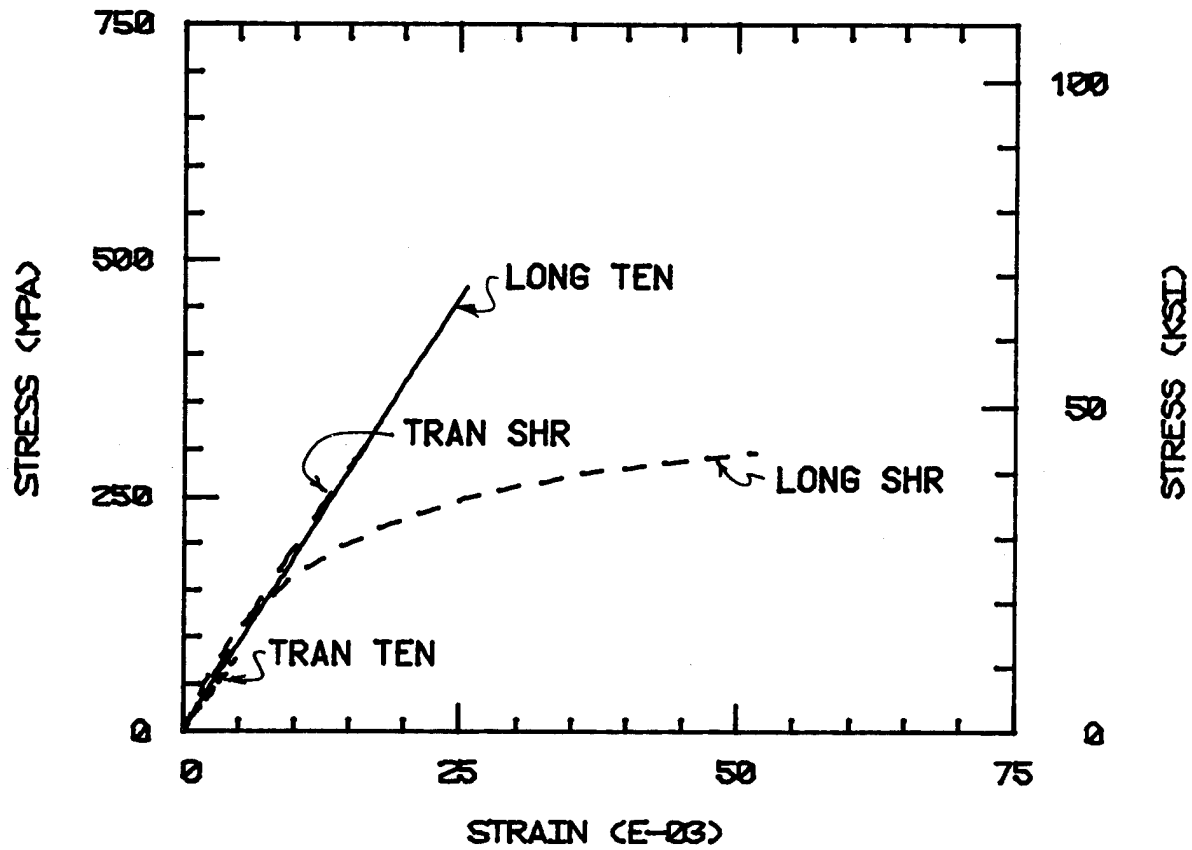


Figure 13. Effective Stress-Effective Strain Plots, 80°C, Dry Conditions.

AS /3501-6 EFF. STRESS  
 160 DEG. C 0.0% MOIS.  
 FIBER VOLUME 60%

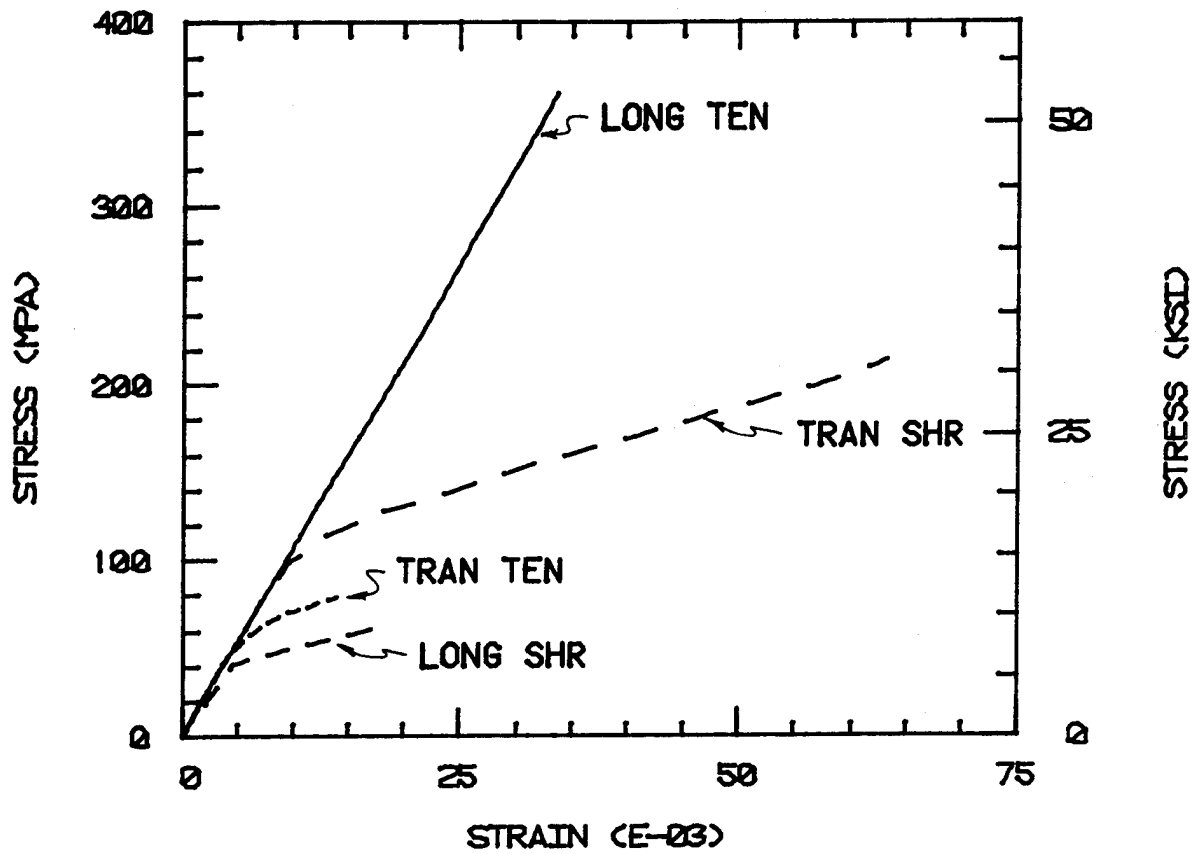


Figure 14. Effective Stress-Effective Strain Plots, 160°C, Dry Conditions.

AS /3501-6 EFF. STRESS  
 21 DEG. C 1.0% MOIS.  
 FIBER VOLUME 60%

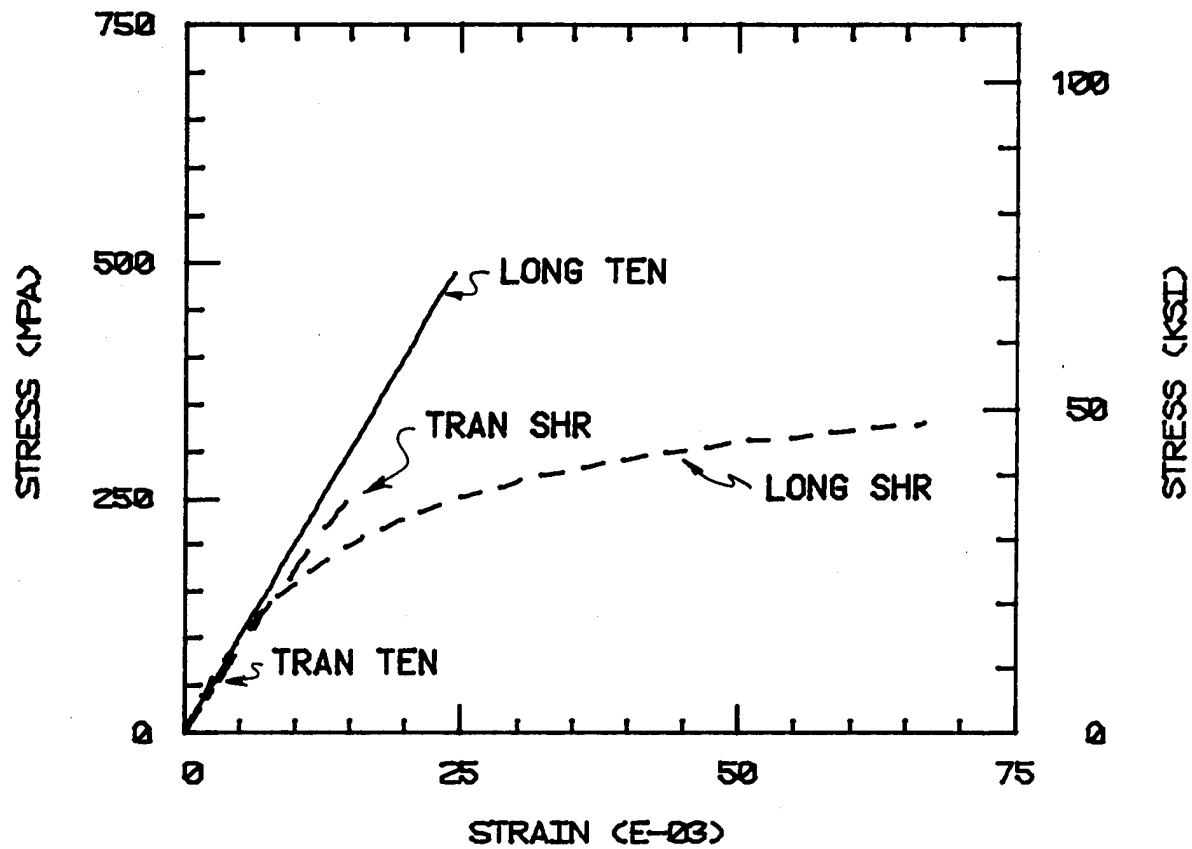


Figure 15. Effective Stress-Effective Strain Plots, Room Temperature, One Weight Percent Moisture Conditions.

predicted effective stress-effective strain behavior may exist, but must be left to further research.

Nonlinear stress-strain response in unidirectional composite lamina takes place primarily during shear loading. This has been observed experimentally [5] as well as being predicted by the 2-D micromechanics analysis. Therefore, even though the effective stress-effective strain concept is not complete in its description of normal and shear loading, it was important to include the nonlinear shear behavior of the lamina in the 3-D models. To circumvent the effective stress-effective strain anomaly, the  $0^\circ$  degree and  $90^\circ$  plies were modelled as linear elastic as they were to be subjected primarily to normal loads. The  $45^\circ$  ply properties were input in terms of nonlinear effective stress-effective strain behavior based on the shear results. The Richard-Blacklock effective stress-effective strain curves used to model the  $45^\circ$  plies are plotted for the different environments in Figure 16.

#### 4.5 Summary

To summarize, material properties for the 3-D models were obtained from 2-D generalized plane strain micromechanics computations. Constituent properties for the Hercules AS fiber and the 3501-6 epoxy matrix were used to predict a set of 3-D material properties for an AS/3501-6 graphite/epoxy lamina, including thermal cure induced response as well as the effect of absorbed moisture. This set of material properties was presented in Figures 6 through 11.

Problems were encountered in reducing data from the four different loading modes into one selfconsistent effective stress-effective strain curve. Normal loading behavior was linear while shear loading behavior was nonlinear. Further pursuit of this anomaly was beyond the scope of the present program, but should be examined in future research. To circumvent the problem, plies subjected to primarily normal loading were modeled as linear elastic, consistent with the predicted response to normal (longitudinal and transverse) loadings. Plies which would be expected to be dominated by shear loading were modeled using nonlinear material properties based on shear response predictions.

AS /3501-6 45 DEG PLIES

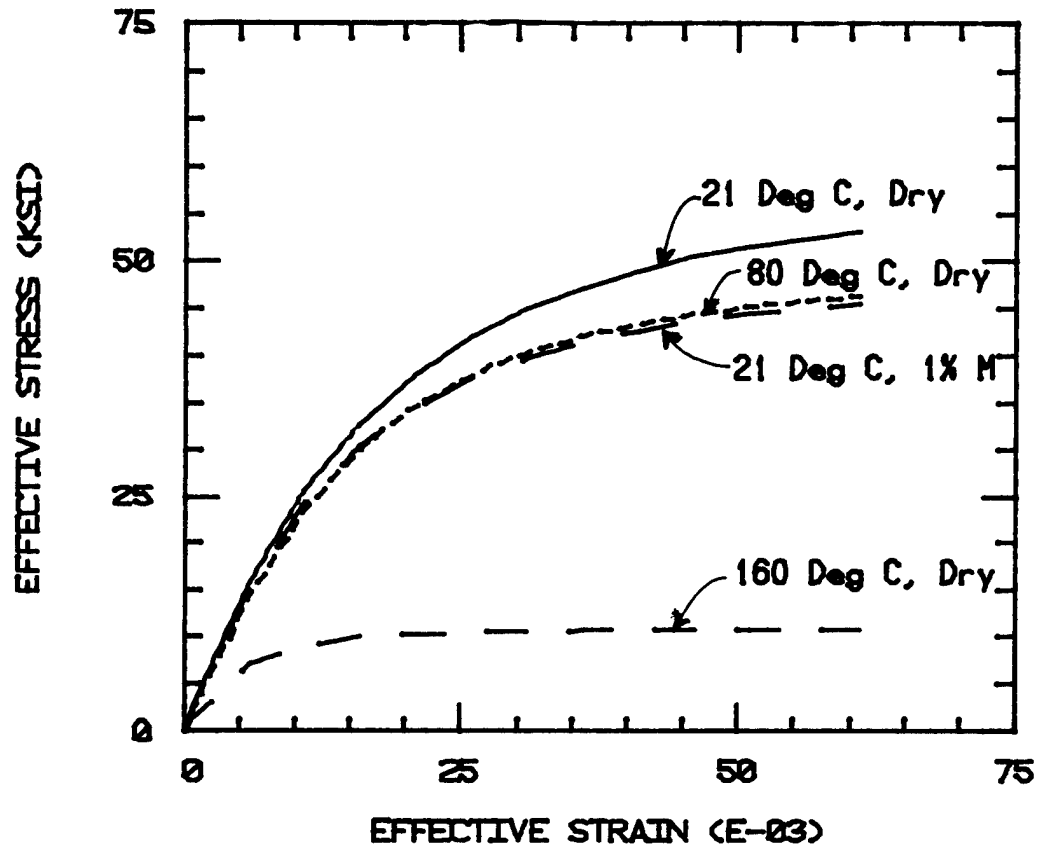


Figure 16. Effective Stress-Effective Strain Plot Used to Model  $\pm 45^\circ$  Ply Material Properties as a Function of Temperature and Moisture.

## SECTION 5

### MICROMECHANICAL ANALYSIS OF POROSITY

During the third-year study [3] and continuing in the present fourth-year study, porosity was deliberately induced in selected laminates, as discussed in Section 1. Experimental results are presented in References [3,4]. This induced porosity (2.5 to 4.5 percent by volume) did reduce the strength and strain to failure of the various composite laminates. The greatest influence was on the unidirectional laminates, with the F-18 laminates being affected less. Results, along with a detailed summary, are contained in Reference [4].

It was decided to use the 2-D analysis to model pores of cross-sectional dimensions comparable to the diameters of individual graphite fibers (which are in the 6 to 8  $\mu\text{m}$  range). This will be termed microporosity. The analysis of larger pores, observed to occur predominately at ply interfaces, will require the use of a full 3-D analysis. This will be addressed in a future study. The analysis of microporosity is presented in the remainder of this section.

#### 5.1 2-D Analysis Capabilities

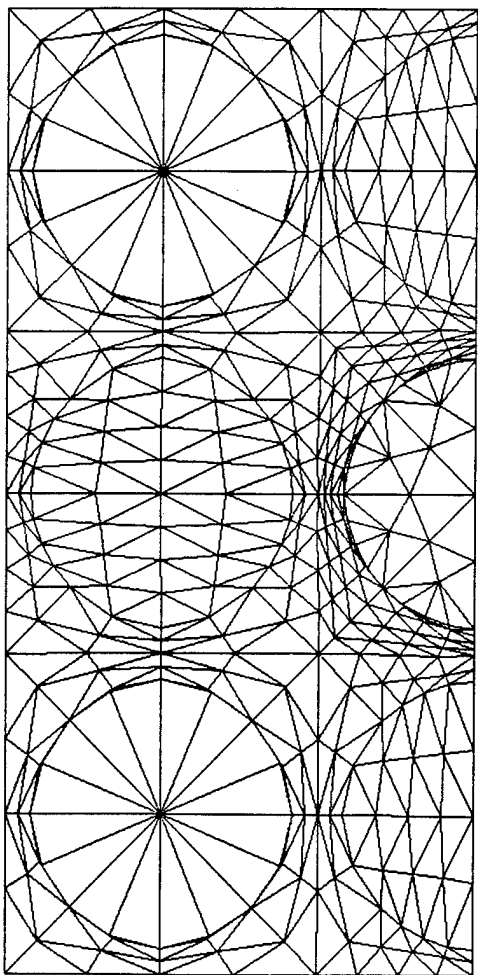
The two-dimensional, generalized plane strain finite element analysis used here to study microporosity was originally developed within the Composite Materials Group at the University of Wyoming a number of years ago [7,8]. This analysis and the associated computer programs have been continually improved since that time, as summarized in Section 1.

The analysis is currently capable of modeling longitudinal shear loading and crack propagation, temperature- and moisture-induced stresses, nonlinear matrix material response, and anisotropic fibers.

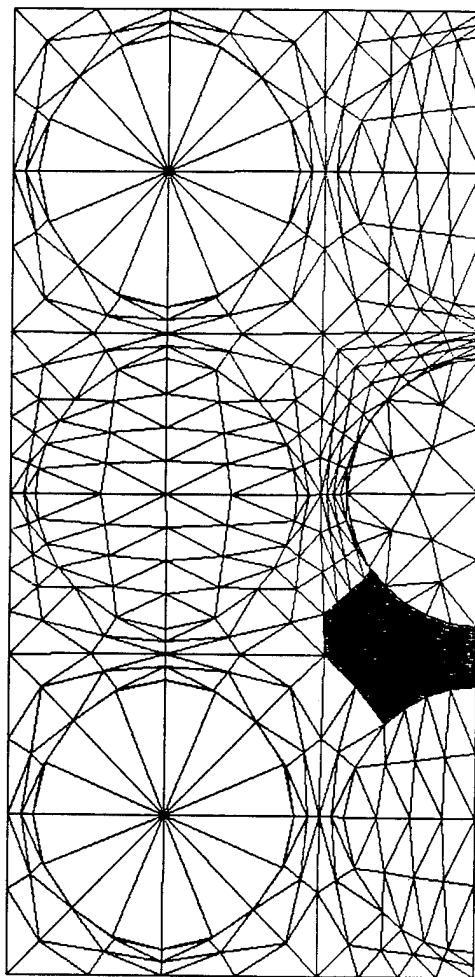
#### 5.2 Porosity Model

Using the 2-D finite element analysis, the grid model shown in Figure 17a was constructed. This model represents one quadrant of a repeating square array of graphite fibers in an epoxy matrix. It





a) no porosity



b) 2.9 percent porosity

Figure 17. Two-Dimensional Finite Element Grids to Model Microporosity, 60 Percent Fiber Volume (640 Elements).

contains three full fibers and three half fibers (centered on a boundary axis of symmetry). Figure 17b shows the same finite element grid, but with a micropore added, as shown by the solid black region. How this porosity is distributed in a large array of fibers can better be seen in Figure 18, the one quadrant of a repeating unit cell of Figure 17b also being indicated. As can be seen, a single micropore is small relative to the diameter of a single fiber. In the present model it is assumed to partially separate two adjacent fibers, occupying well over 50 individual finite elements. It should be noted that with the very fine element grid used (Figure 17a), almost any size or shape pore can be modeled. The location and geometry chosen here is arbitrary, but does represent the type of porosity observed in actual composites when they were sectioned and examined under a microscope. It was also desired to model the actual density of voids, which required the extensive model containing three full plus three half fibers. In this way a low void volume (Figures 17b and 18 represent a fiber volume of 60 percent and a void volume of 2.9 percent) typical of the actual composites fabricated by Northrop for the present study could be modeled while maintaining good grid refinement around the individual small void.

In any future studies, other micropore geometries, locations, and densities could readily be simulated, simply by redefining which finite elements are to represent the pore. The results presented here are intended primarily to demonstrate the capabilities of the analysis.

It should be noted that, because the specific finite element analysis used here is two-dimensional (generalized plane strain), there is no variation of geometry along the axes of the fibers. Thus the micropore is modeled as a cylindrical void, parallel to the fibers. Microscopic examination of actual composites indicated that this is a reasonable representation. The micropores, while not continuous, were typically highly elongated, presumably due to the flow of the resin matrix parallel to the fibers during the consolidation process. If a compact micropore were to be modeled, a 3-D analysis would be required. Such an analysis would be similar to that required to model a large void in a laminate, as previously discussed.

### 5.3 Predicted Response

Although any combination of tension, compression and shear stresses

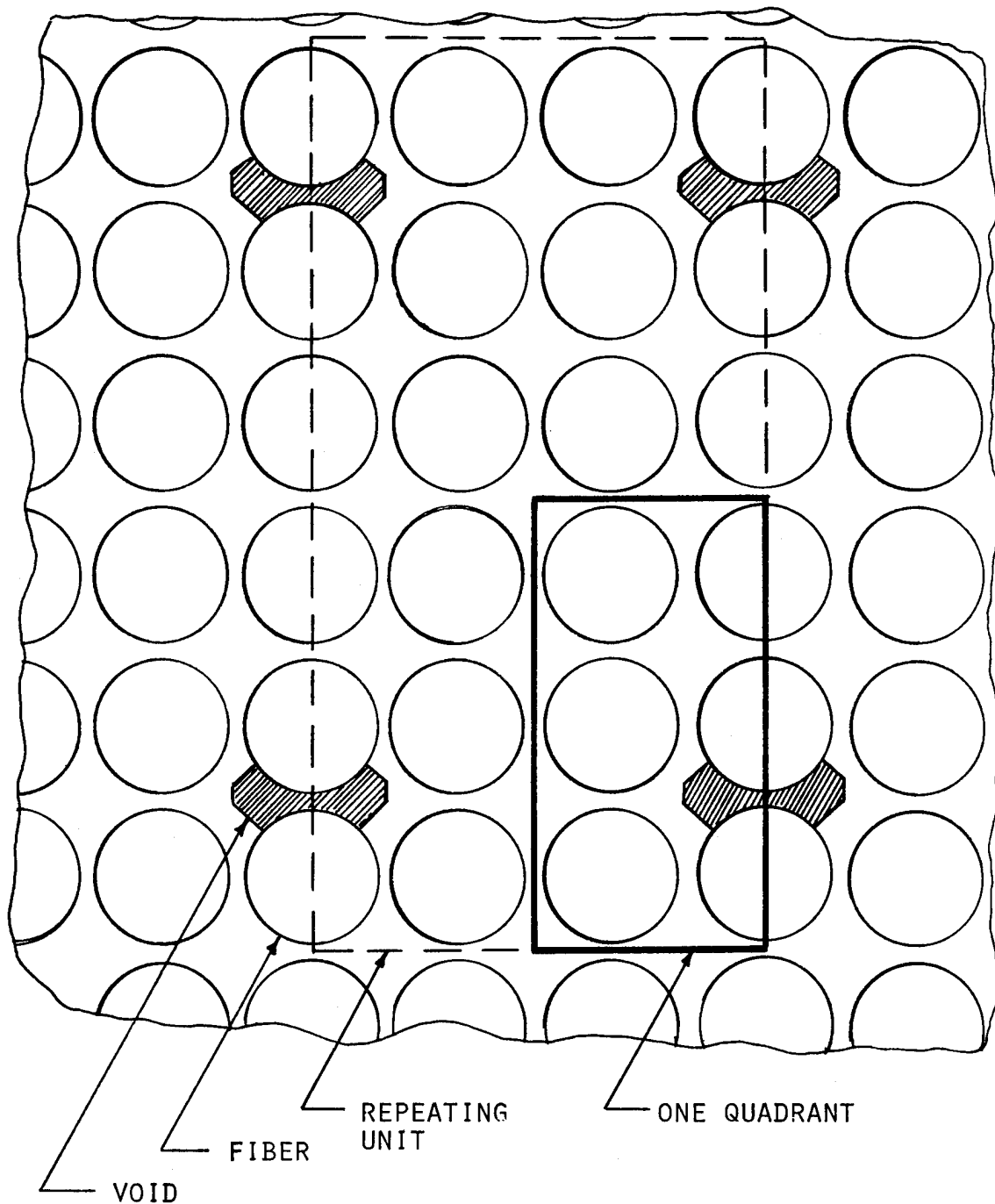


Figure 18. Square Array of Fibers in a Matrix Containing 2.9 Percent Microporosity, with One Quadrant of a Typical Repeating Unit Indicated (Fiber Volume = 60 Percent).

can be applied, results for only uniaxial loadings will be presented here. Specifically, these include longitudinal tension, transverse tension, and longitudinal shear. These represent fundamental loadings of primary interest. Residual stresses due to cooldown-induced thermal stresses and moisture absorption swelling stresses can also be modeled readily by the present analysis. Thermal residual stresses were included in all of the results presented here.

In all cases, the finite element models of both Figure 17a (no porosity) and Figure 17b (one pore in the array) were run, to determine the influence of the micropore. An octahedral shear yield criterion and an octahedral shear failure criterion were used in the present predictions, although any other criteria could be used if desired.

The stress and strain contour plotting routine is presently programmed to display any or all of eight different quantities, viz, octahedral shear stress, octahedral shear strain, each of the three principal stresses, the maximum shear stress, and the normal and shear stress distributions around the fiber-matrix interfaces. The loadings are applied in increments, to accommodate inelastic material response and crack propagation, and as many as 10 or 15 increments may be used to attain the failure stress. Stress and strain contours can be plotted for each load increment. Hence a huge number of contour plots can be made available for detailed study. This was, in fact, done in the present study. However, only selected plots will be presented here, to demonstrate the capabilities of the analysis and to indicate predicted trends of the composite response.

#### 5.3.1 Longitudinal Tension

As an example, a set of plots of the first six quantities previously listed, viz, octahedral shear stress, octahedral shear strain, the three principal stresses, and the maximum shear stress (interface stresses are not included here, but are available) are presented in Figures 19a through f, respectively, for the porosity grid, and an applied longitudinal stress of 20 ksi. This represents the first increment of applied load, as indicated in each figure heading. Other information contained in each computer-generated heading includes a general descriptive caption, e.g., the loading mode, longitudinal tension, and the grid model used (this line is not included in Figure

OCTAHEDRAL SHEAR STRESS CONTOURS

ENP = 23.00 DEG. C MIDS = 0.00 % INCREMENT NO. = 1 PLOT NO. = 8

XX = 0.00 KSI SYY = 0.00 KSI SZZ = 20.00 KSI SYZ = 0.00 KSI

XY = 0.00 KSI MIN = 5.92 MAX = 59.23 A = 10.35

B = 14.70 C = 19.22 D = 23.05 E = 28.08

F = 32.51 G = 36.94 H = 41.37 I = 45.80

OCTAHEDRAL SHEAR STRESS CONTOURS

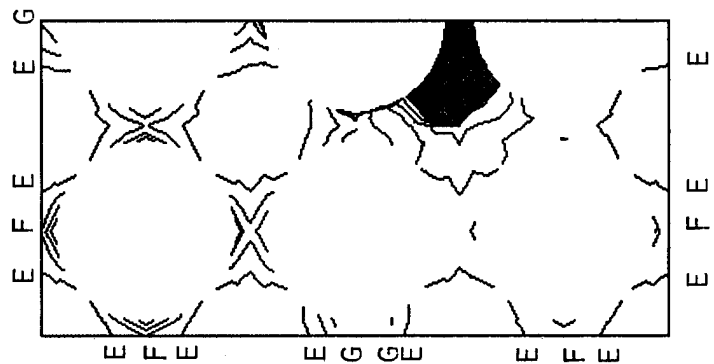
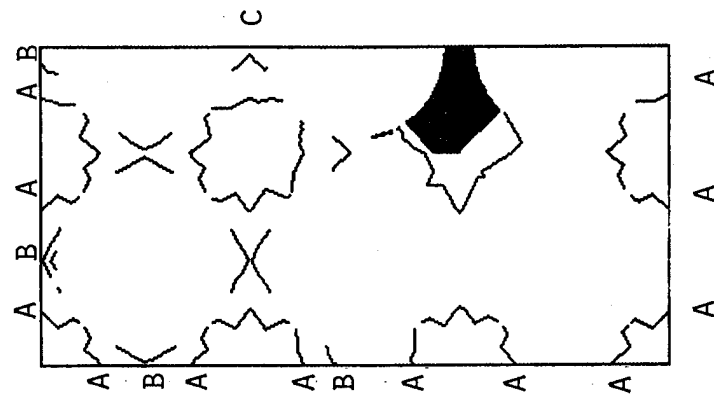
ENP = 23.00 DEG. C MIDS = 0.00 % INCREMENT NO. = 1 PLOT NO. = 7

XX = 0.00 KSI SYY = 0.00 KSI SZZ = 20.00 KSI SYZ = 0.00 KSI

XY = 0.00 KSI MIN = 3.28 KSI MAX = 3.28 KSI A = .38 KSI

B = .00 KSI C = .98 KSI D = 1.31 KSI E = 1.64 KSI

F = 1.97 KSI G = 2.38 KSI H = 2.82 KSI I = 2.95 KSI



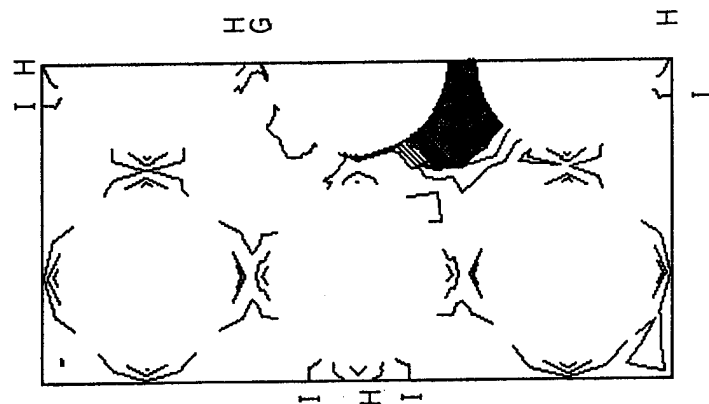
a) Octahedral Shear Stress (ksi)

b) Octahedral Shear Strain

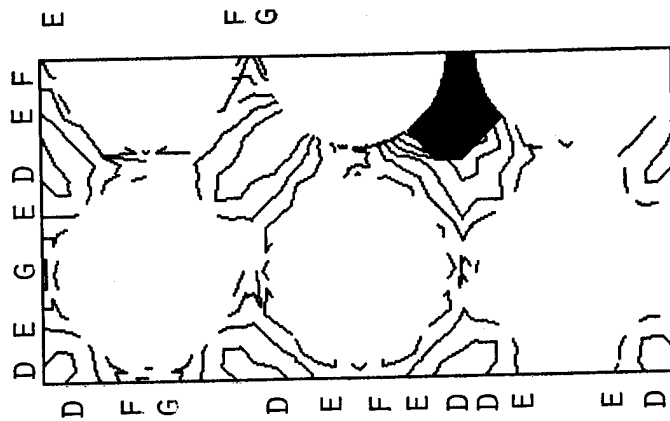
Figure 19. Typical Stress and Strain Contour Plots; Longitudinal Tensile Loading,  $\bar{\sigma}_z = 20$  ksi, 2.9% Porosity.

FIRST PRINCIPAL STRESS CONTOURS  
 TEMP = 23.00 DEG. C MIDS = 0.00 % INCREMENT NO. = 1 PLOT NO. = 5  
 SX = 0.00 KSI SY = 0.00 KSI SZ = 20.00 KSI SYZ = 0.00 KSI  
 SXZ = 0.00 KSI MIN = -0.00 KSI MAX = 4.00 KSI A = .40 KSI  
 B = .03 KSI C = 1.30 KSI D = 1.85 KSI E = 2.32 KSI  
 F = 2.78 KSI G = 3.24 KSI H = 3.70 KSI I = 4.17 KSI

SECOND PRINCIPAL STRESS CONTOURS  
 TEMP = 23.00 DEG. C MIDS = 0.00 % INCREMENT NO. = 1 PLOT NO. = 4  
 SX = 0.00 KSI SY = 0.00 KSI SZ = 20.00 KSI SYZ = 0.00 KSI  
 SXZ = 0.00 KSI MIN = -0.00 KSI MAX = 4.00 KSI A = .41 KSI  
 B = .02 KSI C = 1.23 KSI D = 1.84 KSI E = 2.05 KSI  
 F = 2.46 KSI G = 2.67 KSI H = 3.20 KSI I = 3.60 KSI



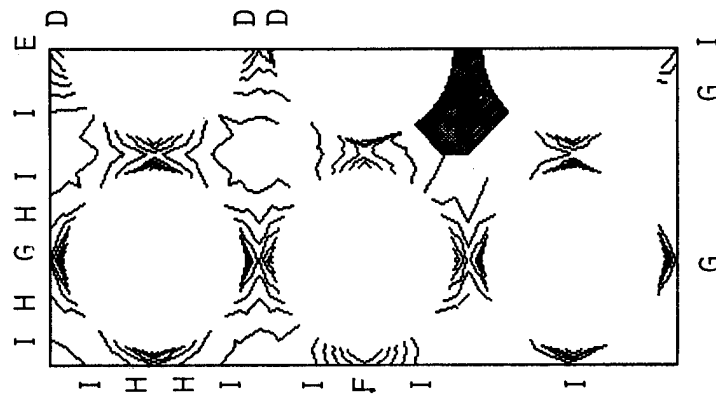
c) First Principal Stress (ksi)



d) Second Principal Stress (ksi)

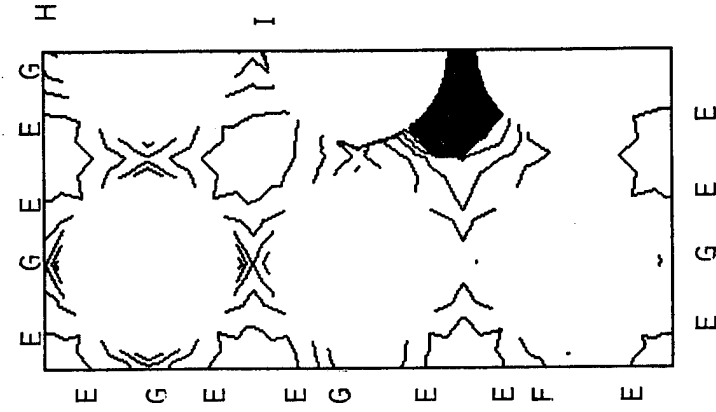
Figure 19 (Continued). Typical Stress and Strain Contour Plots; Longitudinal Tensile Loading,  $\bar{\sigma}_z = 20$  ksi, 2.9% Porosity.

THIRD PRINCIPAL STRESS CONTOURS  
 TYP = 23.00 DES. C MITS = 0.00 % INCREMENT NO. = 1 PLOT NO. = 5  
 SX = 0.00 KSI SY = 0.00 KSI SZ = 20.00 KSI SYZ = 0.00 KSI  
 SZ = 0.00 KSI MIN = -4.65 KSI MAX = 1.44 KSI A = -4.04 KSI  
 B = -3.43 KSI C = -2.82 KSI D = -2.21 KSI E = -1.00 KSI  
 F = -.30 KSI G = -.30 KSI H = .22 KSI I = .63 KSI



e) Third Principal Stress (ksi)

MAXIMUM SHEAR STRESS CONTOURS  
 TYP = 23.00 DES. C MITS = 0.00 % INCREMENT NO. = 1 PLOT NO. = 0  
 SX = 0.00 KSI SY = 0.00 KSI SZ = 20.00 KSI SYZ = 0.00 KSI  
 SZ = 0.00 KSI MIN = -.00 KSI MAX = 5.54 KSI A = .35 KSI  
 B = .71 KSI C = 1.00 KSI D = 1.41 KSI E = 1.77 KSI  
 F = 2.12 KSI G = 2.40 KSI H = 2.83 KSI I = 3.18 KSI



f) Maximum Shear Stress (ksi)

Figure 19 (Concluded). Typical Stress and Strain Contour Plots; Longitudinal Tensile Loading,  $\bar{\sigma}_z = 20$  ksi, 2.9% Porosity.

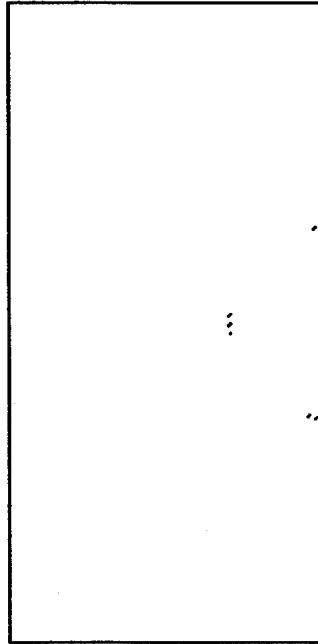
19). The first line in Figure 19 indicates the quantity plotted. The second line indicates the temperature and moisture conditions for the increment being plotted. Here, the temperature is 23°C (room temperature), and no moisture is present. The final entry on the second line, the plot number, is for bookkeeping purposes only. The four entries on Line 3 and the first entry on Line 4 are the cumulative values of the applied stresses, i.e.,  $\bar{\sigma}_x$ ,  $\bar{\sigma}_y$ ,  $\bar{\sigma}_z$ ,  $\bar{\tau}_{yz}$  and  $\bar{\tau}_{xz}$ . As indicated in Figure 19, at Increment No. 1 only an applied longitudinal stress,  $\bar{\sigma}_z = 20$  ksi, is acting. The second and third entries on Line 4 indicate the minimum and maximum values of the plotted quantity. Finally, the letters A through I are the contour labels indicating the magnitudes of the plotted contours. For example, in Figure 19a, Contour E represents an octahedral shear stress value of 1.64 ksi.

Contour plots such as the samples presented in Figure 19 provide much quantitative information regarding the response of the matrix to applied stresses. (Contours in the fibers can also be plotted, if of interest, although not included here.) However, for the present purposes, attention will be focused instead on the extent of yielding and crack propagation, as being simpler to follow. This can be plotted, excluding the contour values, as indicated in Figures 20 and 21.

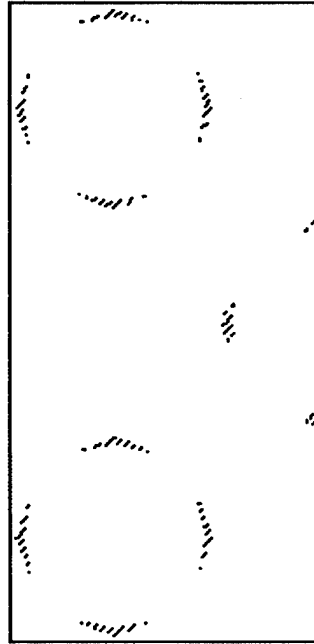
Figures 20a through d indicate the extent of yielding (shown shaded) as a function of increasing applied longitudinal tensile stress, for the nonporous composite. Plots for  $\bar{\sigma}_z$  equal to 120 ksi, 160 ksi, 230 ksi, and 250 ksi are shown, representing loading Increments 6, 8, 13, and 15, respectively. That is, only selected results are shown here, although plots for every increment were available. As indicated in the plot headings, elements still in the elastic range of material response are shown unshaded (white), elements in the inelastic (plastic) range are shown shaded (grey), and failed elements (cracks) are shown as solid black areas.

The first indication of yielding occurred at  $\bar{\sigma}_z = 120$  ksi (Figure 20a) around the middle fiber centered on the right boundary of the model. Actually, because of the regularity of the periodic square array and the absence of porosity, yielding should have theoretically occurred simultaneously at every fiber, in identical patterns. The minor deviation indicated in Figure 20a is due to the use of a

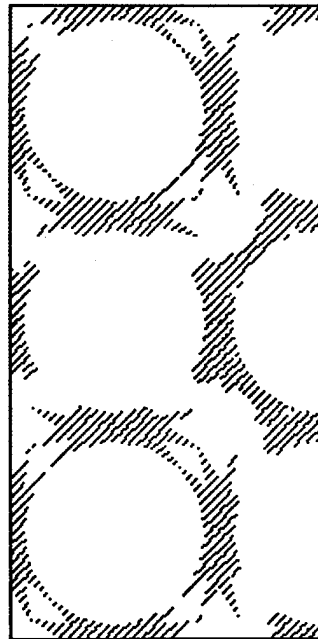




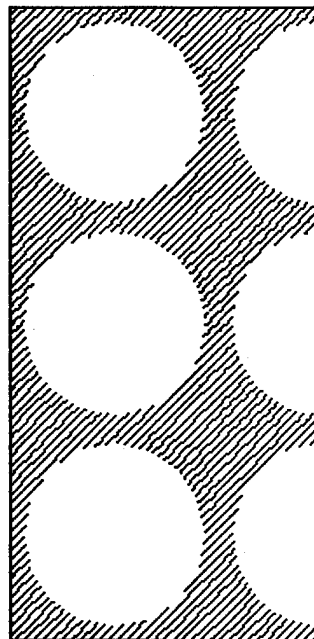
a)  $\bar{\sigma}_z = 120$  ksi



b)  $\bar{\sigma}_z = 160$  ksi

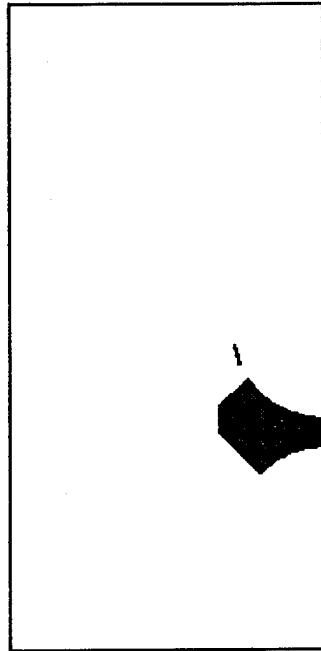


c)  $\bar{\sigma}_z = 230$  ksi

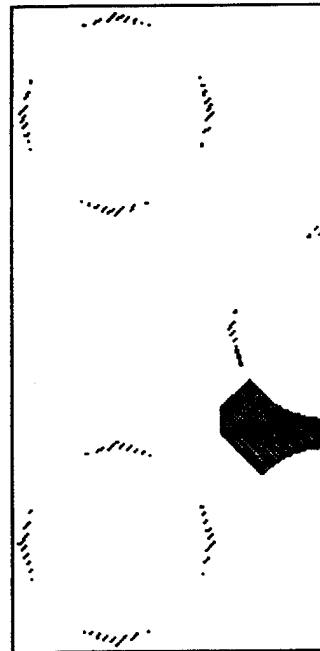


d)  $\bar{\sigma}_z = 250$  ksi

Figure 20. Longitudinal Tension, No Porosity; Extent of Yielding and Crack Propagation With Increasing Applied Stress (Elastic Elements are White, Plastic Elements are Shaded, Failed Elements are Black).



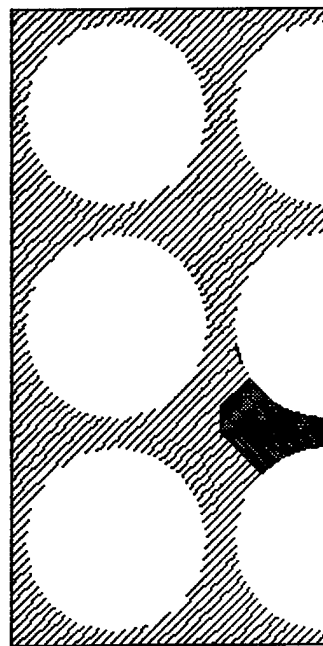
a)  $\bar{\sigma}_z = 40$  ksi



b)  $\bar{\sigma}_z = 160$  ksi



c)  $\bar{\sigma}_z = 230$  ksi



d)  $\bar{\sigma}_z = 250$  ksi

Figure 21. Longitudinal Tension, 2.9 Percent Porosity; Extent of Yielding and Crack Propagation With Increasing Applied Stress (Elastic Elements are White, Plastic Elements are Shaded, Failed Elements are Black).

nonuniform finite element grid (see Figure 17a), the grid resolution being much finer around the fiber where first yielding is indicated. This yielding pattern is as expected, and of no special significance. At 160 ksi (Figure 20c) the yielding has spread to the boundaries of other fibers, and at 230 ksi (Figure 20c) it is extensive. At 250 ksi (Figure 20d) the matrix has completely yielded, but no crack initiation has occurred yet. At an applied stress of 318 ksi the fibers all fail simultaneously, which also defines composite failure.

Figure 21 represents corresponding results for the composite containing a micropore. In Figure 21a, at an applied stress of only 40 ksi, a small crack is indicated at the fiber-matrix interface near the pre-existing pore (the large black area). Little else happens until  $\bar{\sigma}_z = 160$  ksi (Figure 21b), at which load level the yielding first initiated at 140 ksi has spread to the extent shown. This is essentially the same yielding pattern as indicated at the same applied stress level for the nonporous composite (Figure 20b). Figures 21c and d likewise correspond to Figures 20c and d. Failure is predicted at 317.6 ksi, i.e., only about 400 psi less than for the nonporous composite (due to less matrix material available to carry load).

The conclusion is that microporosity is predicted to have little influence on a unidirectional composite subjected to longitudinal tension. As expected, the porosity introduces little more of a stress concentration than the fibers themselves. In an actual composite, where the cylindrical pores are of finite length (in the fiber direction), this axial discontinuity can be expected to cause some degradation. To model this three-dimensional geometry effect, a 3-D analysis would be required, as previously noted.

The composite stress-strain curves as predicted for longitudinal tensile loading are linear to failure, as expected due to the dominance of the graphite fiber properties, and essentially identical for both the nonporous and the porous composite. Hence these stress-strain plots are not shown here.

### 5.3.2 Transverse Tension

As previously noted, complete stress and strain contour plots for each transverse tensile loading increment were available for study. However, only plots representing the extent of yielding and crack

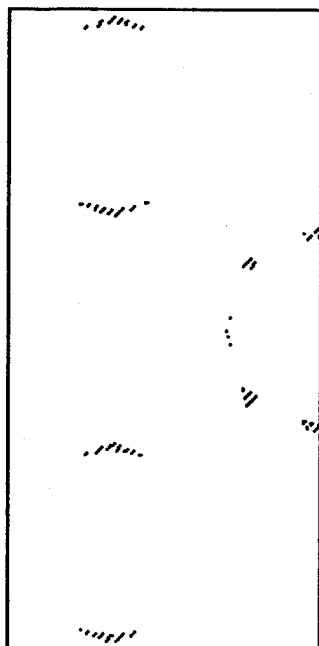
propagation will be included here.

As discussed in detail in Section 4, the material properties of the Hercules 3501-6 epoxy used as input data for the present analysis were experimentally generated using solid rod torsion (shear) tests. This results in octahedral shear strengths considerably higher than are generated using uniaxial tensile tests. This different response of polymer materials such as epoxy to different stress states is not yet adequately understood, and should be a topic of future investigations. In the interim, it is understood that the use of shear data as input to the micromechanics analysis will result in the prediction of transverse tensile strengths of the unidirectional composite which are considerably higher than those measured experimentally. Thus, little relevance will be placed on the magnitudes of the strengths predicted here; rather, the relative differences between the nonporous and porous composite response will be emphasized.

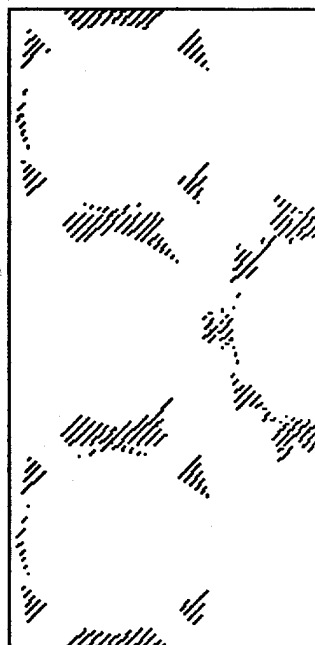
Figure 22 indicates the yield and failure sequence in the nonporous composite subjected to a transverse tensile loading. The first indication of yielding occurred at an applied transverse tensile stress (applied along the horizontal axis in Figure 22 and the subsequent figure) of 3 ksi; the extent at 6 ksi is shown in Figure 22a. It should be noted that the various stress contour plots indicate a relatively uniform stress state around each fiber, as would be expected. The tendency to indicate a nonuniform yield pattern as in Figure 22a is, as noted in Section 5.3.1 also, an artifact of the nonuniform finite element grid used here (see Figure 17a).

At an applied stress of 12 ksi (Figure 22b) the extent of yielding has spread somewhat. At 15.29 ksi (Figure 22c) the first microcracking is predicted, at the interface of one fiber. This cracking continued to extend around this fiber with increasing applied stress, up to 24.14 ksi (Figure 22d), at which point the crack suddenly extended completely across the composite (from top to bottom of the model), defining total failure (the ultimate transverse tensile strength of the composite).

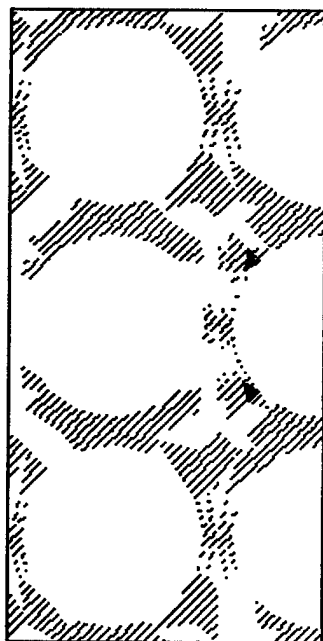
Figure 23 indicates a similar sequence of plots for the composite containing 2.9 percent porosity. At an applied transverse tensile stress of 6 ksi (Figure 23a) the extent of yielding is comparable to that of the nonporous composite (see Figure 22a), except that the



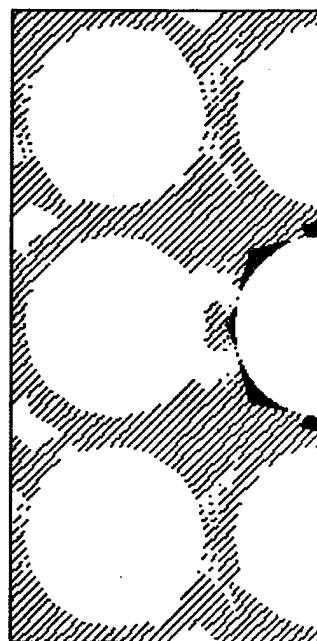
a)  $\bar{\sigma}_x = 6.00$  ksi



b)  $\bar{\sigma}_x = 12.00$  ksi

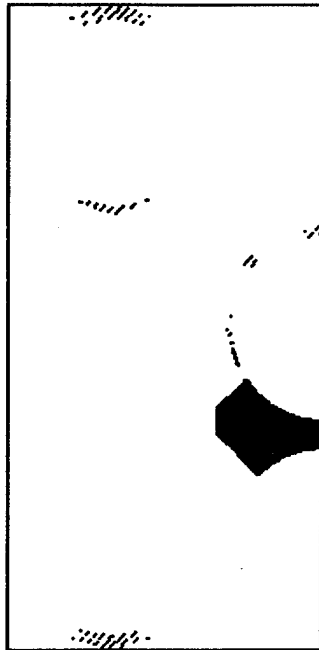


c)  $\bar{\sigma}_x = 15.29$  ksi



d)  $\bar{\sigma}_x = 24.14$  ksi

Figure 22. Transverse Tension, No Porosity; Extent of Yielding and Crack Propagation With Increasing Applied Stress (Elastic Elements are White, Plastic Elements are Shaded, Failed Elements are Black).



a)  $\bar{\sigma}_x = 6.00$  ksi



b)  $\bar{\sigma}_x = 12.00$  ksi



c)  $\bar{\sigma}_x = 15.02$  ksi



d)  $\bar{\sigma}_x = 21.99$  ksi

Figure 23. Transverse Tension, 2.9 Percent Porosity; Extent of Yielding and Crack Propagation With Increasing Applied Stress (Elastic Elements are White, Plastic Elements are Shaded, Failed Elements are Black).

presence of the pore has relieved the stress slightly at the top side of the diagonally adjacent fiber, as indicated in Figure 23a.

At 12 ksi (Figure 23b) the extent of yielding is about the same as for the nonporous composite, although a local failure is predicted at the fiber-matrix interface near the pore, just as for the longitudinal tensile loading (Figure 21). This local microcracking spreads around the interface with increasing applied stress (Figure 23c), eventually resulting in the crack pattern of Figure 23d just prior to total failure.

To summarize, the nonporous composite is predicted to fail at an applied transverse tensile stress of 24.14 ksi, while the porous composite fails at 21.99 ksi (remembering that an unrealistically high matrix tensile strength of 28.69 ksi was assumed here, based upon torsion test data). Nevertheless, the analysis predicts a 9 percent transverse tensile strength loss due to the 2.9 percent porosity modeled here (as a single pore between two fibers). Undoubtedly, other modeling of this 2.9 percent porosity would lead to different results; a statistical modeling of possible porosity geometries should be performed in future studies.

How the predicted transverse tensile stress-strain response of the composite is influenced by the 2.9 percent porosity is indicated in Figure 24. As expected, the composite stiffness as well as strength is reduced slightly. Both curves also reflect the influence of the nonlinear matrix material response on the composite response (although it is slight).

### 5.3.3 Longitudinal Shear

A longitudinal shear loading  $\bar{\tau}_{xz}$  was applied to the composite. That is, the shear loading was assumed to be acting in a direction parallel to the fiber axes, distributed along the vertical edges of the models of Figure 17. This simulates the in-plane shear stress induced in a lamina of a composite laminate.

Figure 25 indicates the extent of yielding and crack propagation in a nonporous composite. As indicated in Figure 25a, even at an applied stress  $\bar{\tau}_{xz}$  of only 1.49 ksi, considerable yielding has occurred around each fiber near the fiber-matrix interface. This is primarily due to the presence of cure-induced residual thermal stresses. It will be

## TRANSVERSE TENSION

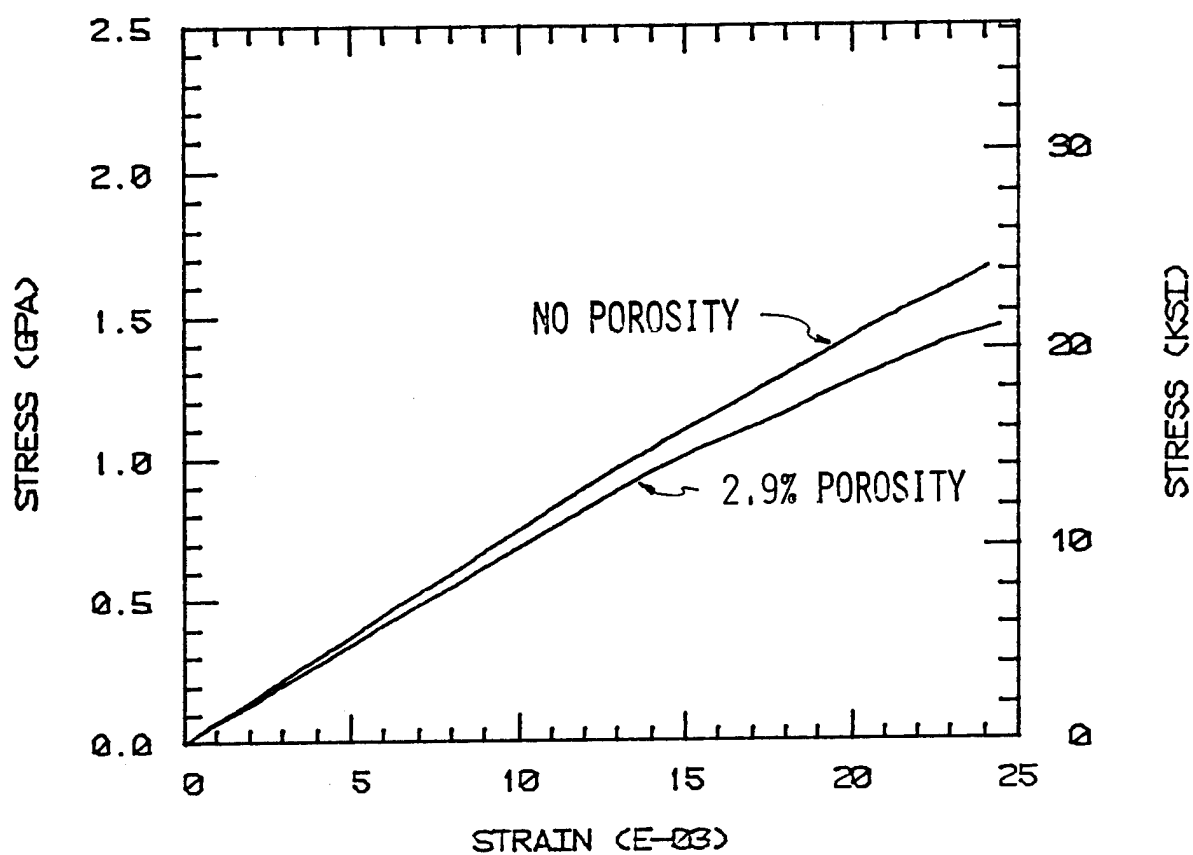
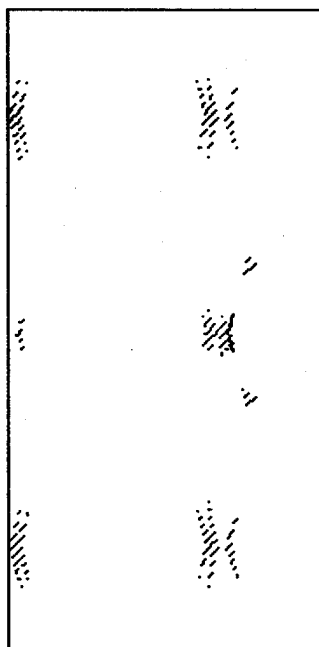


Figure 24. Transverse Tension; Predicted Stress-Strain Response With and Without Porosity.





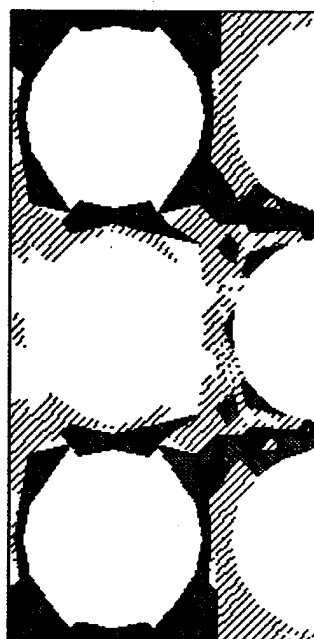
a)  $\bar{\tau}_{xz} = 1.49$  ksi



b)  $\bar{\tau}_{xz} = 4.48$  ksi



c)  $\bar{\tau}_{xz} = 7.18$  ksi



d)  $\bar{\tau}_{xz} = 8.64$  ksi

Figure 25. Longitudinal Shear, No Porosity; Extent of Yielding and Crack Propagation With Increasing Applied Stress (Elastic Elements are White, Plastic Elements are Shaded, Failed Elements are Black).

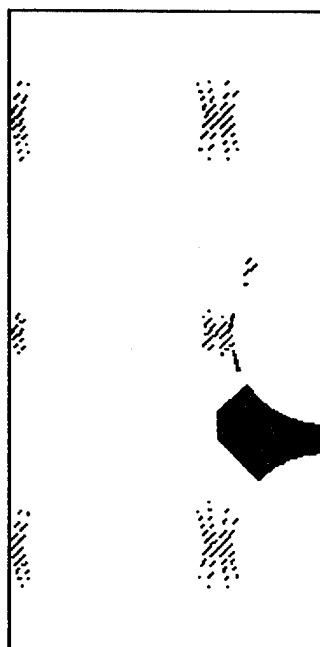
noted in Figure 25a that a small crack has also formed at the interface of one fiber. As discussed in Section 4, the matrix strength properties used here are based upon solid rod torsion test data. At the room temperature, dry condition, the shear yield strength is 5.51 ksi; the shear ultimate strength is 16.57 ksi. These values were used to establish the octahedral shear yield and ultimate strength (failure) criteria.

Figure 25b indicates the extent of yielding and crack propagation at an applied shear stress of 4.46 ksi. At 7.18 ksi (Figure 25c), extensive yielding and microcracking has occurred. Total failure of the composite is predicted at 8.64 ksi, developing from the crack pattern indicated in Figure 25d. At total failure, a crack path must run completely through the model; for the  $\bar{\tau}_{xz}$  loading, this path is from top to bottom.

The influence of microporosity on longitudinal shear loading response is indicated in Figure 26. As for the nonporous composite, the residual thermal stresses are high enough so that even at the low applied stress (1.31 ksi) of Figure 26a, considerable yielding and a slight microcrack is present. The yielding and cracking grows with increasing applied stress in a manner similar to that for the nonporous composite (Figures 26b and c versus Figures 25b and c). Total failure occurs at an applied shear stress  $\bar{\tau}_{xz}$  of 8.74 ksi, the crack pattern just prior to failure being indicated in Figure 26d.

To summarize, the presence of porosity does not appear to influence the composite shear response as much as it influences transverse tensile response. The predicted ultimate shear strengths are almost identical for the nonporous and porous composites.

The predicted shear stress-shear strain response is indicated in Figure 27. The presence of porosity does decrease the shear stiffness of the composite, as expected since matrix material has been removed. Much more nonlinearity than for transverse tensile loading is exhibited for both the nonporous and the porous composite (Figure 27 versus Figure 24), both because of the difference in dominate local stress state (shear versus normal stress), and the much more extensive cracking occurring at lower stress levels for the shear loading cases. (This cracking reduces the effective stiffness of the composite, resulting in



a)  $\bar{\tau}_{xz} = 1.31 \text{ ksi}$



b)  $\bar{\tau}_{xz} = 4.13 \text{ ksi}$



c)  $\bar{\tau}_{xz} = 6.86 \text{ ksi}$



d)  $\bar{\tau}_{xz} = 8.74 \text{ ksi}$

Figure 26. Longitudinal Shear, 2.9 Percent Porosity; Extent of Yielding and Crack Propagation With Increasing Applied Stress (Elastic Elements are White, Plastic Elements are Shaded, Failed Elements are Black).

## LONGITUDINAL SHEAR

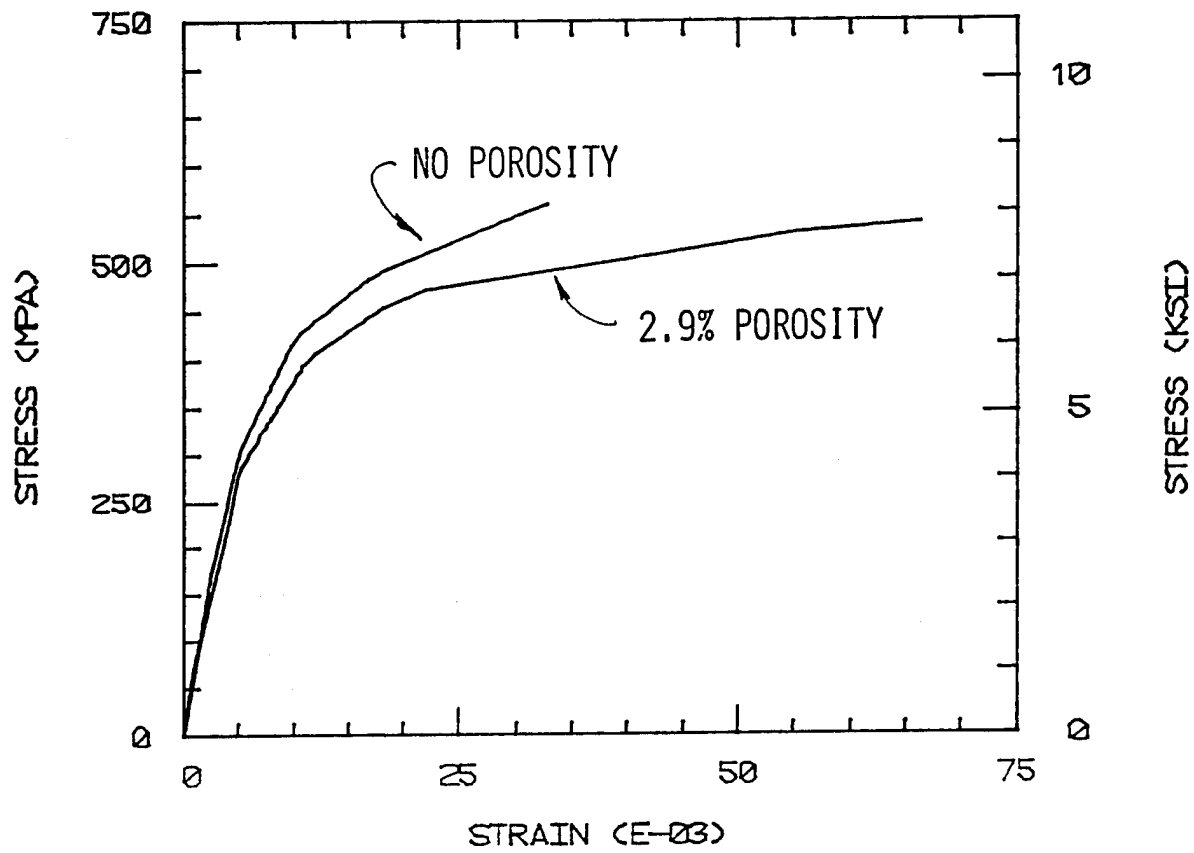


Figure 27. Longitudinal Shear; Predicted Stress-Strain Response With and Without Porosity.

greater composite strains for a given applied stress.) That is, much of the nonlinearity exhibited by both curves of Figure 27 is not due to matrix material nonlinear response, but rather to breakdown (cracking) of the composite structure.

#### 5.4 Discussion

The results presented here are intended to demonstrate the capabilities of the current finite element micromechanics analysis. Actual constituent material properties were used as input, and a representative microporosity model was analyzed. Nevertheless, it is recognized that additional work needs to be done before a totally representative predictive capability is available. The principal problems remaining are associated with the multiaxial stress state flow rule to be used, and the establishment of an adequate failure criterion.

As discussed in Section 4, experimental data for the epoxy matrix suggest response not governed by conventional flow rules and failure criteria. Thus, additional very basic work needs to be conducted in these areas before a full understanding of composite material response can be gained. Nevertheless, the present analysis provides considerable useful information. For example, the prediction of stiffness properties presents no difficulty. Moduli, Poisson's ratios, coefficients of thermal and moisture expansion, and any other bulk properties can be accurately predicted. Likewise, material stress-strain nonlinearities can be handled well. It is strength predictions which still present difficulties.

Having carried micromechanics analyses forward to this point, the present authors are confident that this final hurdle can be overcome in future efforts.

## SECTION 6

### LAMINATE WITH PLY DROP-OFFS

A 3-D finite element analysis of the 30-ply, F-18 laminate containing ply drop-offs was first attempted during the prior one-year study [3]. The analytical results tended to predict what had been observed experimentally, viz, that ply drop-offs do not significantly reduce the strength of the composite laminate. However, these analytical predictions did not incorporate thermal residual stresses due to cooldown, nor inelastic material response. Both of these capabilities were available, but were not exercised, as discussed in Reference [3]. Both have been incorporated in the present work.

#### 6.1 Analysis Capabilities

The 3-D finite element analysis developed at the University of Wyoming to model composite laminates was briefly described in Reference [3]. More details are given in Reference [9]. Thus, a detailed description need not be repeated here. A principal feature of the 3-D analysis and related computer program is the ability to model nonlinear orthotropic material behavior. This is a somewhat unique capability among existing finite element analyses, either 2-D or 3-D. A complete representation of ply material property changes as a function of both temperature and moisture is available. How these temperature and moisture properties are modeled is discussed in detail in Section 4. This modeling has been improved considerably during the past year.

Improved computer graphics have also become available during the past year, making it much easier to prepare grid models, and to display results.

#### 6.2 Finite Element Model

Only the  $0^\circ$  ply drop-off geometry has been modeled here, i.e., the  $\pm 45^\circ$  ply drop-offs included in the prior study have not been modeled again. This is consistent with the current experimental work [4], in which only  $0^\circ$  ply drop-off laminates were fabricated and tested.

The finite element grid indicated in Figure 28 was constructed. It consists of 273 eight-node isoparametric elements, i.e., three layers each containing 91 elements of constant y-direction thickness. These are the same types of elements used in the prior work, and the grid shown in Figure 28 is of about the same general refinement as those used previously [3]. However, less emphasis has been placed upon refinement at the drop-off, to gain a better overall definition. As indicated in Figure 28, only one half of the 30-ply laminate has been modeled, invoking midplane symmetry, just as before. Here, the ply at the midplane is modeled as a  $+45^\circ$  ply. The experimental laminate in the present [4] and all prior studies [1-3] was not actually quite symmetric, the two plies adjacent to the midplane being  $-45^\circ$  and  $+45^\circ$  rather than either both  $-45^\circ$  or  $+45^\circ$ . As previously discussed [3], this is a minor deviation from symmetry, however, and thus has been once again ignored here. The one  $0^\circ$  ply dropped off in the one half of the laminate was modeled by two layers of elements, as indicated in Figure 28. The resin pocket at the end of this ply was modeled using a single element in the plane, i.e., by three elements through the thickness of the model. This resin pocket is relatively large (long). The influence of resin pocket size was analyzed in the prior study [3]. Photomicrographs of resin pockets in actual composites were also presented in the report of that work. The other 14 plies shown in Figure 28 were each modeled by a single layer of elements, as shown.

Although the model used here is three layers of elements thick, just as in the prior study [3], the assumed boundary conditions were slightly different. Here, both lateral boundaries, i.e.,  $y = \text{constant}$ , were assumed to remain plane. This approximates the conditions for a strip well removed from the free edges of the actual composite laminate. This was done since it was felt that the present grid refinement was not sufficient to adequately model free edge stress effects. The lateral boundary conditions modeled in Reference [3] did attempt to represent an actual free edge, although admittedly not very accurately. These results can be studied if an indication of the influence of a free edge is desired. In future work it will hopefully be possible to run much more refined finite element grids, in which case more reliable results will be obtained. The results to be presented here assume the laminate

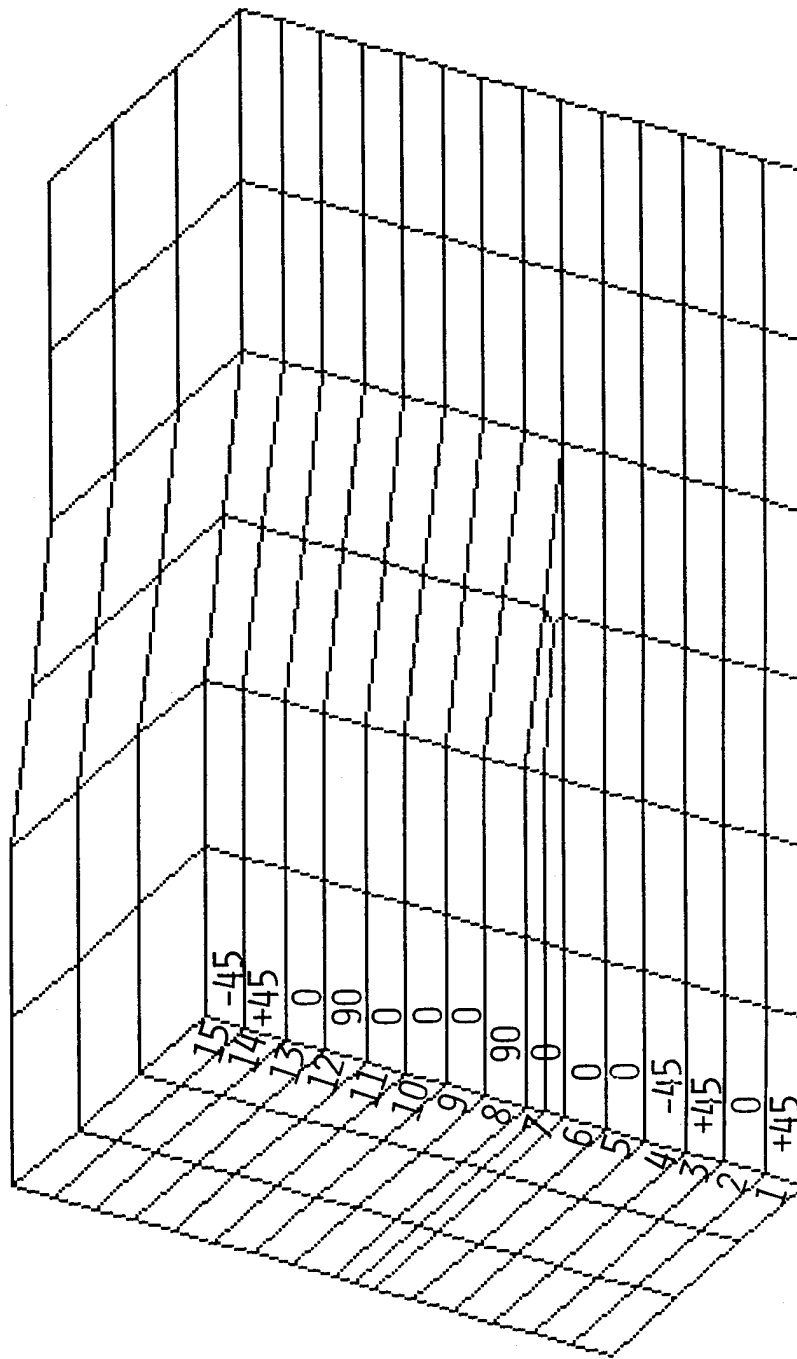


Figure 28. Three-Dimensional Finite Element Model of 0° Ply Drop-Off in F-18 Laminate.



to be infinitely wide, i.e., no free edge effects exist.

The ends of the model, i.e.,  $x = \text{constant}$ , were also assumed to remain plane, as in the prior study. The axial compressive loading was achieved by imposing a uniform displacement in the  $x$ -direction of one boundary relative to the other. The right surface of the model (representing the midplane of symmetry) was assumed to remain plane also, as previously.

The individual plies have been modeled as being 0.006" thick. The model is 1.5" long (in the  $x$ -direction) and 1.0" wide (in the  $y$ -direction).

### 6.3 Predicted In-Plane Stresses

Both as-fabricated and moisture-preconditioned specimens containing ply drop-offs were modeled. Thus, it was necessary to first apply a thermal loading representing the cooldown from the 177°C cure temperature to room temperature. Then the composite was either loaded in axial compression, or subjected to a one weight percent moisture absorption prior to mechanical loading. Predicted stress contours in selected plies will be presented, after cooldown, after moisture preconditioning, and after mechanical loading is applied.

#### 6.3.1 Cooldown Thermal Residual Stresses

Thermal residual stresses induced during cooldown from the cure temperature to room temperature were not included in the prior study [3], although the capability existed. The 3-D finite element model of Figure 28 was subjected to a temperature change from an assumed stress-free temperature of 177°C (350°F), i.e., the composite cure temperature, to room temperature (21°C). This 156°C temperature decrease was applied in 17 increments.

Any or all of the six components of stress can be plotted for each ply, using either geometric ( $x, y, z$ ) coordinates or material (1, 2, 3) coordinates, at each temperature increment. Likewise, the corresponding six components of strain, or any other quantity which can be calculated, e.g., effective stress or strain, can be plotted. For the present purposes, only selected plots will be included. Hundreds of additional plots were studied, however.

As indicated in Table 6.4 of Reference [1] and elsewhere, the ultimate strengths of a unidirectional ply of Hercules AS/3501-6

graphite/epoxy are reasonably well characterized. Values from Reference [1] are summarized here in Table 5.

TABLE 5. HERCULES AS/3501-6 GRAPHITE/EPOXY UNIDIRECTIONAL PLY STRENGTH PROPERTIES [1].

| Ultimate Strength (ksi) |             | 21°C, Dry | 21°C, 1%M |
|-------------------------|-------------|-----------|-----------|
| $\sigma_{11}^u$         | tension     | 235       | 235       |
|                         | compression | -175      | -163      |
| $\sigma_{22}^u$         | tension     | 7.0       | 6.0       |
|                         | compression | -37.0     | -29.0     |
| $\tau_{12}^u$           | shear       | 18.1      | 16.0      |

Thus, only in-plane stresses in the material coordinates, i.e.,  $\sigma_{11}$ ,  $\sigma_{22}$ , and  $\tau_{12}$  and not in-plane stresses in the geometric coordinates, i.e.,  $\sigma_{xx}$ ,  $\sigma_{yy}$ , and  $\tau_{xy}$ , will be referred to here, for brevity. These stress components can be readily related to the ply stress ultimates given in Table 5. Also, results will be presented here only for Increment 17, i.e., the stress state after cooldown to room temperature.

The interlaminar stress components, i.e.,  $\sigma_{33}$ ,  $\tau_{13}$ , and  $\tau_{23}$ , may also be of interest for the present ply drop-off model, since the discontinuity can induce such stresses even when a free edge is not modeled. First, however, the in-plane stresses will be presented.

Unlike for the model of a laminate with a hole to be presented in the next section, Section 7, where the two groups of three 0° plies are each modeled by a single layer of finite elements, the present ply drop-off model represents each 0° ply individually. This permits a better description of the stress gradients through the laminate thickness due to the centrally located dropped-off ply. Also of course, as shown in Figure 28, only one 0° ply is dropped off, i.e., Ply 7.

For all of the loading cases to be discussed in this section, including the present case of cooldown residual stresses only, complete stress contours were available for every ply. However, for brevity of

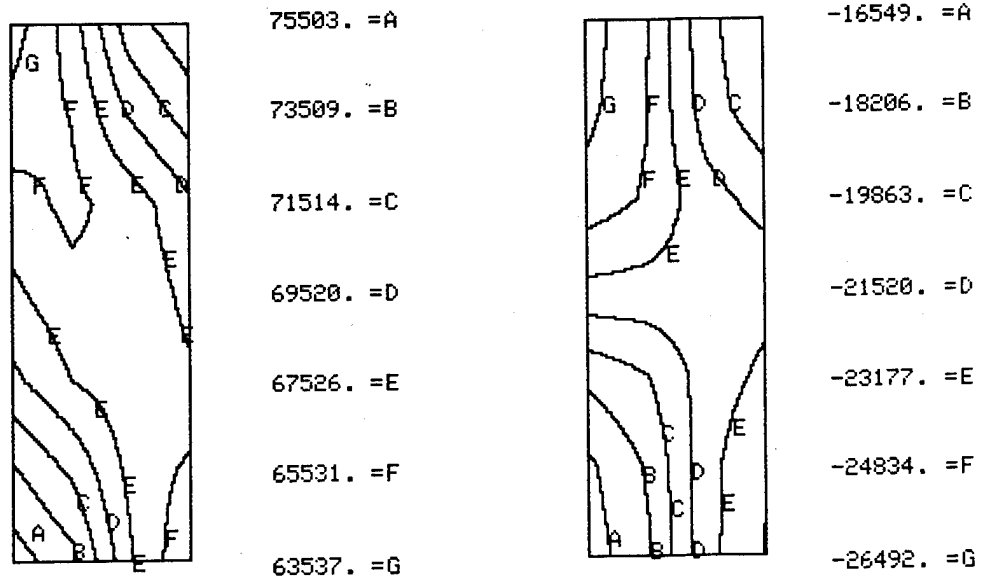
presentation, only plots for selected plies will be shown. The discussion of observations is based upon knowledge of the complete stress fields in every ply, however.

As might be expected, it was found that the drop-off ply (Ply 7) and the adjacent plies were most strongly influenced by the drop-off. Thus, one ply of each orientation closest to the dropped-off 0° ply has been selected for presenting stress distributions. That is, Ply 4 (the nearest -45° ply; stresses in the +45° plies were similar in magnitude to those in -45° plies), Ply 6 (the 0° ply adjacent to the drop-off ply), and Ply 8 (the 90° ply adjacent on the other side of the drop-off ply), along with the drop-off ply, Ply 7, will be shown.

Figure 29 presents plots of the longitudinal stress  $\sigma_{11}$  (the stress component in the direction of the fibers) for Plies 4, 6, 7 and 8 (i.e. -45°, 0°, 0° drop-off, and 90° plies). The stresses in the 0° and 90° plies are compressive, while those in the 45° plies are tensile. The -26.5 ksi maximum stress in Ply 6 (Figure 29b), and the range and distribution of this  $\sigma_{11}$  stress in general, was representative of that in each of the other 0° plies, with the minor exception of Ply 2. The highest and lowest  $\sigma_{11}$  stresses in Ply 2 were -28.4 ksi and -13.8 ksi, respectively. That is, this highest stress, although occurring in the same region within the ply, was about 7 percent higher than that in Ply 6.

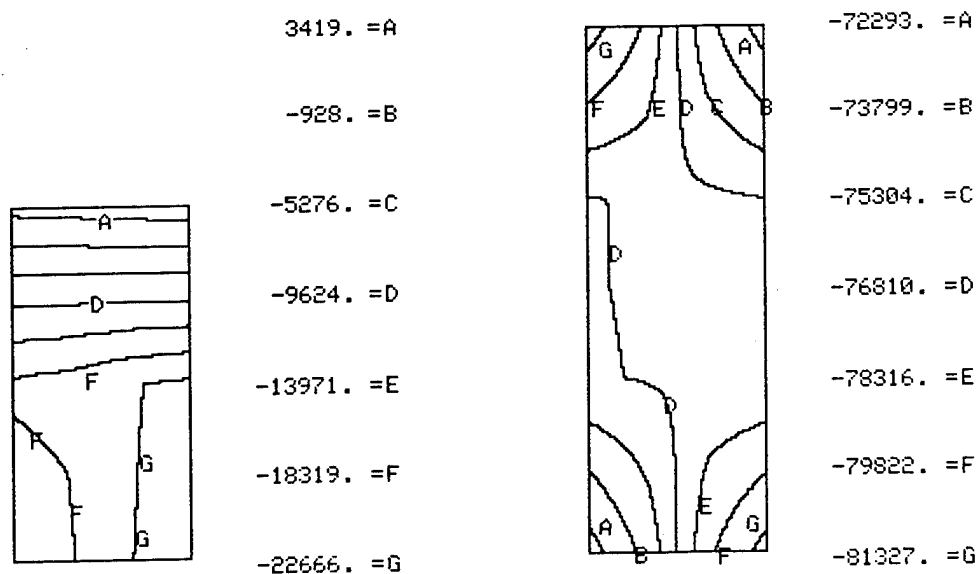
The  $\sigma_{11}$  stresses in the two 90° plies were much higher than those in the 0° plies, and essentially identical to each other. The  $\sigma_{11}$  stresses in 90° Ply 8 are plotted in Figure 29d. The maximum stress of -81.3 ksi is about 46 percent of ultimate (as given in Table 5).

The highest  $\sigma_{11}$  stresses in the +45° and -45° plies did occur in the -45° ply (Ply 4) shown in Figure 29a. These stresses were all tensile, whereas the  $\sigma_{11}$  stresses in the 0° and 90° plies were all compressive. In Ply 4, the lowest tensile stress (63.5 ksi) was 84 percent of the highest tensile stress (75.5 ksi). As expected, the variation of stress became less for the +45° and -45° plies further from the dropped-off ply toward the outer surface. That is, there was less influence of the ply drop-off. (The highest  $\sigma_{11}$  stress in Ply 15 was 66.8 ksi.) On the other hand, the variation in stress in Ply 1 (the



a) Ply 4 (-45°)

b) Ply 6 (0°)



c) 0° Ply Drop-Off

d) Ply 8 (90°)

Figure 29. Longitudinal Stress ( $\sigma_{11}$ , psi) in Selected Plies after Cooldown from Cure Temperature.

+45° ply at the laminate midplane) was greater, the high being 61.6 ksi and the low being 45.4 ksi, i.e., the low was only 74 percent of the high. However, this high was almost 20 percent less than the highest stress in Ply 4 (the 45° ply closest to the drop-off). The general distribution of stresses was about the same in all 45° plies, Figure 29a thus being representative.

The stress in the neat resin pocket at the end of the dropped-off 0° ply (see Figure 29c) is compressive near the end of the ply, but becomes tensile toward the tip of the resin pocket. The values indicated in Figure 29c range from approximately -8.0 ksi to 3.5 ksi. These values are less than measured neat epoxy resin matrix strengths (see Section 4). As can be seen in Figure 29c, the  $\sigma_{11}$  stress in the dropped-off ply quickly builds up to values equal to those in the adjacent continuous 0° ply (compare Figure 29c to Figure 29b) over a relatively short distance from the end of the ply.

Representative plots of the  $\sigma_{22}$  component of stress (the normal stress transverse to the fibers) are shown in Figure 30, for the same Plies 4, 6, 7 and 8 shown in Figure 29. The  $\sigma_{22}$  stresses in all the 0° and 90° plies were tensile, as well represented in Figures 30b, c and d. The general distributions are also well represented by Figures 30b and d. The highest  $\sigma_{22}$  stress did occur in the 90° Ply 8 (Figure 30d), but at 3.9 ksi it was well below the tensile ultimate strength of 7.0 ksi (see Table 5).

The  $\sigma_{22}$  stresses in all of the 45° plies were compressive, the highest occurring in the Ply 4 shown (Figure 30a). At only -2.2 ksi, this stress is well under the -37.0 ksi compressive ultimate strength indicated in Table 5.

As shown in Figure 30c, the  $\sigma_{22}$  stress in the neat resin pocket (i.e., the normal stress in the width direction of the laminate) was tensile everywhere, the highest value being only 4.3 ksi.

The in-plane shear stresses  $\tau_{12}$  are indicated in Figure 31. These stresses were low in all 0° and 90° plies, typically increasing in each ply away from the drop-off location (as seen in Figures 31b, c and d). The highest value of  $\tau_{12}$  of 0.5 ksi occurred in Ply 2, the 0° ply closest to the laminate midplane. The highest value in Ply 13, the 0° ply farthest from the midplane, was less than 0.2 ksi. The values of

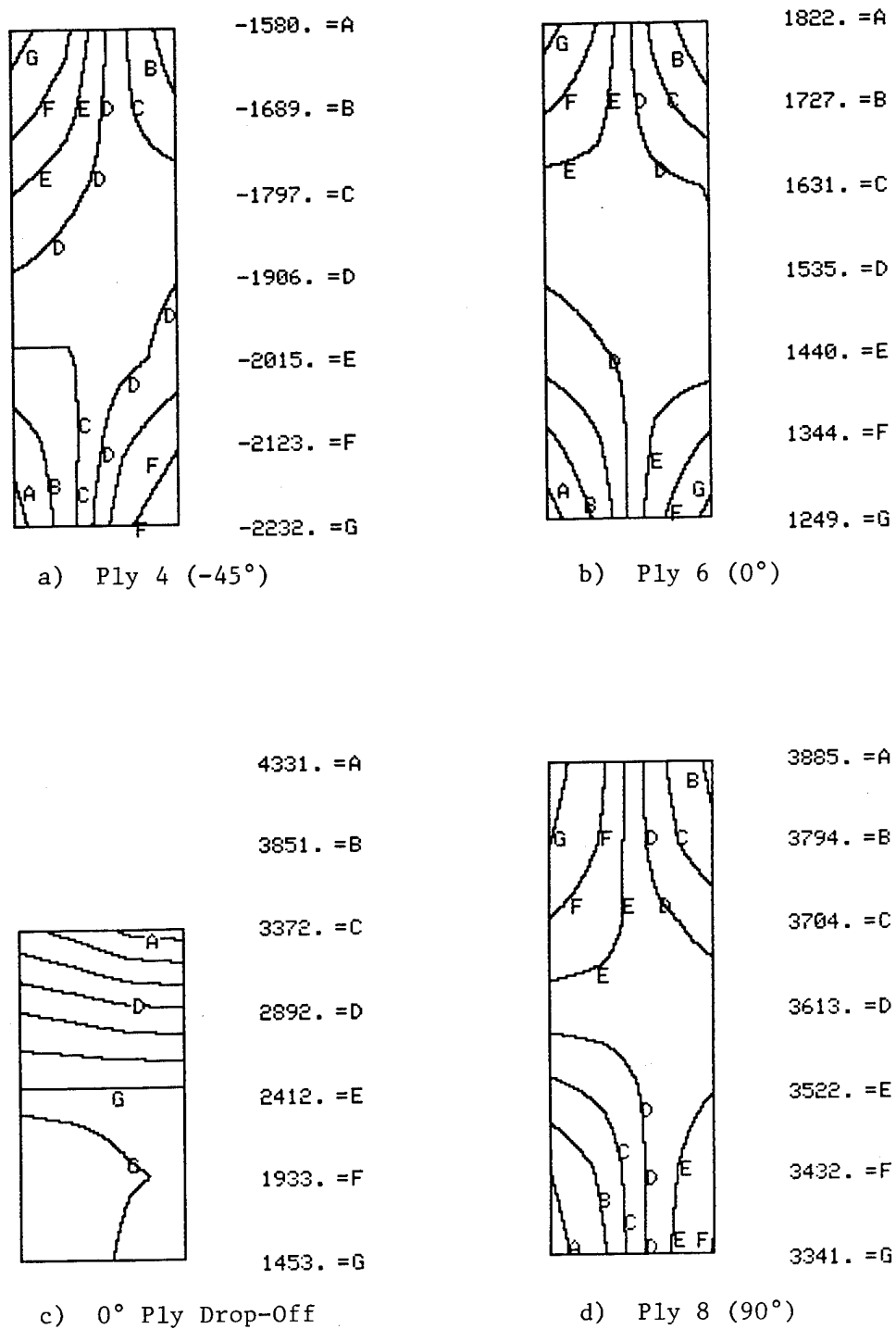
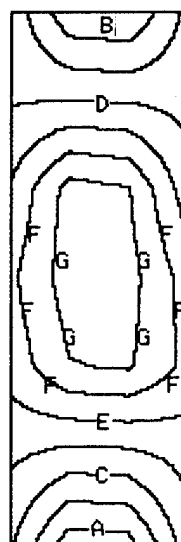


Figure 30. Transverse Stresses ( $\sigma_{22}$ , psi) in Selected Plies after Cooldown from Cure Temperature.



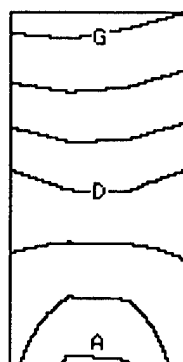
-1209. =A  
-1235. =B  
-1261. =C  
-1287. =D  
-1312. =E  
-1338. =F  
-1364. =G

a) Ply 4 (-45°)



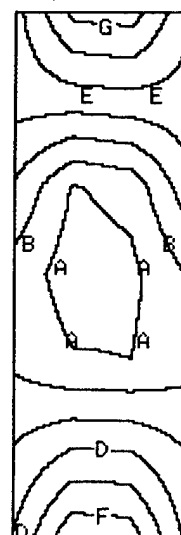
253. =A  
236. =B  
219. =C  
202. =D  
185. =E  
168. =F  
150. =G

b) Ply 6 (0°)



230. =A  
201. =B  
171. =C  
142. =D  
112. =E  
82.4 =F  
52.8 =G

c) 0° Ply Drop-Off



-135. =A  
-150. =B  
-165. =C  
-181. =D  
-196. =E  
-211. =F  
-226. =G

d) Ply 8 (90°)

Figure 31. In-Plane Shear Stresses ( $\tau_{12}$ , psi) in Selected Plies after Cooldown from Cure Temperature.

$\tau_{12}$  in the 45° plies were considerably higher, typically about 1.3 ksi, and very uniform (as indicated in Figure 31a). Since the ultimate shear strength for this composite is 18.1 ksi (see Table 5), even the shear stresses in the 45° plies are not significant.

The shear stress in the neat resin pocket (Figure 31c) was also very low.

In summary, the presence of the 0° ply drop-off did not induce a very large stress riser when the laminate was cooled down from the cure temperature. The longitudinal compressive stresses in the 90° plies and the longitudinal tensile stresses in the 45° plies were the most significant components, but were less than half the ultimate values. The transverse and shear stresses were low. The tensile stresses in the neat resin pocket were also about half the ultimate value for this neat epoxy. These pre-existing thermal residual stresses are obviously not negligible, and whether they are favorable or unfavorable depends upon the type of subsequent loading to be introduced, as will be discussed in the following sections.

#### 6.3.2 Moisture-Induced Stresses

In the experimental portion of this study [4], an axial compressive loading was applied to moisture-conditioned as well as dry specimens, at room temperature. Thus, the predicted influence of moisture absorption on the as-fabricated composite (i.e., a composite already containing thermal residual stresses due to cooldown from the cure temperature) will be presented here.

Experimentally [4], one weight percent moisture (1% M) was absorbed into the laminates. This moisture addition was modeled here in four equal increments, i.e., by Solution Increments 18-21, the first 17 increments being used to model the cooldown, as discussed in the previous subsection. No attempt was made to model a transient moisture gradient through the laminate thickness, although this can readily be done if desired. Only stress contours for Increment 21 (i.e., after 17 increments of temperature decrease, plus 4 increments of moisture absorption) will be presented here.

So that direct comparisons can be made with the predicted stresses for cooldown only, results for the same plies will be presented here. That is, in-plane stress contour plots, in material coordinates, will be

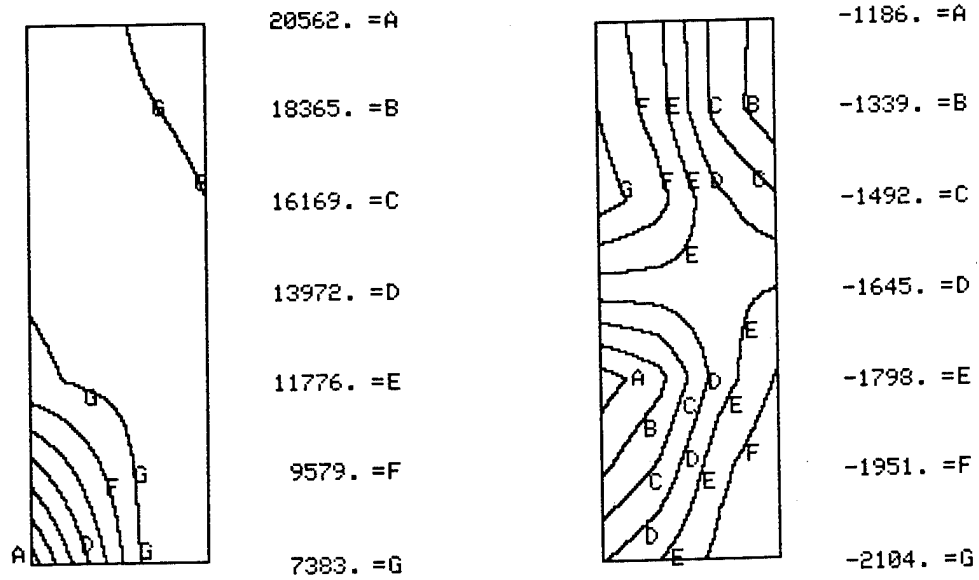


included for Plies 4, 6, 7 and 8. As detailed in Section 6.3.1, and indicated in Figure 28, these are the 45°, 0°, and 90° plies closest to the dropped-off ply, Ply 7. Thus, these plies tend to show the greatest influence of the ply drop-off.

The  $\sigma_{11}$  stresses are presented in Figure 32. By comparing these plots with the corresponding plots for the cooldown residual stresses of Figure 29, it will be noted that the general distributions are similar. However, the addition of one percent moisture significantly reduces the magnitudes of the stresses, as expected. The moisture-induced swelling counteracts the thermal contraction due to cooldown. In fact, the stresses in the 0° and 90° plies are reduced by an order of magnitude, as indicated in Figures 32b, c and d. The highest  $\sigma_{11}$  stresses in the 45° plies (a plot for Ply 4, a -45° ply, is given in Figure 32a) are also reduced, but only by about a factor of 3.5. This lesser reduction is actually favorable in the present case since these stresses are tensile, and the subsequent mechanical loading is to be compressive. If a subsequent axial tensile loading were to be applied, the inverse would be true, the 0° and 90° plies being in a more favorable residual stress condition then.

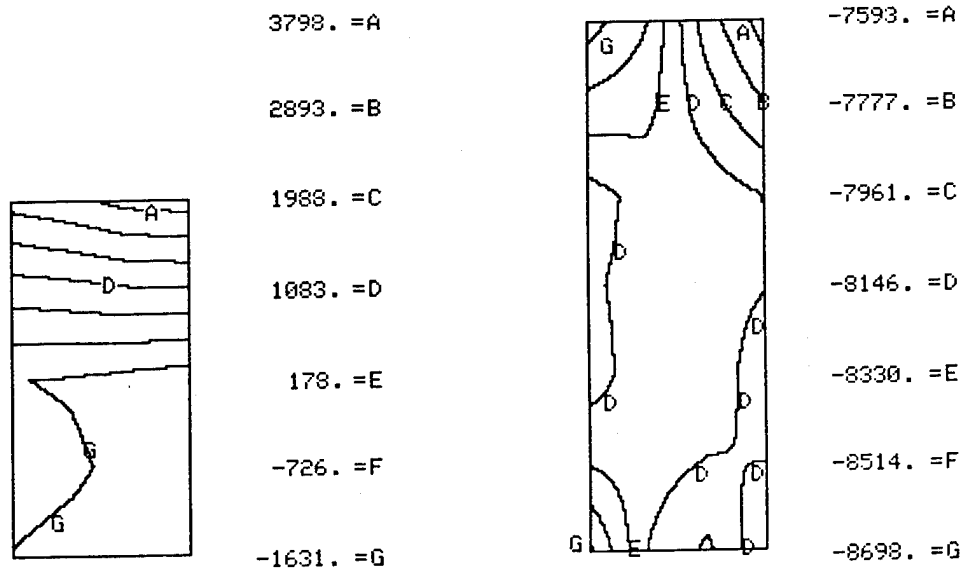
The influence of absorbed moisture on the stresses in the neat resin pocket is also of interest. As indicated in Figure 32c, the  $\sigma_{11}$  stress (the stress in the axial direction of the specimen) is tensile everywhere, with a maximum magnitude of about 3.8 ksi. Prior to moisture absorption, this stress was compressive at the ply end, transitioning to tension at the tip of the resin matrix pocket, this tensile value being 3.4 ksi (Figure 29c). That is, in terms of a subsequent axial compressive loading, moisture addition is favorable in terms of eliminating the high pre-existing compressive stress in the matrix, but it does not induce a correspondingly higher tensile stress in the tip region.

The transverse stresses  $\sigma_{22}$  due to cooldown were slightly more than offset by the addition of one weight percent moisture, as can be seen by comparing Figure 33 to Figure 30. Thus, the residual  $\sigma_{22}$  stress state is very low, except in the neat resin pocket (Figure 33c). Interestingly, but not totally unexpectedly, the pre-existing  $\sigma_{22}$  tensile stress in the resin pocket is not significantly influenced by



a) Ply 4 (-45°)

b) Ply 6 (0°)



c) 0° Ply Drop-Off

d) Ply 8 (90°)

Figure 32. Longitudinal Stresses ( $\sigma_{11}$ , psi) in Selected Plies after 1%M Moisture Absorption.

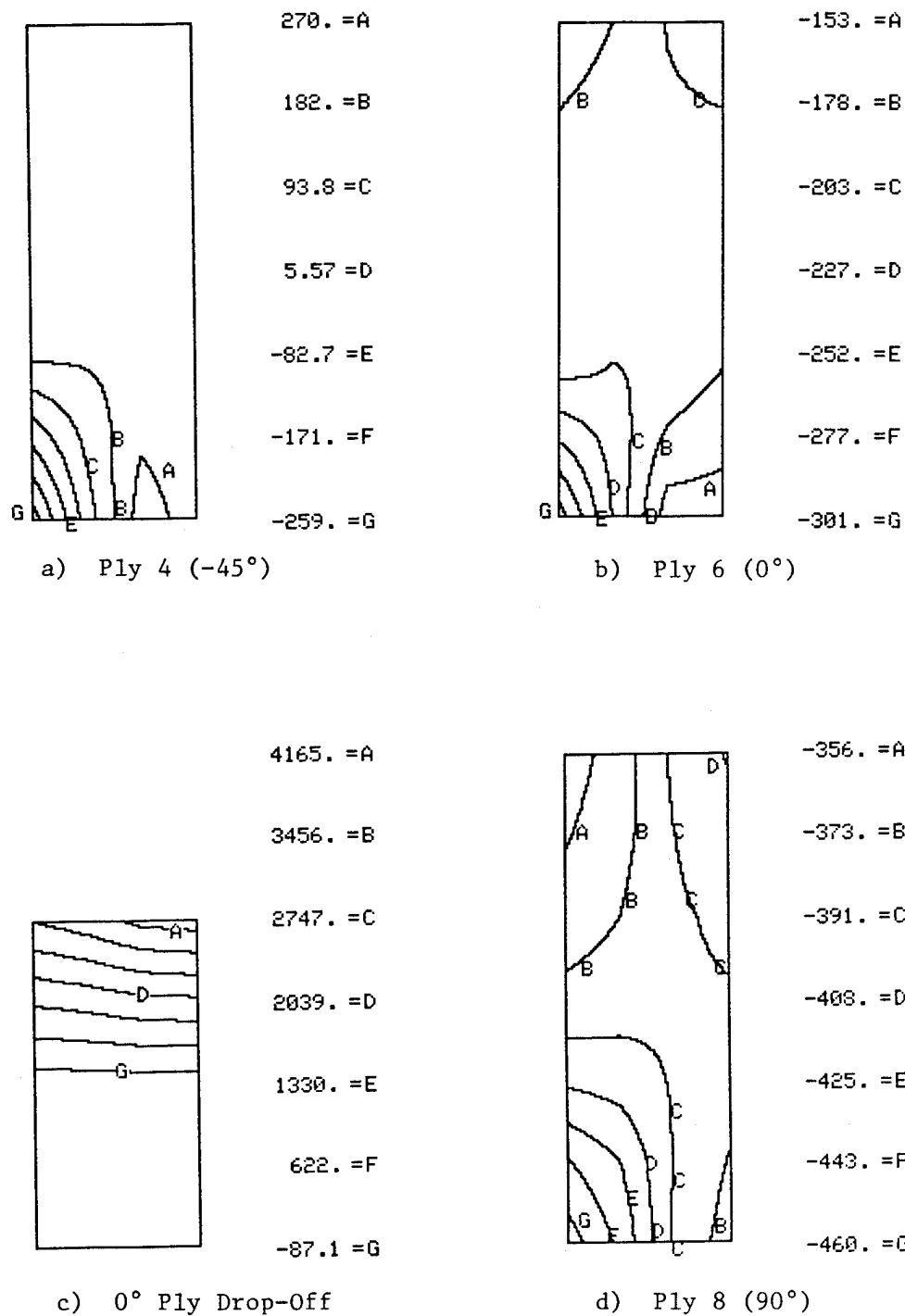


Figure 33. Transverse Stresses ( $\sigma_{22}$ , psi) in Selected Plies after 1% Moisture Absorption.

the moisture addition. The transverse moisture expansion of the 0° dropped-off ply and the adjacent 0° plies are similar in magnitude to that of the matrix, and the expansion of the 90° ply adjacent on the other side of the drop-off is little affected by either temperature or moisture in the transverse direction of the specimen (the  $\alpha_{11}$  and  $\beta_{11}$  of this ply both being very low, as discussed in Section 4). At 4.2 ksi, this matrix tensile stress is not insignificant, the ultimate strength being only 6.0 ksi at the RTW condition, as shown in Table 5. On the other hand, it is not sufficient to induce failure in itself. Whether it is a favorable or unfavorable prestress depends upon the subsequent mechanical loading, as will be discussed.

The in-plane shear stresses  $\tau_{12}$  after moisture absorption are indicated in Figure 34. These stresses are even lower than after cooldown, for which condition they were generally insignificant (as discussed in relation to Figure 31 previously). This includes the resin pocket stresses, which are essentially zero.

In conclusion, the addition of moisture to the as-fabricated composite laminate clearly reduces the in-plane stresses, as expected.

### 6.3.3 Axial Compressive Loading

Axial compressive loading of the F-18 laminate containing two 0° ply drop-offs was analytically modeled for both the RTD and RTW conditions.

#### 6.3.3.1 Room Temperature, Dry Condition

The results to be presented here are for an applied axial compressive stress (based upon the full 30-ply laminate thickness) of -41.6 ksi, corresponding to Solution Increment 25. That is, eight axial compressive loading increments have been applied following the 17 increments of temperature cooldown defined in Section 6.3.1. The experimentally measured proportional limit stress was -35.4 ksi, and the ultimate strength was -98.6 ksi (see Table 5.2 of Reference [2]). Thus, the loading modeled here, -41.6 ksi, is above the experimentally observed proportional limit, and about 42 percent of ultimate. The experimental stress-strain curves indicated relatively little nonlinearity (see, for example, Figures 5.8-5.13 of Reference [2]). Thus, the proportional limit was not well defined. Since composite microcracking and crack propagation were not included in the present

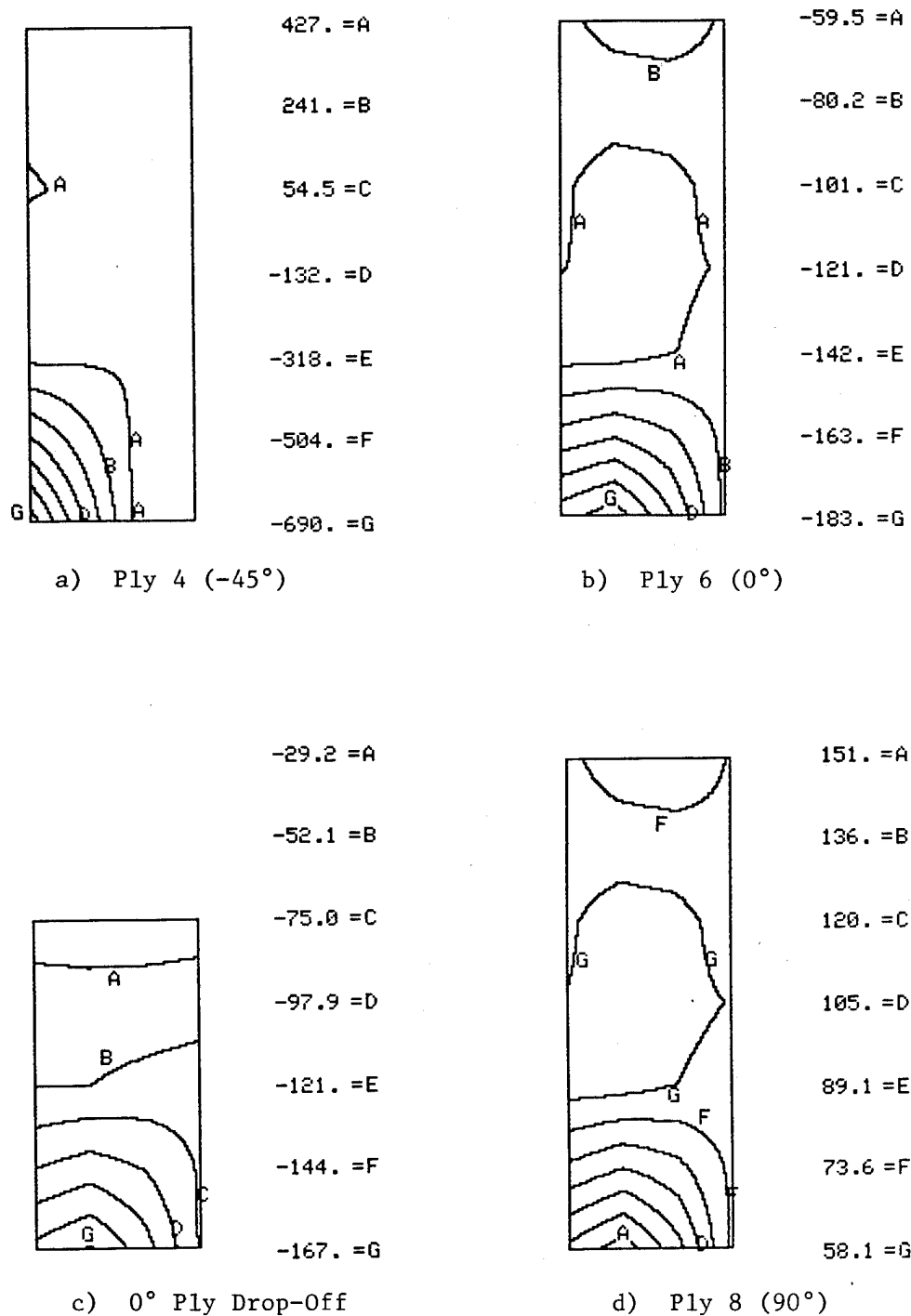


Figure 34. In-Plane Shear Stresses ( $\tau_{12}$ , psi) in Selected Plies after 1% Moisture Absorption.

work, the analytically modeled loading was kept relatively low.

Since in-plane stress plots for Plies 4, 6, 7 and 8 were presented for the cooldown stresses only condition (Section 6.1), the same plies are selected here. Figure 35 contains plots of the  $\sigma_{11}$  stresses at the applied stress of -41.6 ksi. It will be recalled that the  $0^\circ$  plies (including Ply 6, shown in Figure 35b) were in a state of relatively low axial compression due to cooldown, the highest stress of -28.4 ksi occurring in Ply 2, as noted in Section 6.1. After application of the -41.6 ksi axial compression loading, this stress was -101.3 ksi, and still the highest occurring anywhere in the laminate. However, the stresses were relatively uniform in all  $0^\circ$  plies, as expected in this  $0^\circ$  ply-dominated laminate, being less in the lower half of the ply (see, for example, Figure 35b) since the laminate was two  $0^\circ$  plies thicker on this side of the ply drop-offs (two drop-offs occurring through the full laminate thickness).

The  $\sigma_{11}$  stresses in the  $90^\circ$  plies were compressive due to cooldown (see Figure 29d), and are less compressive after mechanical loading, as indicated in Figure 35d. The reduction is about 24 ksi, indicating that the applied axial compression of -41.6 ksi induced a tensile stress of roughly this magnitude in the fiber direction of the  $90^\circ$  plies (neglecting nonlinear material response effects).

The  $\sigma_{11}$  stresses in the  $45^\circ$  plies, initially tensile (see, for example, Figure 29a), were also reduced by the application of the axial compressive loading (Figure 35a). The highest stresses are still in Ply 4, the maximum value being reduced by about 21.4 ksi. That is, the applied compressive loading induces a compression stress in the  $45^\circ$  plies, as expected.

The  $\sigma_{11}$  stresses in the neat resin pocket are compressive, and extremely high (Figure 35c), indicating that this material would fail early during the mechanical loading application. This may account for why intact resin pockets were never observed in the scanning electron microscope studies of Reference [2].

The transverse ( $\sigma_{22}$ ) stresses in the  $0^\circ$  plies are little influenced by the mechanical loading, Ply 6 being totally representative (see Figure 36b). The  $\sigma_{22}$  stresses in the  $90^\circ$  plies (i.e., the stresses in the direction of loading) induced by the mechanical loading are

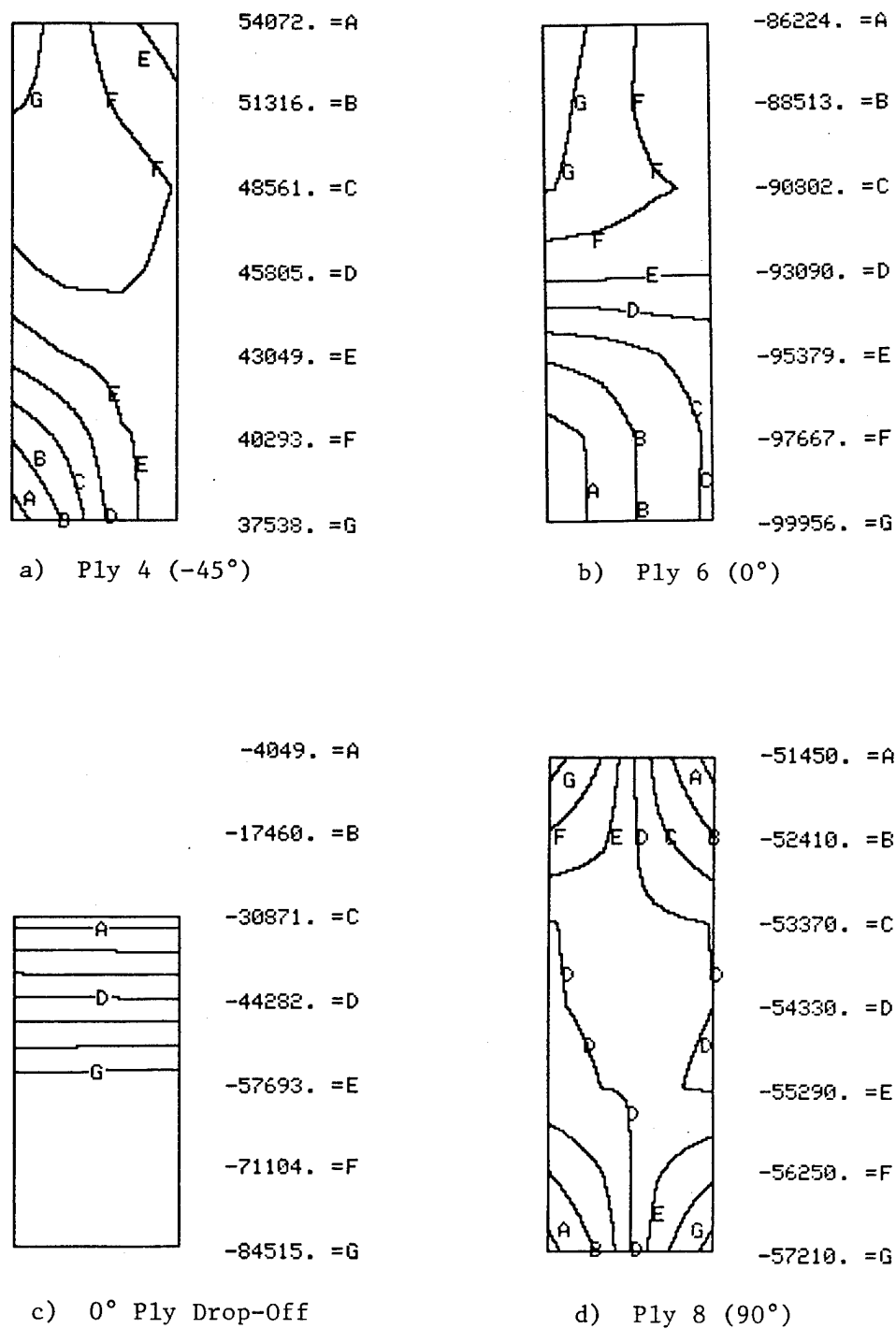


Figure 35. Longitudinal Stresses ( $\sigma_{11}$ , psi) in Selected Plies after -41.6 ksi Axial Compressive Loading; No Moisture.

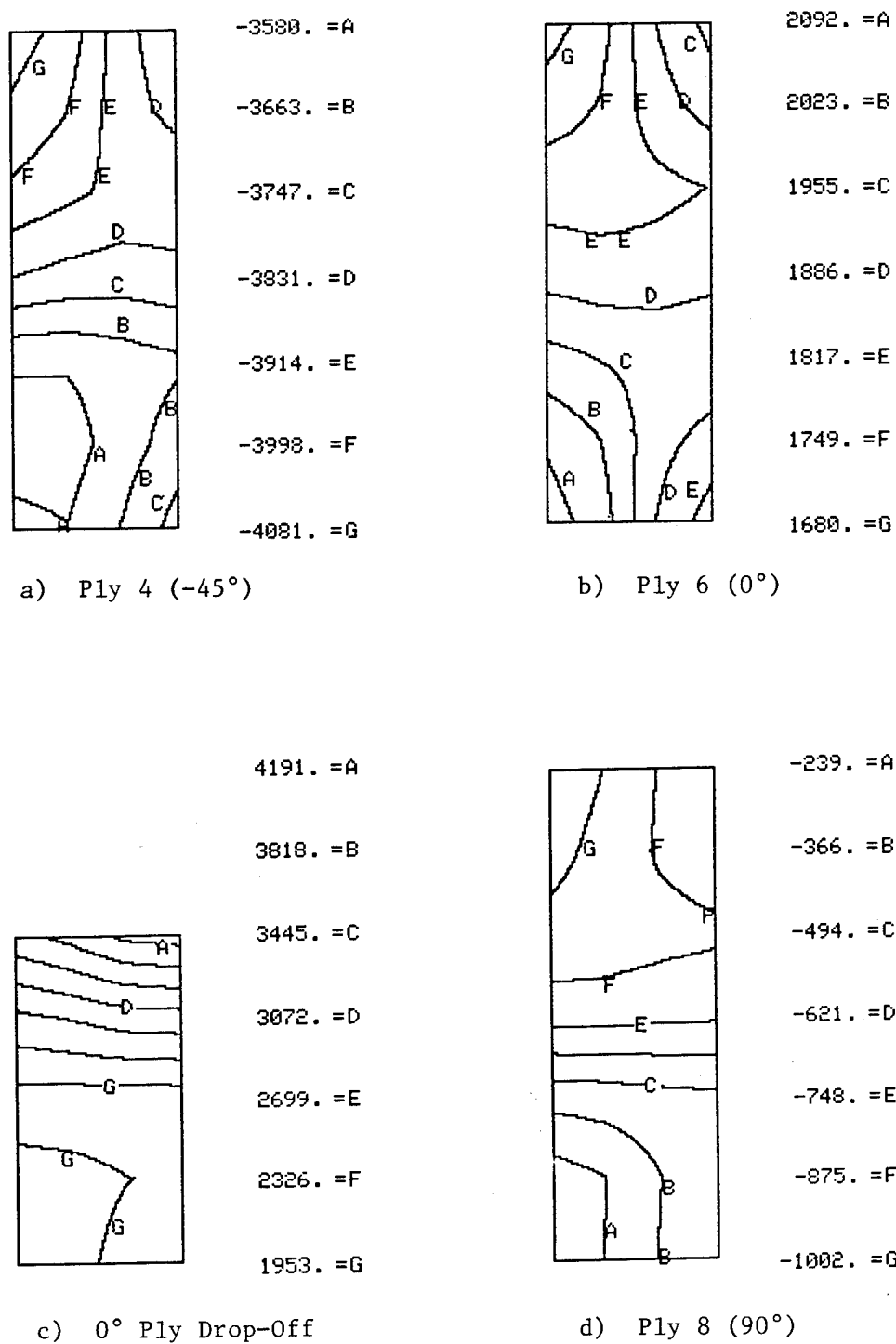


Figure 36. Transverse Stresses ( $\sigma_{22}$ , psi) in Selected Plies after -41.6 ksi Axial Compressive Loading; No Moisture.



compressive, as expected. But since the pre-existing  $\sigma_{22}$  stresses were tensile (Figure 30d), the net stresses after the -41.6 ksi axial loading is applied are only slightly ( $\sim 1$  ksi) negative. This is an excellent example of favorable thermal residual stresses.

The in-plane shear stresses  $\tau_{12}$  in all plies remain low after mechanical loading, those in the  $0^\circ$  and  $90^\circ$  plies being negligible. Because the shear stresses in the  $45^\circ$  plies are reversed in sign by the applied compressive loading (compare Figure 37a with Figure 31a), the net stress remains low. That is, the pre-existing shear stress is favorable. However, the shear stress magnitude would have been low anyway ( $\sim 3.5$  ksi), even in the absence of residual stresses, the ultimate shear strength being 18.1 ksi (Table 5).

#### 6.3.3.2 Room Temperature, Wet Condition

Results are presented for an applied axial compressive stress of -53.4 ksi (based upon the full 30-ply laminate thickness), corresponding to Solution Increment 31. That is, ten axial compressive loading increments have been applied following the 17 increments of temperature cooldown defined in Section 6.3.1 and the four increments of moisture absorption defined in Section 6.3.2. The experimentally measured proportional limit stress was not reported in terms of thick section values in Reference [2], but the thin section value was -35.9 ksi. The thick section ultimate strength was -97.2 ksi. Thus, the loading modeled here, i.e., -53.4 ksi, is undoubtedly above the proportional limit, and about 55 percent of ultimate. The experimentally measured stress-strain curves for this RTW loading (Figures 5.14 and 5.15 of Reference [2]) were only slightly more nonlinear than for the RTD case. The ultimate compressive strength was essentially unaffected by the one weight percent moisture addition.

As in the prior subsections, results will be presented only for Plies 4, 6, 7 and 8, although full results for every ply of the laminate were available for study. Figure 38 contains plots of the  $\sigma_{11}$  stresses in these four plies. As previously discussed, the compressive curing residual stresses in the  $0^\circ$  plies had been significantly reduced by the addition of moisture, to almost zero. This is very favorable in terms of the subsequent compressive mechanical loading. Thus, after the -53.4 ksi applied loading, the highest stresses in the  $0^\circ$  plies is only

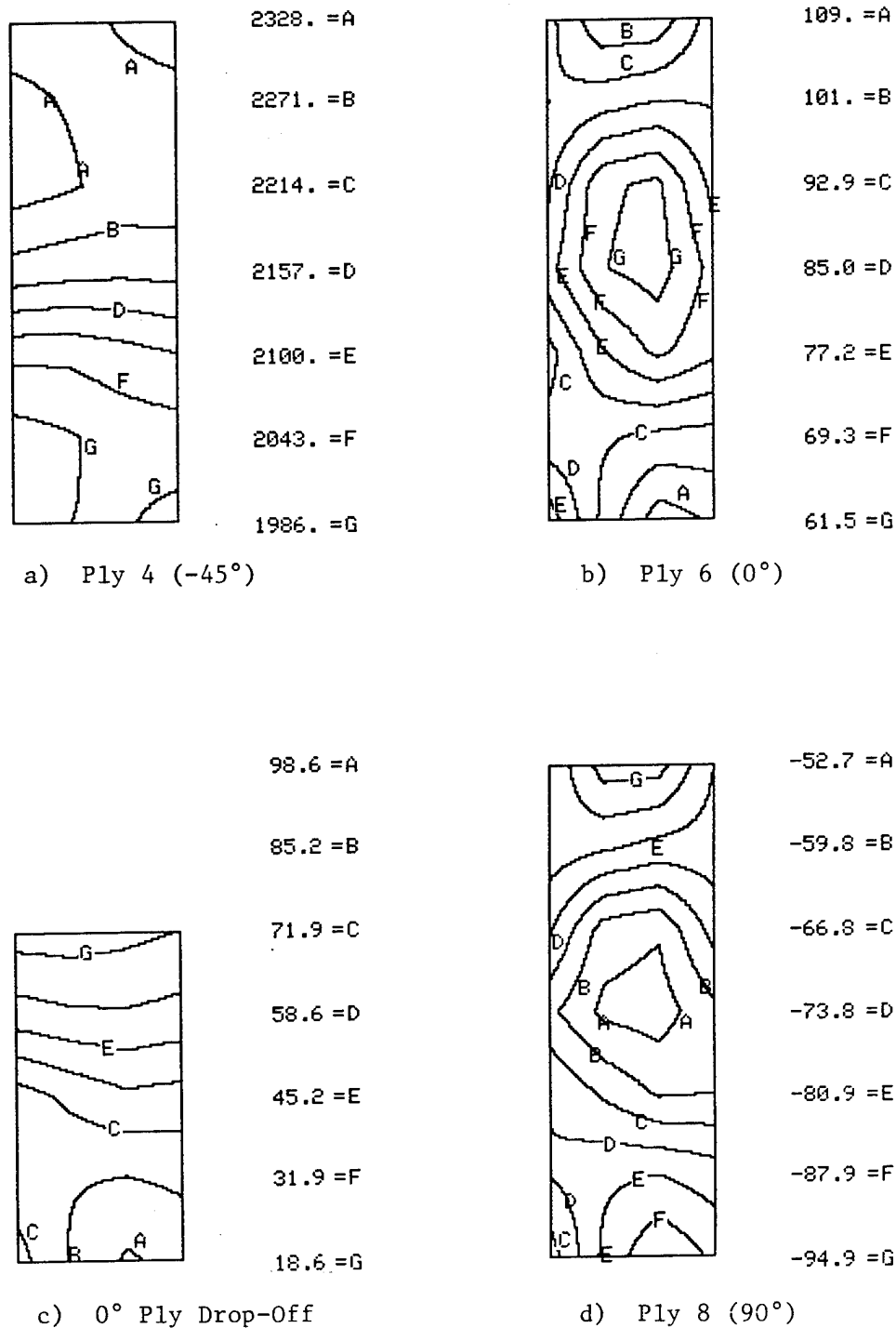
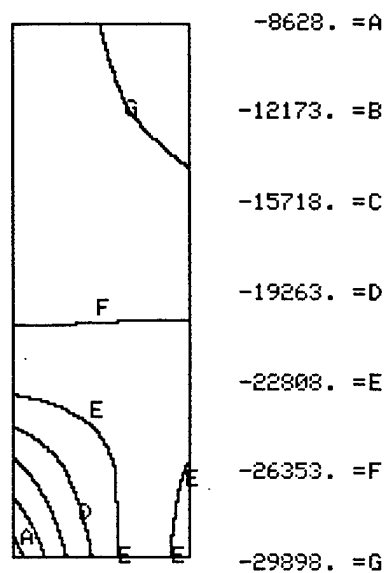
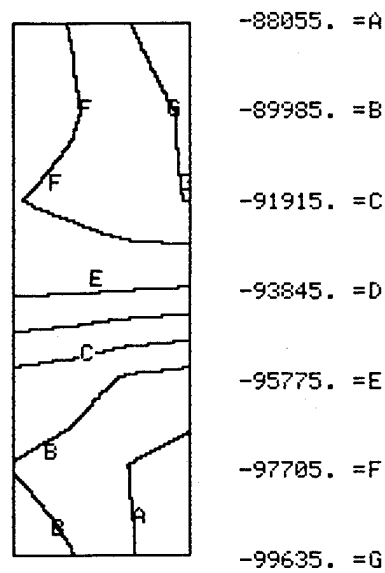


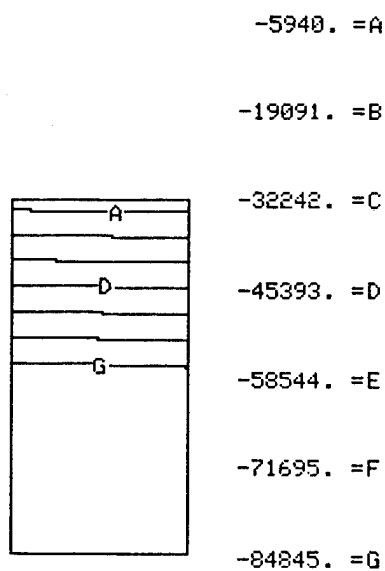
Figure 37. In-Plane Shear Stresses ( $\tau_{12}$ , psi) in Selected Plies after -41.6 ksi Axial Compressive Loading; No Moisture.



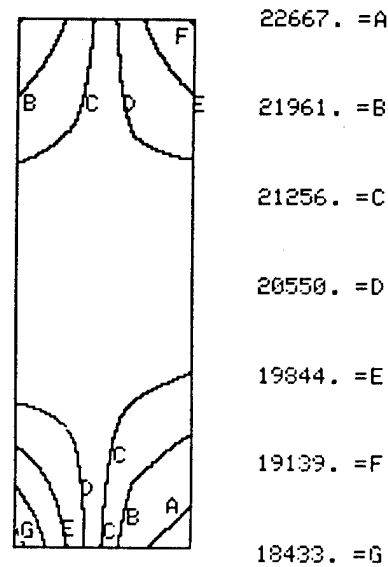
a) Ply 4 ( $-45^\circ$ )



b) Ply 6 ( $0^\circ$ )



c)  $0^\circ$  Ply Drop-off



d) Ply 8 ( $90^\circ$ )

Figure 38. Longitudinal Stresses ( $\sigma_{11}$ , psi) in Selected Plies after  $-53.4$  ksi Axial Compressive loading; 1%M Moisture Absorption.

-99.6 ksi. This is slightly less than the -101.3 ksi maximum stress predicted for the -41.6 ksi loading at RTD conditions. That is, although the applied loading is almost 30 percent higher, the  $0^\circ$  ply stresses are essentially equal. This explains why this  $0^\circ$  ply-dominated laminate is as strong in the wet condition as in the dry condition.

The  $\sigma_{11}$  stresses in the  $90^\circ$  plies were still compressive after moisture absorption (Figure 32d), but drastically lower than before (Figure 29d). Thus, after the axial compressive loading of -53.4 ksi is applied these stresses become tensile (Figure 38d). Without moisture they were compressive (Figure 35d). In both cases they were not critically high, however, 22.7 ksi and -57.2 ksi, respectively.

The  $\sigma_{11}$  stresses in the  $45^\circ$  plies prior to loading were tensile, but much lower than for the RTD case (compare Figure 32a with Figure 29a). Thus, upon loading, the  $\sigma_{11}$  stress becomes compressive (-29.9 ksi maximum, as indicated in Figure 38a), whereas for the RTD case it remained tensile (54.1 ksi, as indicated in Figure 35a). However, because the -53.4 ksi applied loading represented here is more than one-half of the experimentally measured ultimate strength, this compressive stress in the  $45^\circ$  plies will not become critical prior to composite failure.

As in the RTD loading case, the  $\sigma_{11}$  stresses in the resin pocket region are very high, and compressive. This is probably where first failure initiates in a ply drop-off composite laminate, although its occurrence is not particularly significant in terms of subsequent response.

The  $\sigma_{22}$  stresses are presented in Figure 39. These stresses in the  $0^\circ$  plies are negligible (see Figure 39b as an example) since the moisture absorption had converted the relatively high tensile stresses to small compressive stresses prior to loading. Upon loading, these  $\sigma_{22}$  stresses again become tensile, but of very low magnitude, as indicated in Figure 39b.

Moisture had a similar influence on the  $\sigma_{22}$  stresses in the  $90^\circ$  plies. However, the applied axial compressive loading induces compressive  $\sigma_{22}$  stresses in the  $90^\circ$  plies, rather than tensile. Thus, as indicated in Figure 39d, the maximum compressive stress is about -5.9

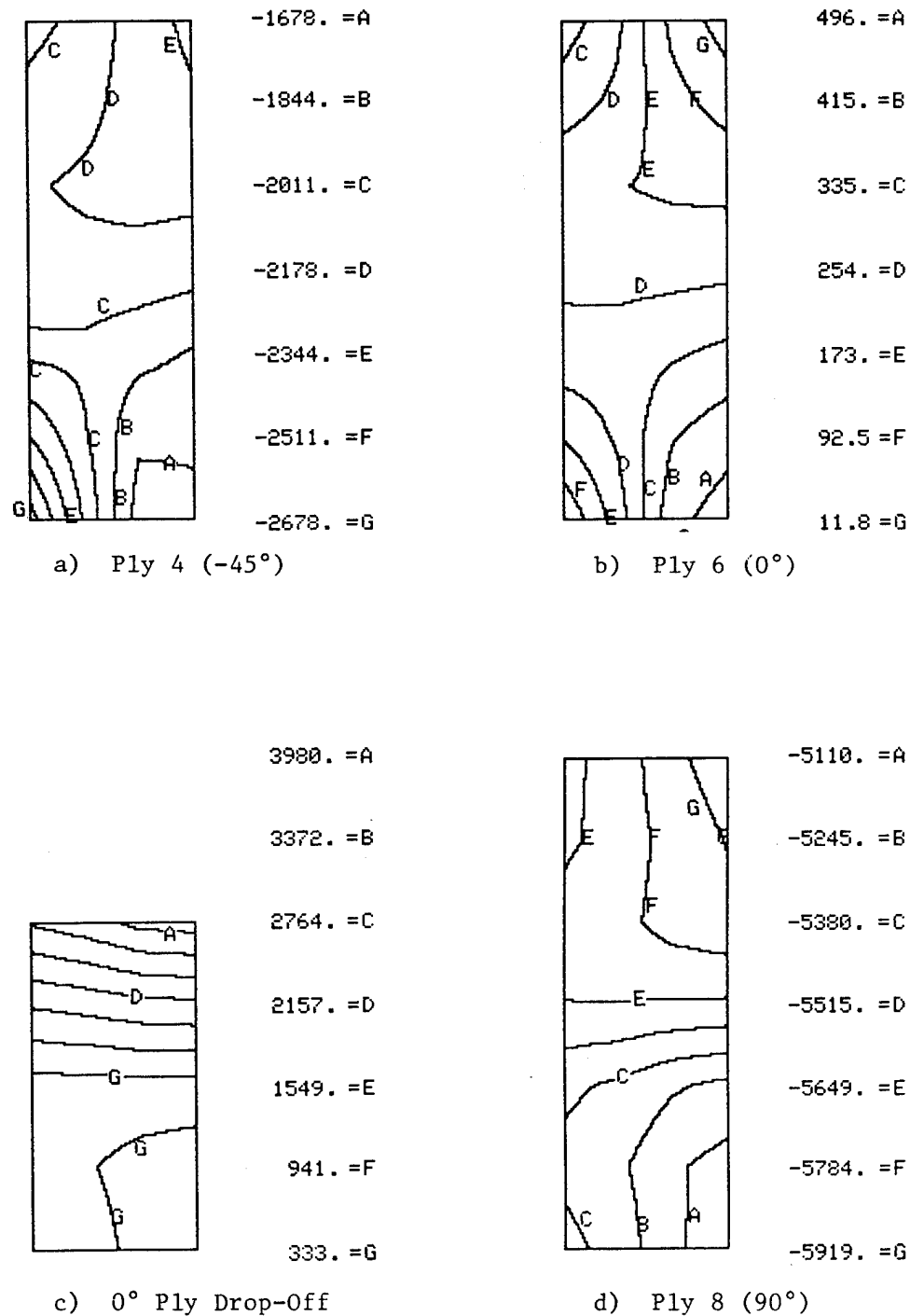


Figure 39. Transverse Stresses ( $\sigma_{22}$ , psi) in Selected Plies after -53.4 ksi Axial Compressive loading; 1% M Moisture Absorption.

ksi. While almost six times higher than the corresponding stress for the RTD condition, it is in fact only 20 percent of the RTW ultimate strength, and still not a potential cause of failure.

The  $\sigma_{22}$  stresses in the 45° plies are also compressive, and only about half as large. The  $\sigma_{22}$  stresses in the neat resin pocket are also not excessive (particularly when compared to the  $\sigma_{11}$  stresses at the same location).

The in-plane shear stresses in the representative plies are presented in Figure 40. The only potentially significant shear stresses are in the 45° plies. These are about twice as high as for the RTD case (compared Figure 40a with Figure 37a), but still only 4.8 ksi. The reason they are higher is that the moisture absorption had negated the favorable cooldown residual stresses. However, at only 5.0 ksi maximum (in Ply 15), they are little more than 30 percent of the RTW ultimate shear strength (Table 5), and hence not likely to contribute significantly to laminate failure.

#### 6.4 Interlaminar Stresses

The interlaminar stresses (i.e., those stresses acting in the 3-direction perpendicular to the plies of the laminate) are not expected to be large due to a ply drop-off alone (neglecting free edge effects, as discussed in Section 6.1). Thus, they were not included in the detailed discussion of Section 6.3, attention being focused on the in-plane stresses.

The interlaminar stresses can readily be calculated, however, to verify that they are small. By definition, the interlaminar normal stress can be referred to either as  $\sigma_{33}$  or  $\sigma_{zz}$ , since the coordinate transformation is a rotation about the normal axis. The two interlaminar shear stresses are defined as  $\tau_{13}$  and  $\tau_{23}$  in the material coordinate system, or  $\tau_{xz}$  and  $\tau_{yz}$  in the geometric coordinate system. In Section 6.3, in discussing in-plane stresses, only material coordinates were referred to. Here it is convenient to use geometric coordinates, so that a given stress component can be displayed for all plies simultaneously. This is acceptable since these stresses are small anyway. Also, only  $\sigma_{zz}$  and  $\tau_{xz}$  will be presented here, as being of more significance than  $\tau_{yz}$ .

Plots of the interlaminar normal stress  $\sigma_{zz}$  are presented in Figure

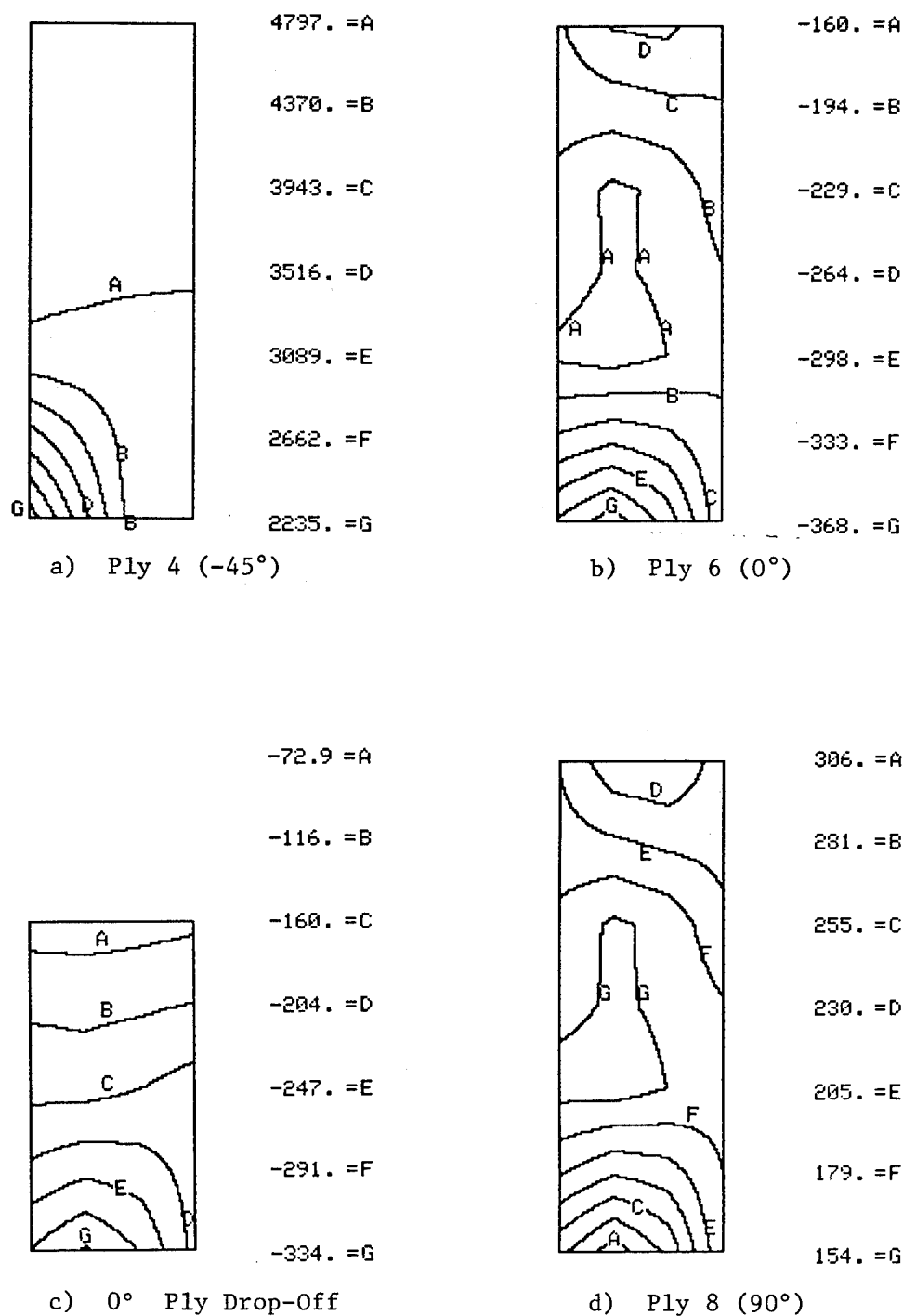


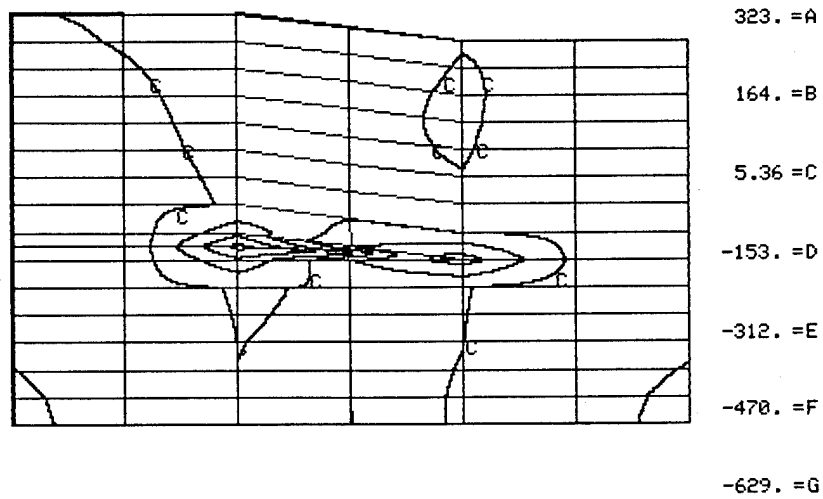
Figure 40. In-Plane Shear Stresses ( $\tau_{12}$ , psi) in Selected Plies after -53.4 ksi Axial Compressive loading; 1%M Moisture Absorption.

41. The stresses at only one longitudinal plane are shown, the variation in the through-the-thickness direction being negligible because of the boundary conditions assumed for this model. Figures 41 a, b, c and d represent the same four loading conditions as discussed in Section 6.3. That is, Figure 41a is the predicted  $\sigma_{zz}$  stress state after cooldown only, Figure 41b is after the addition of one weight percent moisture, Figure 41c is for an axial compressive loading of -41.6 ksi in the RTD condition, and Figure 41d is for an axial compressive loading of -53.4 ksi in the RTW condition. As can be seen, the  $\sigma_{zz}$  stresses remain low under all four conditions. The highest tensile stress is at the tip of the neat resin pocket. The highest compressive stress is in the dropped-off  $0^\circ$  ply near its end.

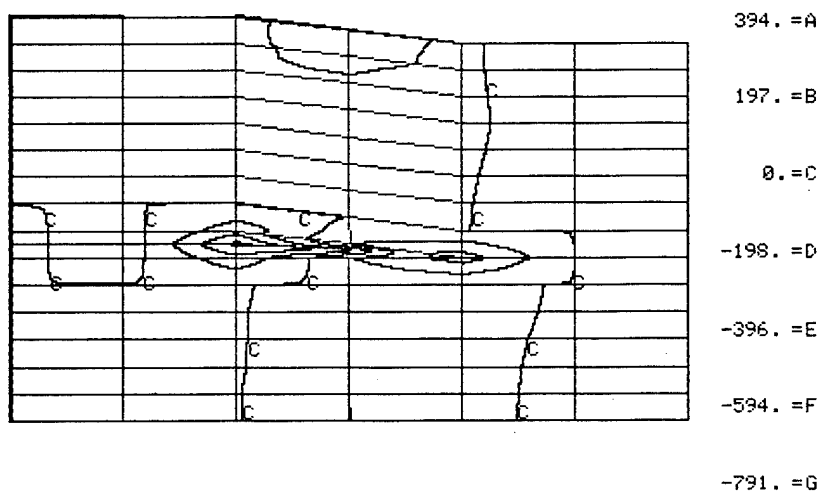
The corresponding interlaminar shear stresses  $\tau_{xz}$  are plotted in Figure 42. These stresses are also low in all cases.

These results indicate that interlaminar stresses induced by a  $0^\circ$  ply drop-off are negligible compared to the in-plane stresses.



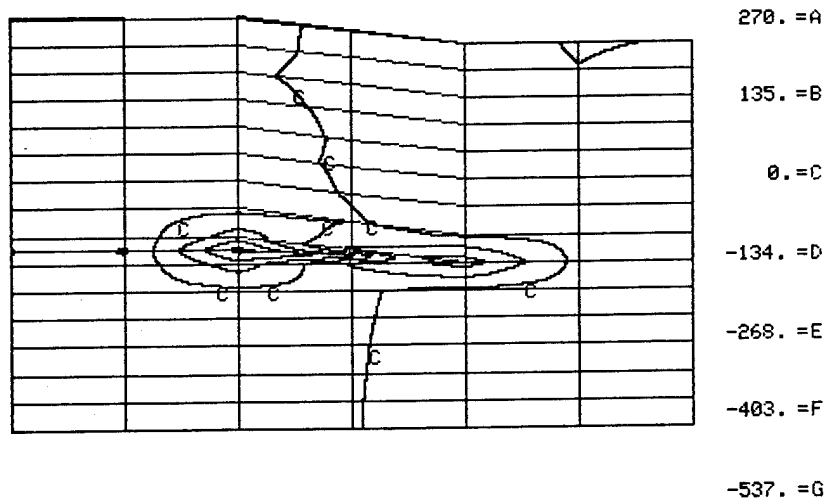


a) After Cooldown from Cure Temperature

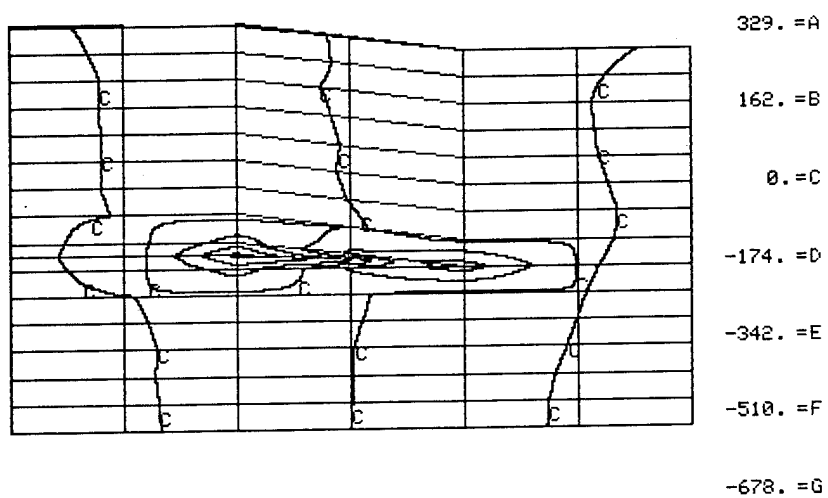


b) After 1%M Moisture Absorption

Figure 41. Interlaminar Normal Stresses ( $\sigma_{zz}$ , psi) Due to  $0^\circ$  Ply Drop-Off in F-18 Laminate.

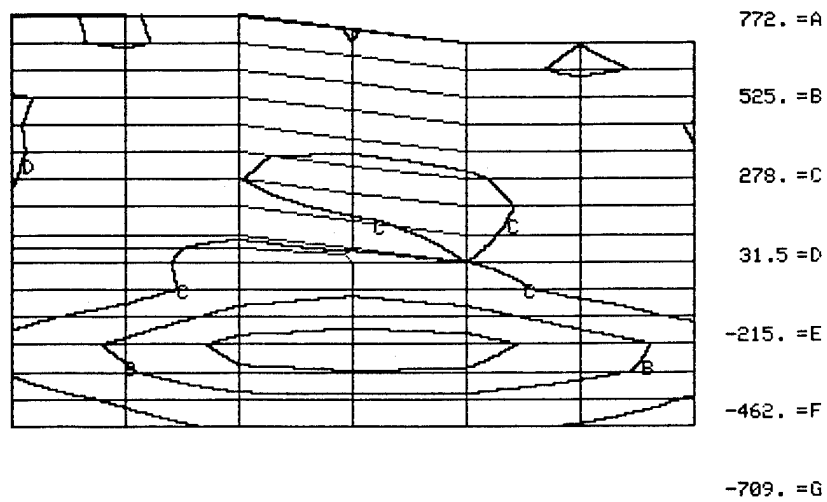


c) Axial Compressive Loading,  $\bar{\sigma}_x = -41.6$  ksi,  
No Moisture

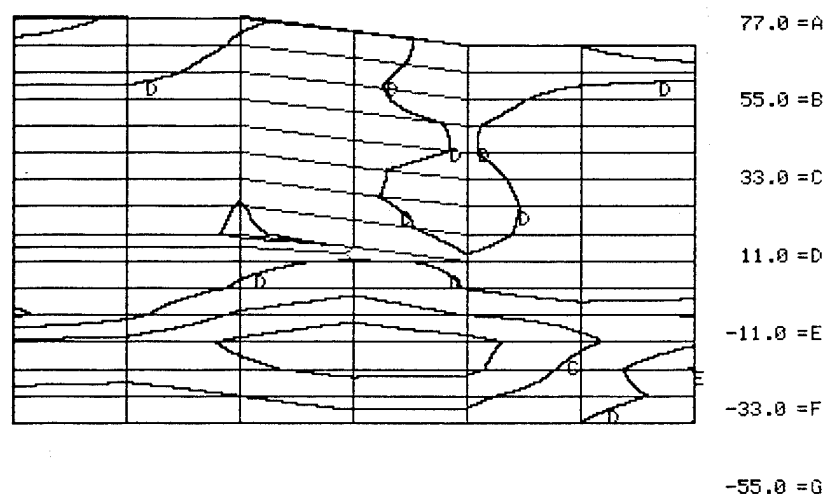


d) Axial Compressive Loading,  $\bar{\sigma}_x = -53.4$  ksi,  
1%M Moisture Content

Figure 41 (Continued). Interlaminar Normal Stresses ( $\sigma_{zz}$ , psi) Due to  $0^\circ$  Ply Drop-Off in F-18 Laminate.

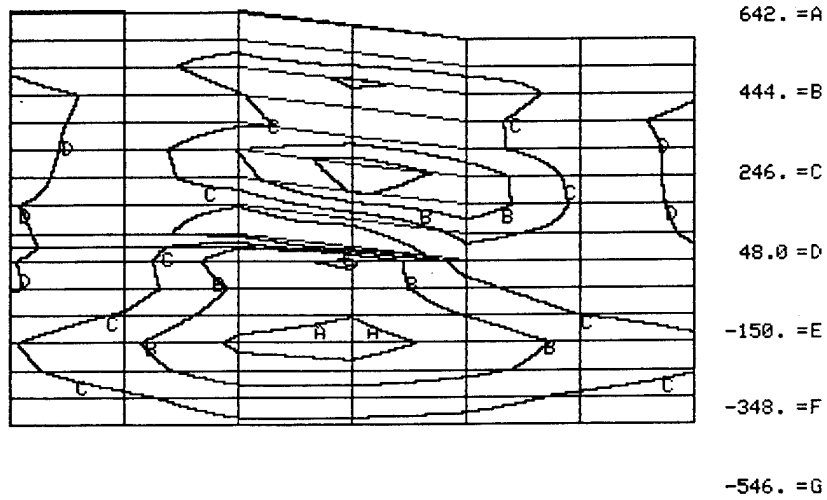


a) After Cooldown from Cure Temperature

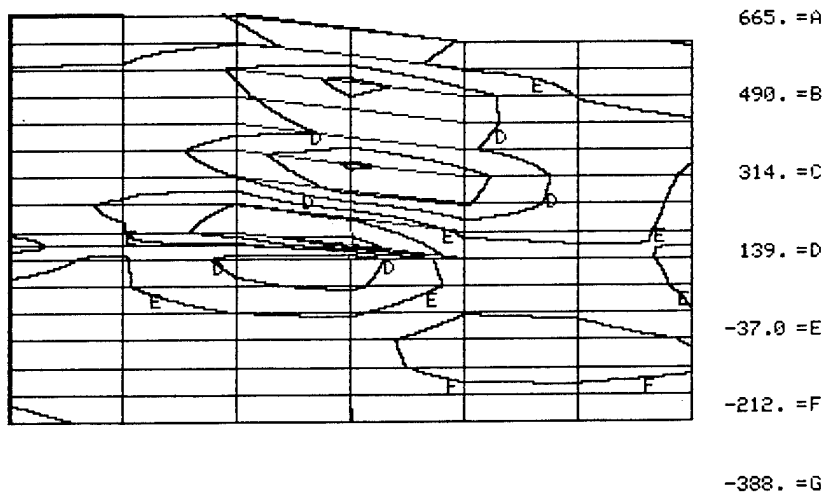


b) After 1%M Moisture Absorption

Figure 42. Interlaminar Shear Stresses ( $\tau_{xz}$ , psi) Due to  $0^\circ$  Ply Drop-Off in F-18 Laminate.



c) Axial Compressive Loading,  $\bar{\sigma}_x = -41.6$  ksi,  
No Moisture



d) Axial Compressive Loading,  $\bar{\sigma}_x = -53.4$  ksi,  
1%M Moisture Content

Figure 42 (Continued). Interlaminar Shear Stresses ( $\tau_{xz}$ , psi) Due to  $0^\circ$  Ply Drop-Off in F-18 Laminate.

## SECTION 7

### LAMINATE CONTAINING A HOLE

Holes were not considered in the prior studies [1-3], the first experimental data being generated as part of the current effort [4]. Holes in laminates are commonly required to accommodate fasteners. Hence loaded as well as unloaded holes need be considered. In the present analytical study, only an unloaded hole in an F-18 laminate subjected to axial compression is considered. This can readily be extended to loaded holes and other types of laminates and laminate loading conditions in future work.

A laminate containing a hole represents a full three-dimensional stress analysis problem. Thus, the same 3-D finite element analysis computer program as described in Section 6 for use in analyzing the ply drop-off geometry can be used here also.

#### 7.1 Finite Element Model

The same 30-ply F-18 laminate tested and analyzed in prior studies was utilized here. In the experimental portion of the current study [4], F-18 laminates with and without porosity, and with and without ply drop-offs were tested with unloaded and loaded holes. For purposes of the present analysis, only an unloaded hole in a 30-ply laminate containing no ply drop-offs or porosity will be considered. The influences on composite response of porosity and ply drop-offs were considered in the two prior sections of this report.

The 30-ply F-18 laminate containing a hole was modeled as indicated in Figure 43. Only one quadrant of the hole circumference and surrounding laminate need be analyzed, because of assumed symmetry conditions. This is not strictly correct here because of the presence of the +45° and -45° plies, which are not symmetrically reflected about the upper and left boundaries of the model of Figure 43a. Around the free curved surface of the hole there is no problem. Also, the right boundary of the model represents the free edge of the compression test

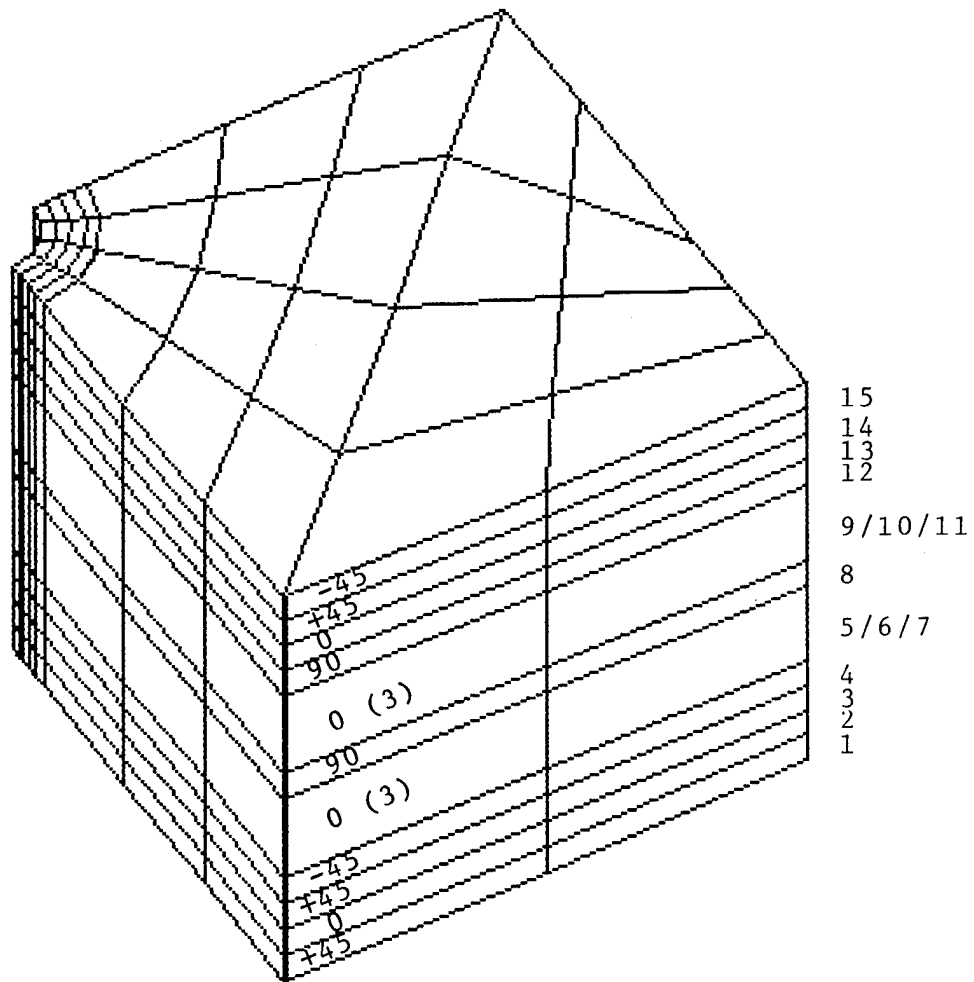


Figure 43. Three-Dimensional Finite Element Model of Hole in F-18 Laminate.

specimen, and hence is not a plane of symmetry. The lower boundary, where the in-plane compressive loading is applied, is assumed to be sufficiently removed from the hole so that its presence does not significantly influence the stress state at the hole. The inaccuracies introduced by the improper modeling of the  $45^\circ$  ply symmetries was permitted here only because the present work is considered as a demonstration of the potential of this analysis tool, rather than a presentation of detailed results. Proper representation would have required the inclusion of all four quadrants in the finite element model, hence increasing the number of individual elements by a factor of four. As can be seen, the one-quadrant model shown in Figure 43 is already very coarse (compared, for example, to the 2-D grids used in Section 5). Yet even this 3-D grid taxes the storage capabilities of the CDC CYBER 760 computer it is run on at present. In future work, as larger computers become available, and more efficient solution techniques are developed even for current computers, much more refined grids and larger models will be possible. Presently, it is the potential of the basic analysis technique which is being demonstrated.

Figure 43 shows an edge of the laminate, indicating the ply stacking sequence. Only one half of the laminate thickness is modeled, as the F-18 laminate is essentially a symmetric laminate (a minor deviation being the  $-45^\circ$  and  $+45^\circ$  plies straddling the midplane; both would have to be of the same orientation for the laminate to be completely symmetric). The bottom ( $45^\circ$ ) ply in Figure 43 is at the midplane; the upper 15 plies of the laminate are represented. Each ply is represented by a single layer of eight-node isoparametric finite elements, except the two groups of three  $0^\circ$  plies separated by the  $90^\circ$  ply, each group being modeled by a single layer of elements. That is, the 15 plies are represented in Figure 43 by a total of 11 layers of elements. With 36 elements per layer the present model consists of 396 elements. Approximately half of these elements are concentrated near the hole boundary, to model local stress gradients as accurately as possible.

The unidirectional ply properties required as input to the finite element analysis are defined in Section 4. These nonlinear orthotropic material properties are defined as functions of both temperature and

moisture.

## 7.2 Predicted Response

Both as-fabricated and moisture-preconditioned specimens containing a hole were to be analyzed. Thus, it was first necessary to apply a thermal loading representing the cooldown from the composite cure temperature. Then the composite was either loaded in axial compression (along the x-axis, i.e., the axis of the 0° plies), or subjected to a one weight percent moisture absorption prior to mechanical loading. Predicted stress contours in selected plies will be presented, after cooldown, after moisture preconditioning, and after mechanical loading is applied.

### 7.2.1 Cooldown Thermal Residual Stresses

The 3-D finite element model of Figure 43 was subjected first to a temperature change from an assumed stress-free temperature of 177°C (350°F), i.e., the composite cure temperature, to room temperature (21°C). This temperature decrease of 156°C was applied in 17 increments.

Any or all of the six components of stress can be plotted for each ply, using either geometric (x, y, z) coordinates or material (1, 2, 3) coordinates, at each temperature increment. Likewise, the corresponding six components of strain, or any other quantity which can be calculated, e.g., effective stress or strain, can be plotted. This obviously provides a huge number of plots to study. For purposes of the present presentation, recognizing that the results obtained here are only approximate because of the coarseness of the finite element grid, only selected plots will be included. Hundreds of additional plots were studied, however, as they would normally be in formulating interpretations of the composite response.

As indicated in Table 6.4 of Reference [1] and elsewhere, the ultimate strengths of a unidirectional ply of Hercules AS/3501-6 graphite/epoxy are reasonably well characterized. Values from Reference [1] are summarized in Table 5 of Section 6. Thus, only in-plane stresses in the material coordinates, i.e.,  $\sigma_{11}$ ,  $\sigma_{22}$ , and  $\tau_{12}$ , will be referred to here, for brevity. These stress components can be readily related to the ply stress ultimates given in Table 5. Also, results will be presented here only for Increment 17, i.e., the stress state



after cooldown to room temperature. The interlaminar stress components, i.e.,  $\sigma_{33}$ ,  $\tau_{13}$ , and  $\tau_{23}$ , would also be of considerable interest, because of their potential importance at free edges (here the right boundary of the model, and the surface of the hole). However, because of the coarseness of the grid used here (particularly at the straight free edge), these were not predicted sufficiently accurately for presentation purposes. Thus, they will not be included here, but will be in future work as more refined grid representations become practical.

In Figure 44, the  $\sigma_{11}$  stress contour plots for Plies 1, 2, 4 and 8 are presented, i.e., for a  $+45^\circ$ ,  $0^\circ$ ,  $-45^\circ$ , and  $90^\circ$  ply, respectively, these being the first plies of their respective orientations from the laminate midplane. It will be noted that the cooldown induces modest compressive stresses in the  $0^\circ$  ply, and considerably higher compressive stresses in the  $90^\circ$  ply, the latter being as much as 50 percent of the ultimate compressive strength (from Table 5). The axial stresses in the  $+45^\circ$  and  $-45^\circ$  plies are tensile, and also relatively high. The other  $45^\circ$  plies for which contour plots are not shown here exhibited similar stress distributions, although they were not totally identical, in either distribution or magnitude. For example, the maximum axial stress contour in Ply 15 (the outermost ply, of  $-45^\circ$  orientation) was over 65 ksi. The differences from one ply to another of identical orientation is due, of course, to differences in coupling induced by neighboring plies.

Perhaps of greater interest than the in-plane axial stress distributions are the in-plane transverse stresses. The same selected plies are shown in Figure 45. The  $+45^\circ$  ply shown is the only  $+45^\circ$  or  $-45^\circ$  ply to indicate any region of possible tensile stress, and as can be seen this is actually only a small region of essentially zero stress at the hole boundary. The -3.9 ksi contour in the  $-45^\circ$  ply shown is the highest compression stress in any  $45^\circ$  ply. The stresses in the other  $0^\circ$  plies not shown here were all tensile, the highest contour being 4.9 ksi near the hole in Plies 9, 10, 11 (modeled as a single layer of elements). The highest tensile stresses occur in the two  $90^\circ$  plies. Both distributions were similar to that shown here for Ply 8; the highest contour in Ply 12 (not shown here) was 5.3 ksi. These highest transverse tensile stresses are about 75 percent of the ultimate

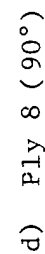
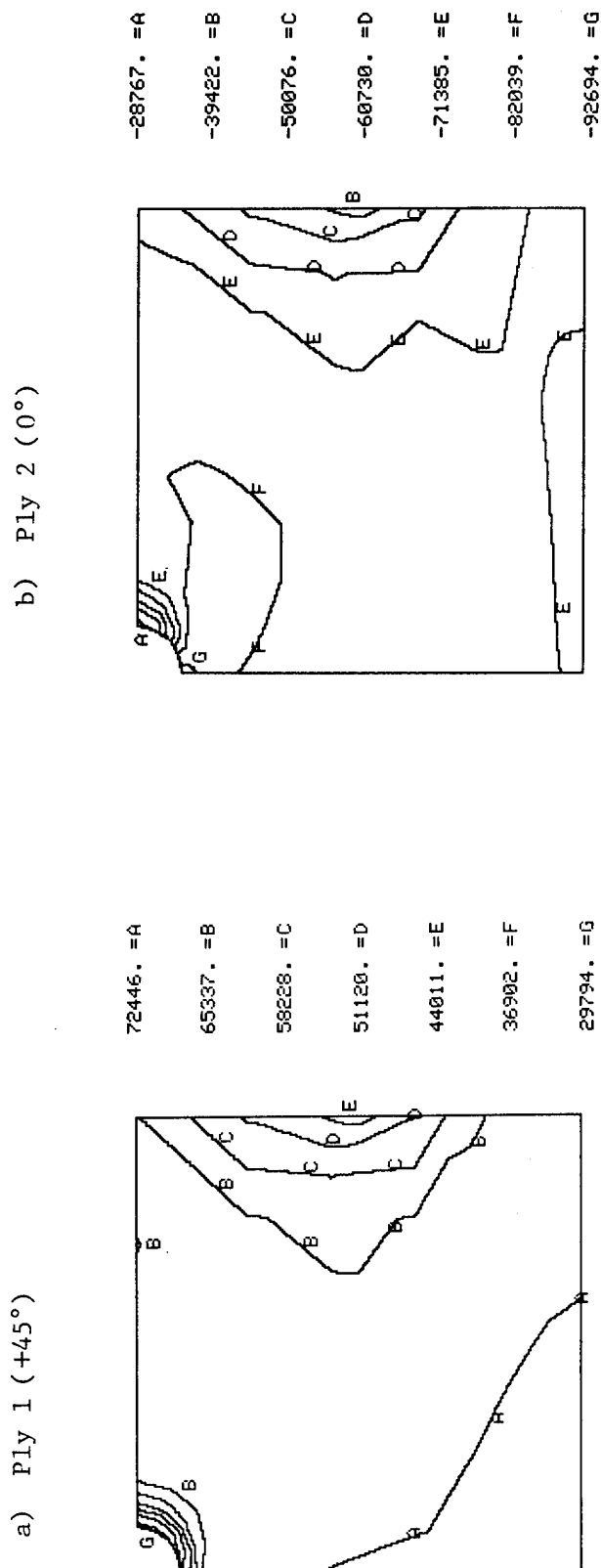
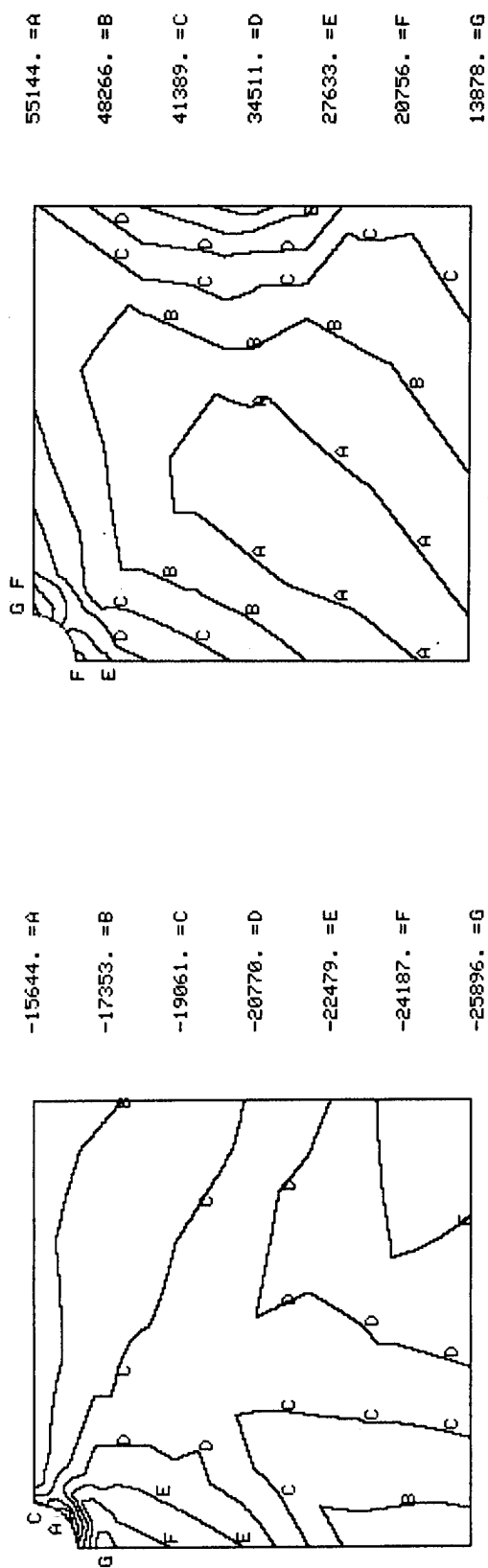
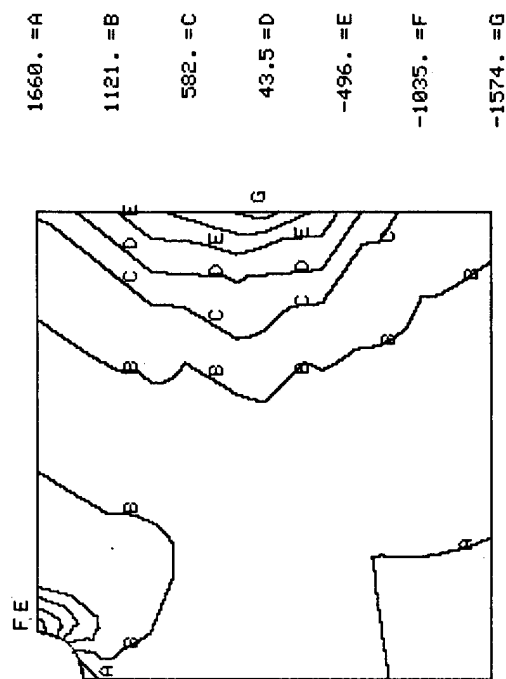
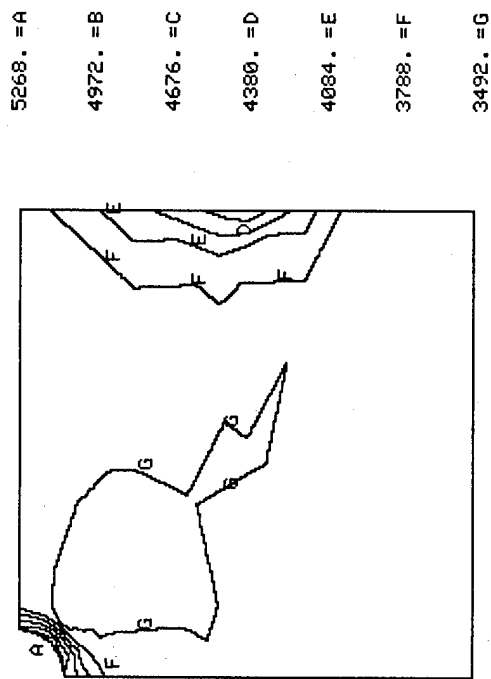


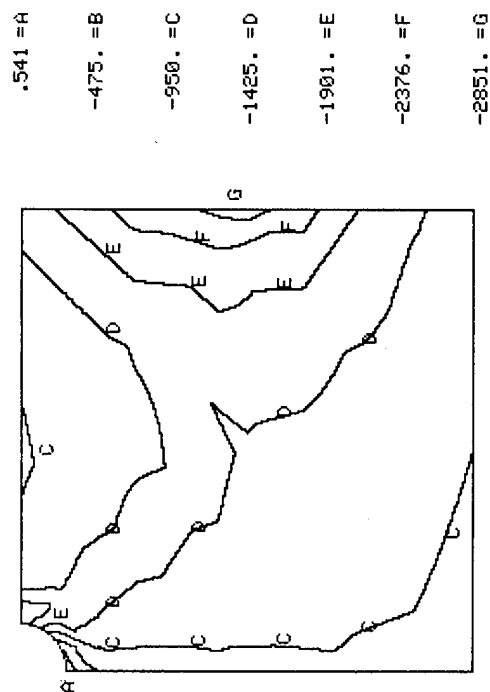
Figure 44. Longitudinal Stresses ( $\sigma_{11}$ , psi) in Selected Plies after Cooldown from Cure Temperature.



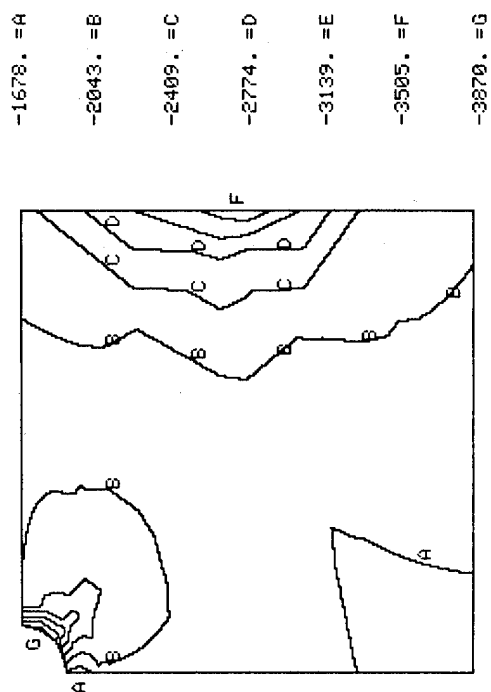
b) Ply 2 (0°)



d) Ply 8 (90°)



a) Ply 1 (+45°)



c) Ply 4 (-45°)

Figure 45. Transverse Stresses ( $\sigma_{22}$ , psi) in Selected Plies after Cooldown from Cure Temperature.

strength (see Table 5), thus certainly not negligible, and they occur at the hole boundary. The maximum compressive stresses are not as significant, being only about 10 percent of ultimate.

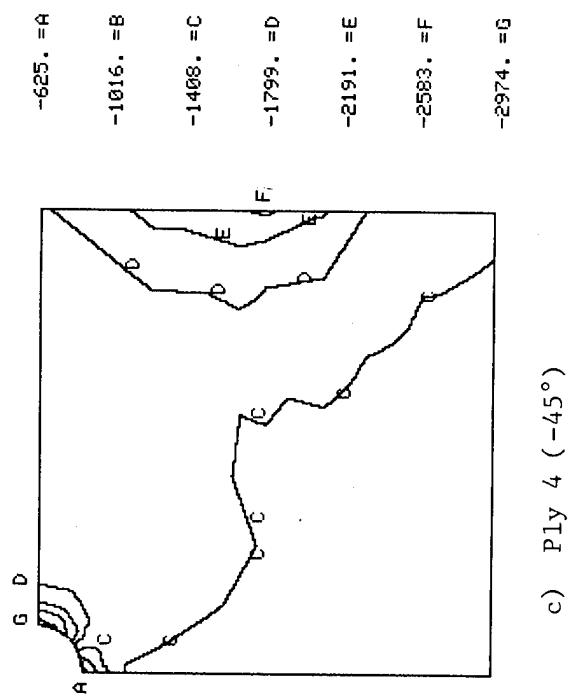
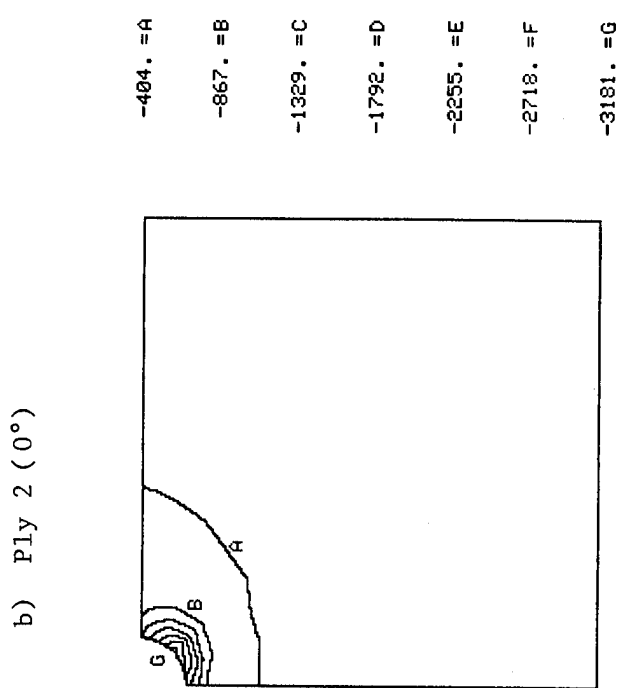
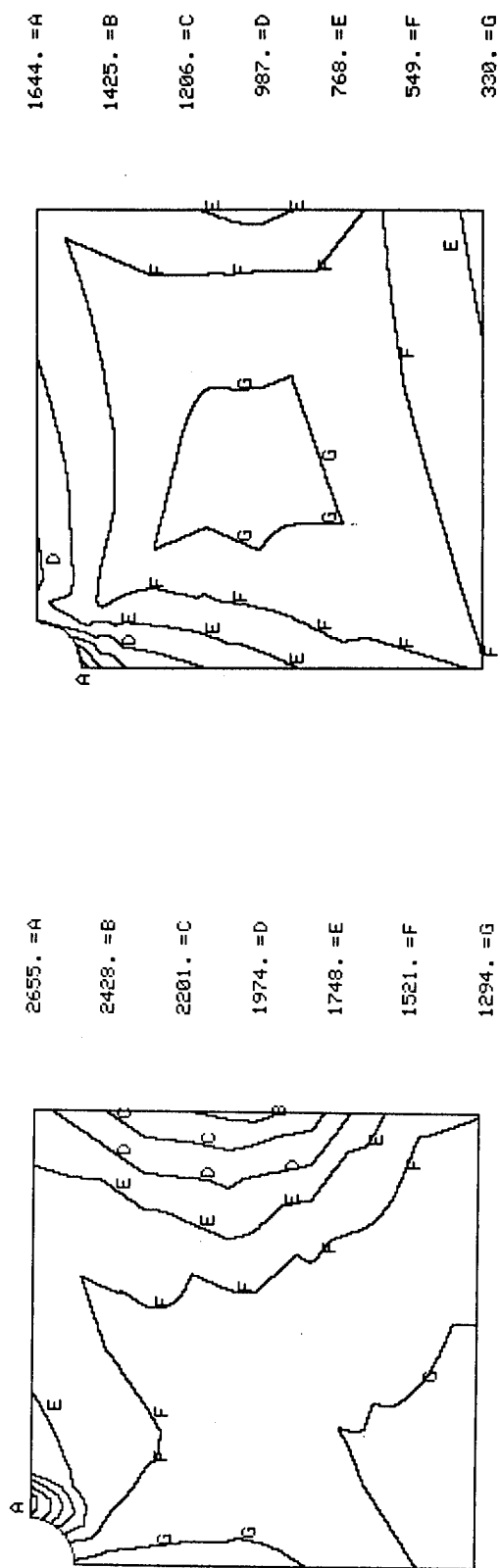
Shear stress contour plots for the same Plies 1, 2, 4 and 8 are presented in Figure 46. These plots are representative of all the plies. The highest shear stress, 3.89 ksi, actually occurred at the hole boundary in the outside (-45°) ply, i.e., Ply 15. Even this local shear stress is only about 20 percent of the ultimate shear strength, however, the AS/3501-6 graphite/epoxy having good shear strength properties (see Table 5).

From these results it can be seen that the transverse tensile stresses developed during cooldown are the most critical, as perhaps expected. However, the axial compressive stresses are also very high, as much as 50 percent of ultimate.

#### 7.2.2 Moisture-Induced Stresses

Axial compressive loading was applied to both dry and moisture-conditioned specimens containing a hole. Moisture absorption of one weight percent (1%M) was modeled in four increments, continuing from the cooldown conditions presented in the previous Section 7.2.1. No attempt was made to model a transient moisture gradient through the laminate thickness, although this can readily be done if desired. Only stress contours for Increment 21 (i.e., after 17 increments of temperature cooldown plus 4 increments of moisture absorption) will be presented here. Both because they are reasonably representative of the other plies, and because this permits direct comparisons with the cooldown stress results of Figures 44 through 46, the same Plies 1, 2, 4 and 8 will be selected here for presentation. Again it will be noted that these are, respectively, the first +45°, 0°, -45° and 90° plies from the midplane of the laminate, respectively. The complete results were available for comparison, however.

The axial stress ( $\sigma_{11}$ ) contour plots are presented for the selected plies in Figure 47. The highest tensile stress (20.1 ksi) occurred in Ply 4, a -45° ply, away from the hole. It will be noted that this is only 28 percent of the tensile stress occurring in the same ply after cooldown, the general distribution of stresses being somewhat similar to the cooldown-stresses-only condition. This reduction of stress is



d) Ply 8 (90°)

Figure 46. In-Plane Shear Stresses ( $\tau_{12}$ , psi) in Selected Plies after Cooldown from Cure Temperature.

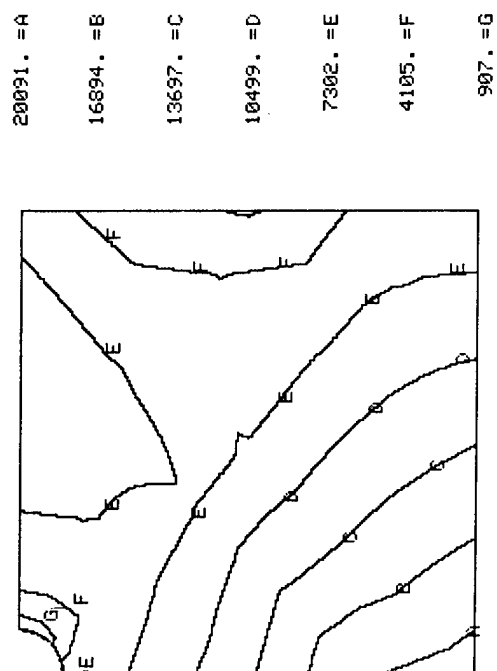
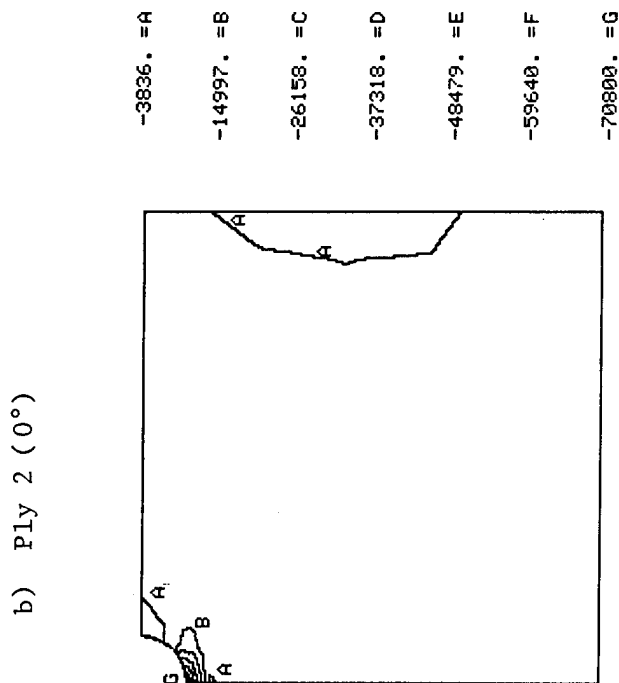
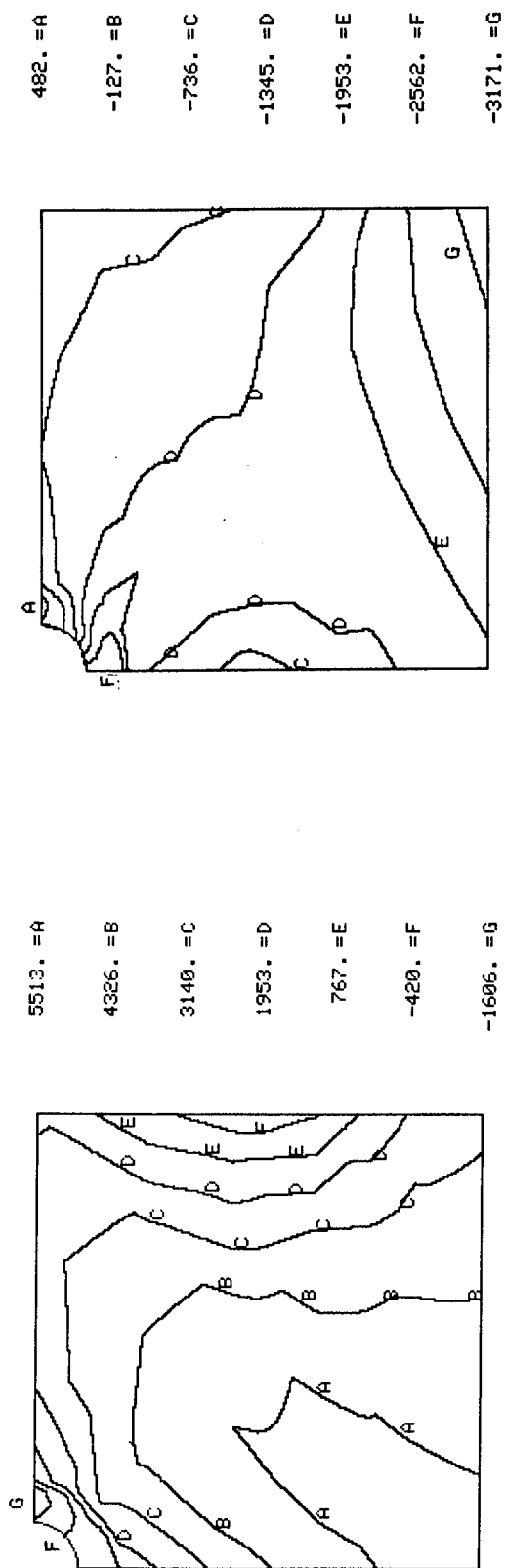


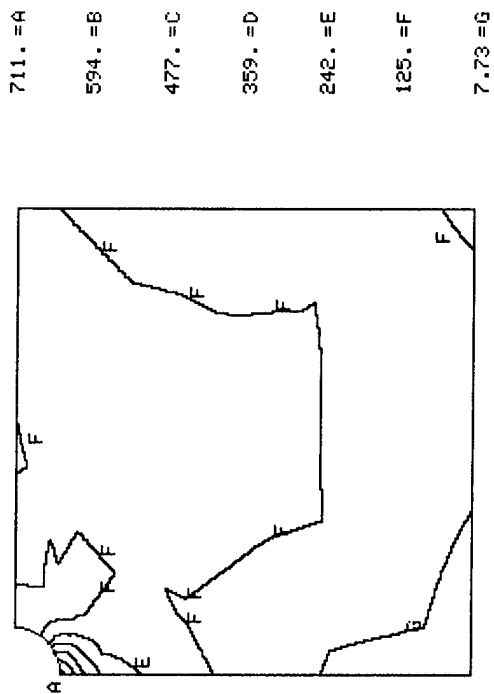
Figure 47. Longitudinal Stresses ( $\sigma_{11}$ , psi) in Selected Plies after 1%M Moisture Absorption.

expected since the moisture swelling tends to offset the thermal contraction previously induced. The axial compressive stresses in every ply are likewise reduced with the addition of moisture. The highest compressive stress still occurs in Ply 8, a 90° ply, but at -70.8 ksi it is 24 percent lower than the cooldown-only stress indicated in Figure 44d. It also occurs at the edge of the hole, as expected.

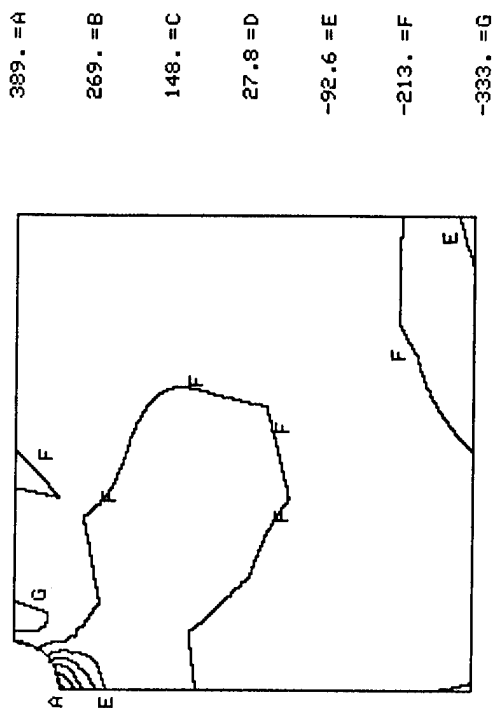
Transverse stress ( $\sigma_{22}$ ) contour plots are presented in Figure 48. As for the axial stresses, the distribution of transverse stresses is similar to that exhibited after cooldown only, and the magnitudes are again reduced due to the addition of one weight percent moisture. The highest tensile stress again occurred in Ply 12, and at 1.2 ksi was 77 percent lower than before. As shown in Table 5, the transverse tensile ultimate strength is reduced by 1 ksi, to 6.0 ksi, with the addition of one weight percent moisture. Thus, the highest tensile stress in Ply 12 is 20 percent of ultimate. In the room temperature, dry condition, the highest tensile stress was 75 percent of ultimate, as previously noted. Thus, even though the addition of moisture reduced the ply transverse tensile strength, this was more than offset by the corresponding reduction in stress. The highest compressive stress was again near the surface of the hole, but in Plies 9, 10, and 11, the 0° plies. However, it was only 13 percent of that for the case of thermal stresses only, and about 2 percent of the compressive ultimate strength at the 21°C, 1%M condition (see Table 5).

The shear stress ( $\tau_{12}$ ) distributions after moisture preconditioning were perhaps even more similar to the cooldown stress distributions than was previously shown for the  $\sigma_{11}$  and  $\sigma_{22}$  stresses. This can be seen by comparing the individual plots of Figure 49 with those of Figure 46. After the moisture absorption the highest shear stress occurs in the outer -45° ply (Ply 15), just as before the addition of moisture. At 1.1 ksi, this highest stress is 72 percent less than the highest stress before moisture absorption. It is also only 7 percent of the ultimate shear strength of 16.0 ksi for this environmental condition (Table 5).

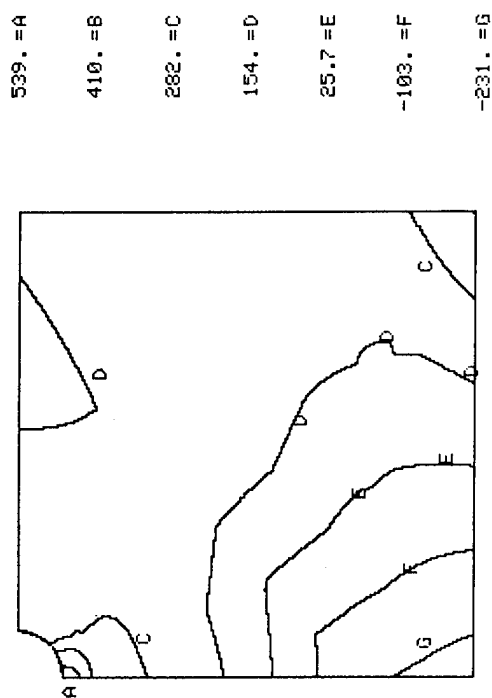
In summary, the uniform addition of one weight percent moisture is actually beneficial in the sense of reducing the cooldown-induced thermal stresses. The residual axial compressive stresses are the most critical, being about 43 percent of ultimate.



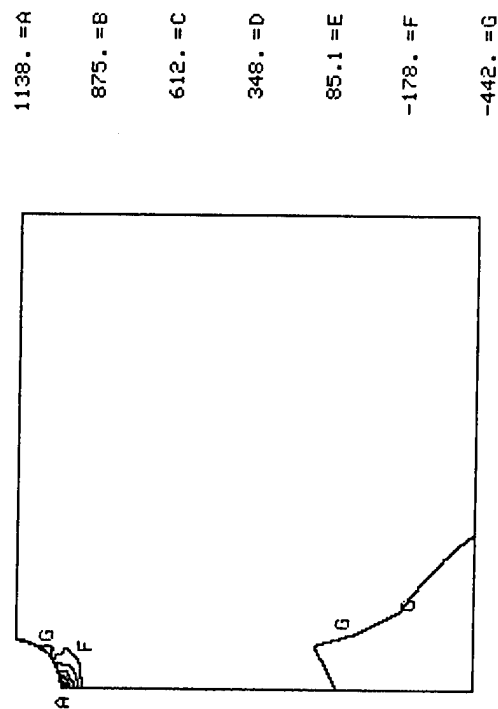
a) Ply 1 (+45°)



b) Ply 2 (0°)



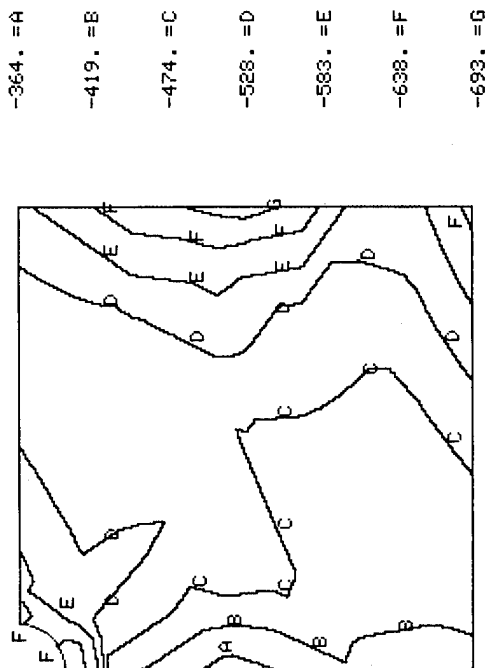
c) Ply 4 (-45°)



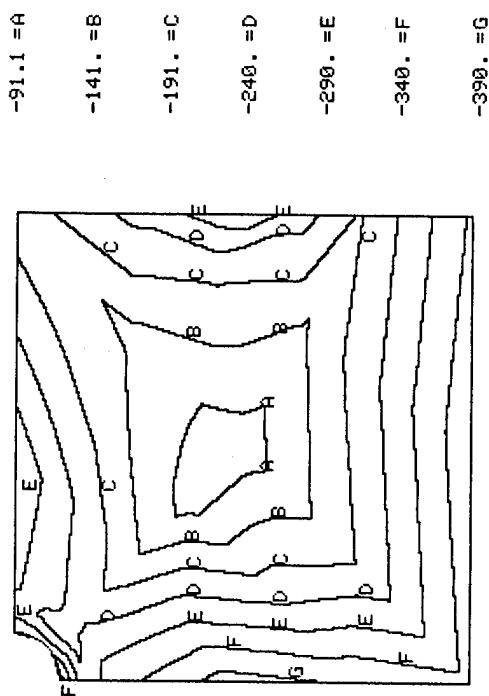
d) Ply 8 (90°)

Figure 48. Transverse Stresses ( $\sigma_{22}$ , psi) in Selected Plies after 1%M Moisture Absorption.

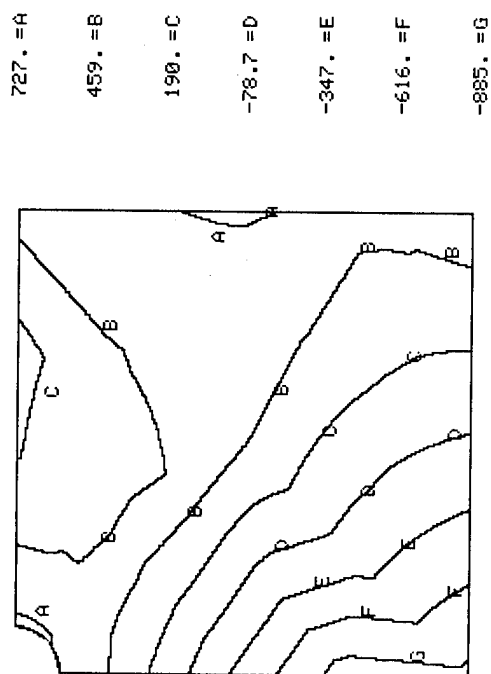




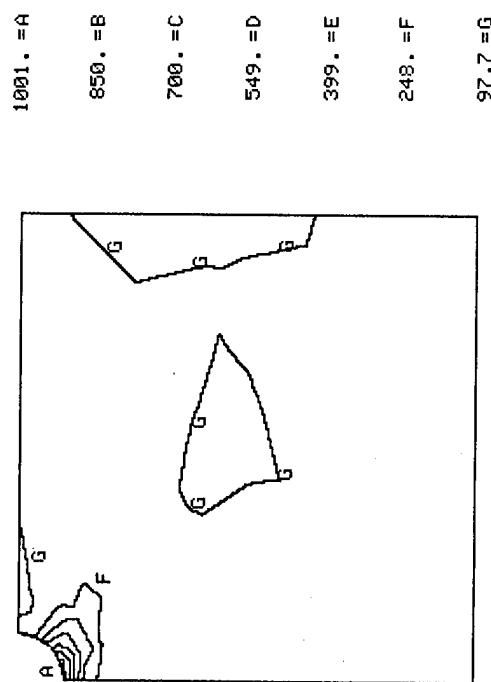
a) Ply 1 (+45°)



b) Ply 2 (0°)



c) Ply 4 (-45°)



d) Ply 8 (90°)

Figure 49. In-Plane Shear Stresses ( $\tau_{12}$ , psi) in Selected Plies after 1%M Moisture Absorption.

### 7.2.3 Axial Compressive Loading

Axial compressive loading was applied, at room temperature, to both the as-fabricated and the moisture preconditioned laminates containing a hole. These results will be presented in separate subsections, and then compared.

#### 7.2.3.1 Room Temperature, Dry Condition

As described in Section 7.2.1, the cooldown from the cure temperature to room temperature had been achieved in 17 increments. Increments 18 through 25 were then applied as axial compression loading increments. These 8 load increments were of varying magnitude, starting at  $\Delta\bar{\sigma}_x$  of only 1 ksi, and then increasing to 6 ksi. The sizes of the increments can be varied as desired, to be compatible with the type of material nonlinearity being modeled. Stress contour results will be presented here only for Increment 25, at which point the applied axial stress had reached -42.7 ksi. Stress contours for each of the other 7 loading increments are also available, of course, for comparison purposes.

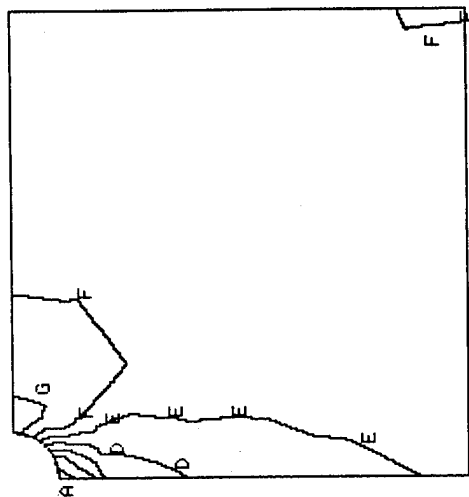
The composite response is strongly dominated by the large number of 0° plies in the laminate, and hence is essentially linear over the full range of loading indicated. This was true of the experimental data as well, individual stress-strain curves for various combinations of porosity, ply drop-offs, and holes being given in Appendix C of Reference [4].

To remain consistent with the presentations of Sections 7.2.1 and 7.2.2, stress contour plots will be presented here only for the three in-plane stress components in the material coordinate directions, i.e.,  $\sigma_{11}$ ,  $\sigma_{22}$ , and  $\tau_{12}$ , and only for Plies 1, 2, 4 and 8.

Figure 50 contains the contour plots of axial ( $\sigma_{11}$ ) stresses in the selected plies. These and subsequent results are for Increment 25, representing an applied axial compressive stress  $\bar{\sigma}_x$  of -42.7 ksi. As can be seen, the high compressive stresses are in the 0° ply (Ply 2), as expected. The highest compressive stress did actually occur in Ply 2, being -108.4 ksi near the surface of the hole, as indicated in Figure 50b. This is 62 percent of the compressive ultimate stress of -175 ksi (Table 5).

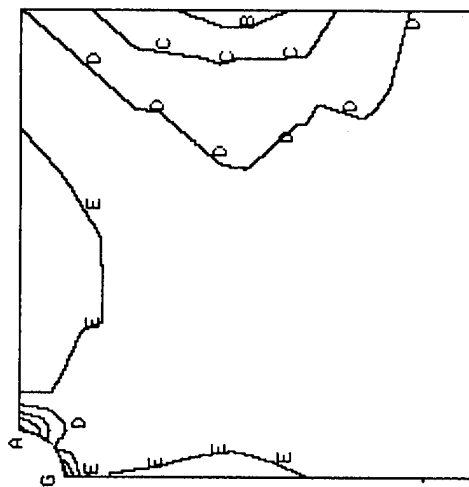
The transverse stress ( $\sigma_{22}$ ) plots are shown in Figure 51. The

-27576. =A  
 -41049. =B  
 -54532. =C  
 -67995. =D  
 -81468. =E  
 -94941. =F  
 -108414. =G



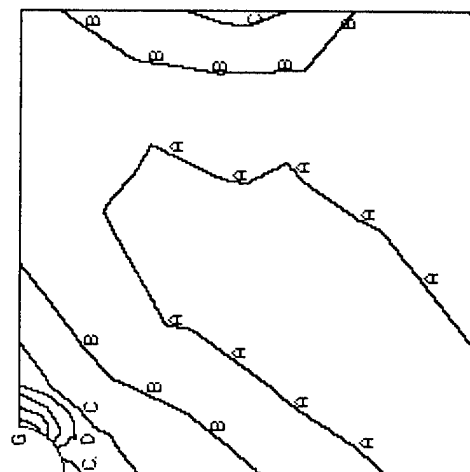
b) Ply 2 (0°)

-22014. =A  
 -31143. =B  
 -40272. =C  
 -49400. =D  
 -58529. =E  
 -67658. =F  
 -76786. =G



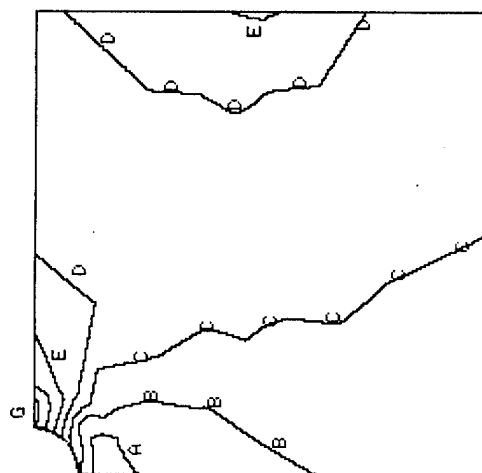
d) Ply 8 (90°)

30952. =A  
 20987. =B  
 11022. =C  
 1057. =D  
 -8908. =E  
 -18873. =F  
 -28838. =G



a) Ply 1 (-45°)

74246. =A  
 61398. =B  
 48549. =C  
 35701. =D  
 22853. =E  
 10005. =F  
 -2844. =G



c) Ply 4 (-45°)

Figure 50. Longitudinal Stresses ( $\sigma_{11}$ , psi) in Selected Plies after -42.7 ksi Axial Compressive Loading; No Moisture.

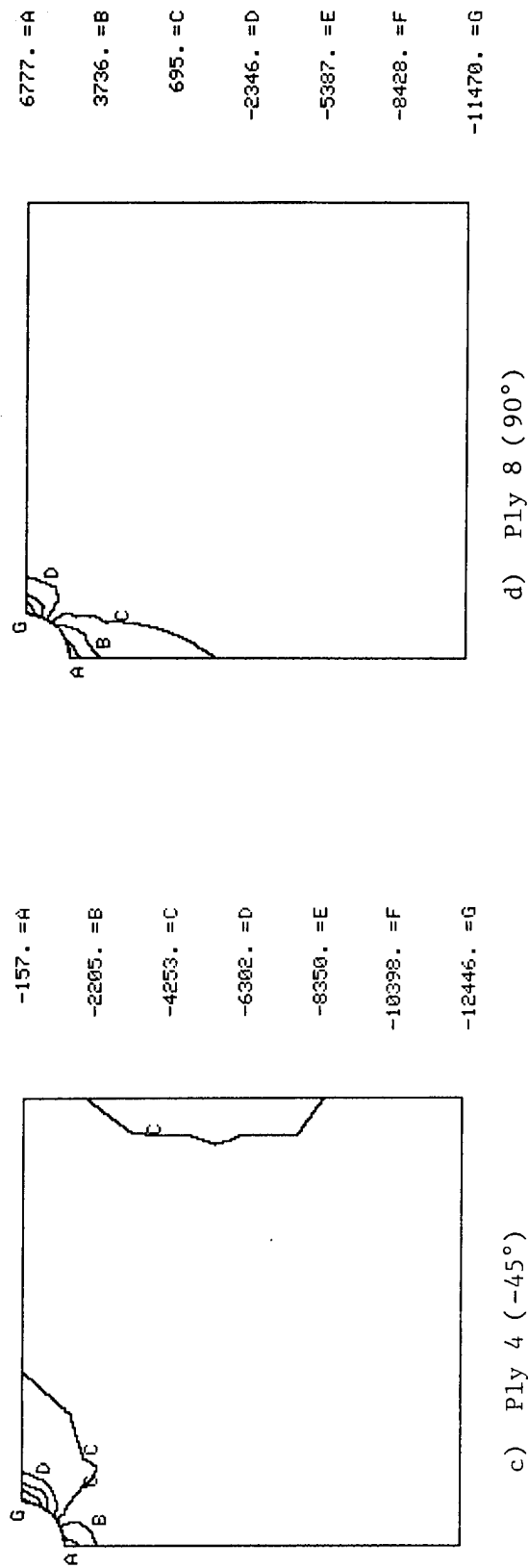
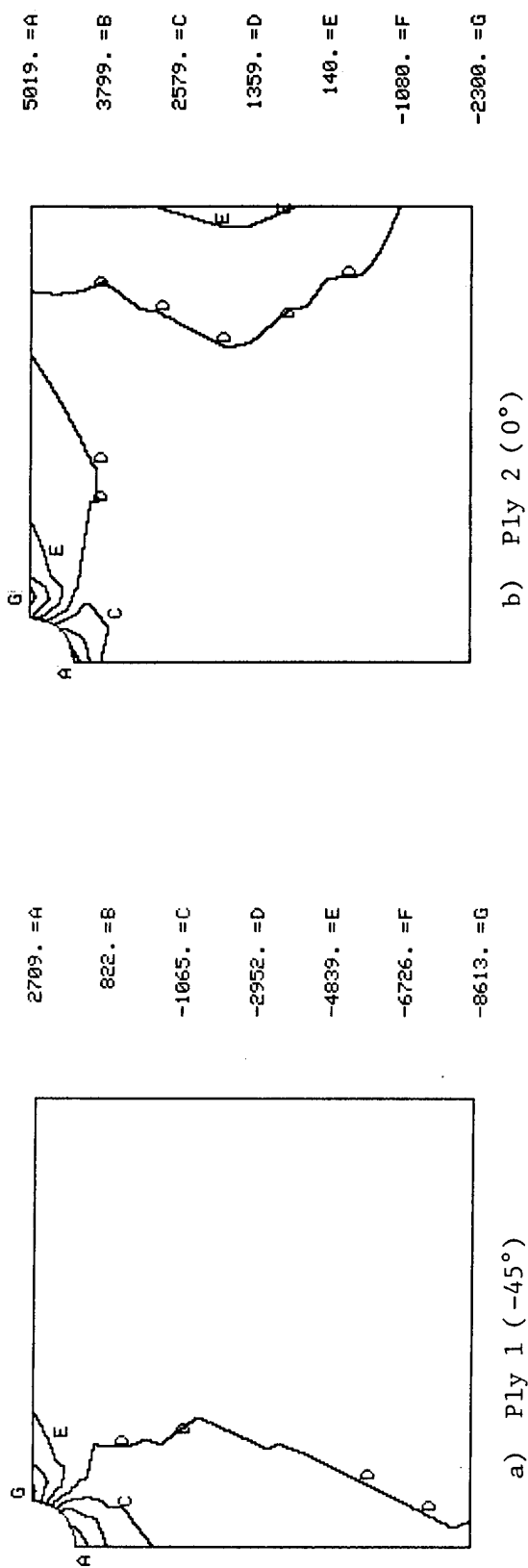


Figure 51. Transverse Stresses ( $\sigma_{22}$ , psi) in Selected Plies after -42.7 ksi Axial Compressive Loading; No Moisture.

highest tensile stress occurred in Ply 8, a 90° ply (see Figure 5ld, where  $\sigma_{22} = 6.8$  ksi); the transverse tensile stresses in the 0° plies were almost as high. These local stress concentrations occurred near the surface of the hole, in the same location indicated in Figure 5ld. These stresses are nearly equal to the tensile ultimate strength of 7.0 ksi, suggesting that failure would have occurred locally at the hole at an only slightly higher applied stress. The highest transverse compressive stress occurred in the -45° Ply 4 (Figure 5lc), at a point 90° around the hole circumference from the highest tensile stress in the 90° ply. This highest compressive stress was -12.4 ksi, which is only 34 percent of the compressive ultimate strength of -37.0 ksi. The relatively high tensile residual stresses developed during cooldown in the hole region of the 90° plies (see, for example, Figure 45d) were a favorable influence in keeping the compressive loading induced stresses moderate in these plies, whereas they were unfavorable with respect to the loading-induced tensile stresses 90° around the hole.

The induced in-plane shear stresses ( $\tau_{12}$ ) in all plies are well represented by the stress states indicated in Figure 52. The high stresses occurred near the hole, at the minimum cross section. The highest shear stress, in the first (+45°) ply, was 8.5 ksi, which is 47 percent of the ultimate shear strength of 18.1 ksi.

In summary, the hole creates a significant stress concentration, the transverse tensile stresses induced in the 90° plies being predicted to cause first failure. However, the transverse tensile stresses in the 0° plies are also very high, suggesting that fiber microbuckling at the surface of the hole at the minimum cross section would eventually occur due to loss of lateral support. The shear stress distributions, aided by the combination of a high ultimate shear strength and favorable cooldown-induced residual stresses, were not as significant.

#### 7.2.3.2 Room Temperature, Wet Condition

As described in Section 7.2.2, the combination of temperature cooldown and the addition of one weight percent moisture occupied a total of 21 solution increments. A compressive axial loading was then applied in 10 increments, in a progression similar to that for the room temperature, dry case. This resulted in a cumulative applied stress  $\bar{\sigma}_x$  of -54.7 ksi (as compared to -42.7 ksi for the room temperature, dry

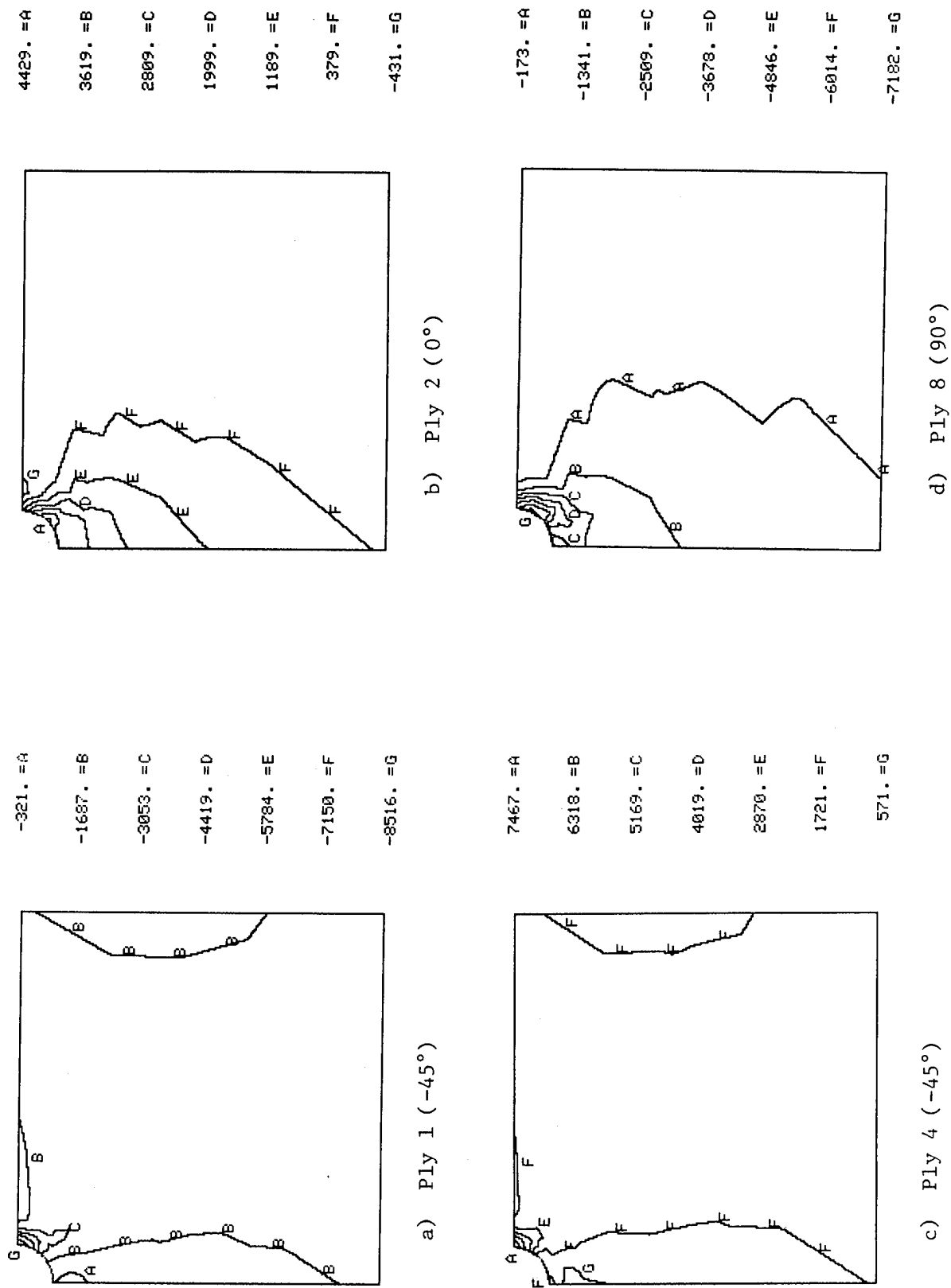


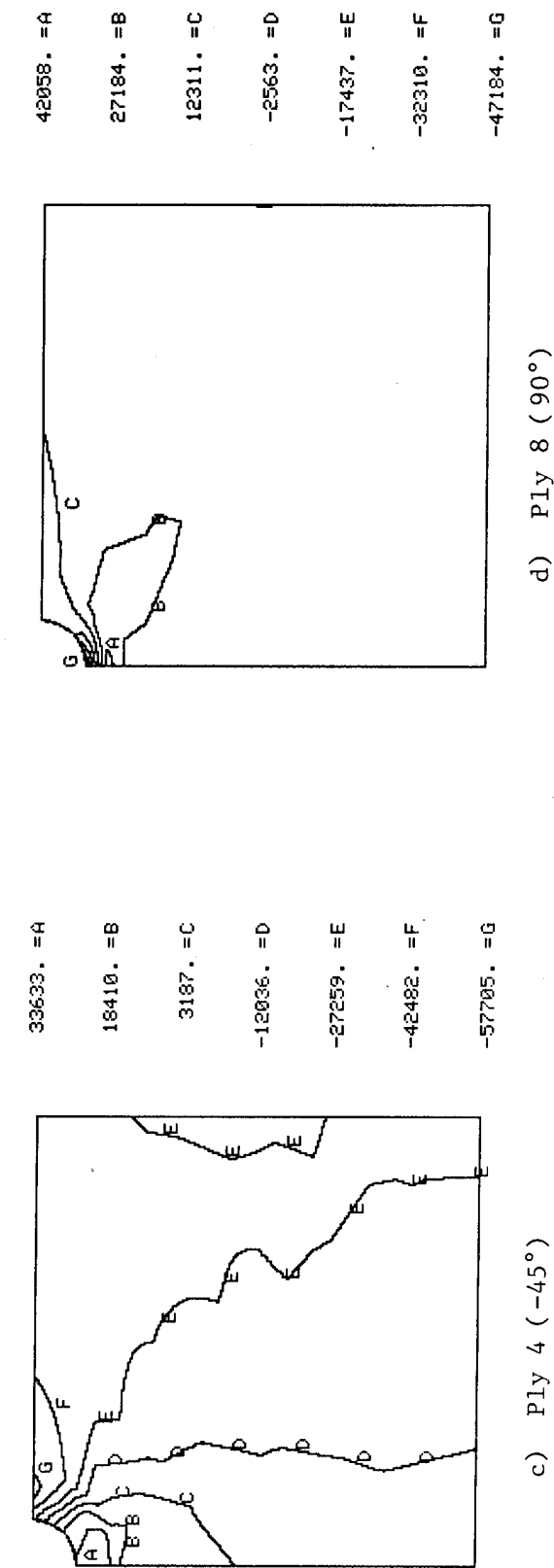
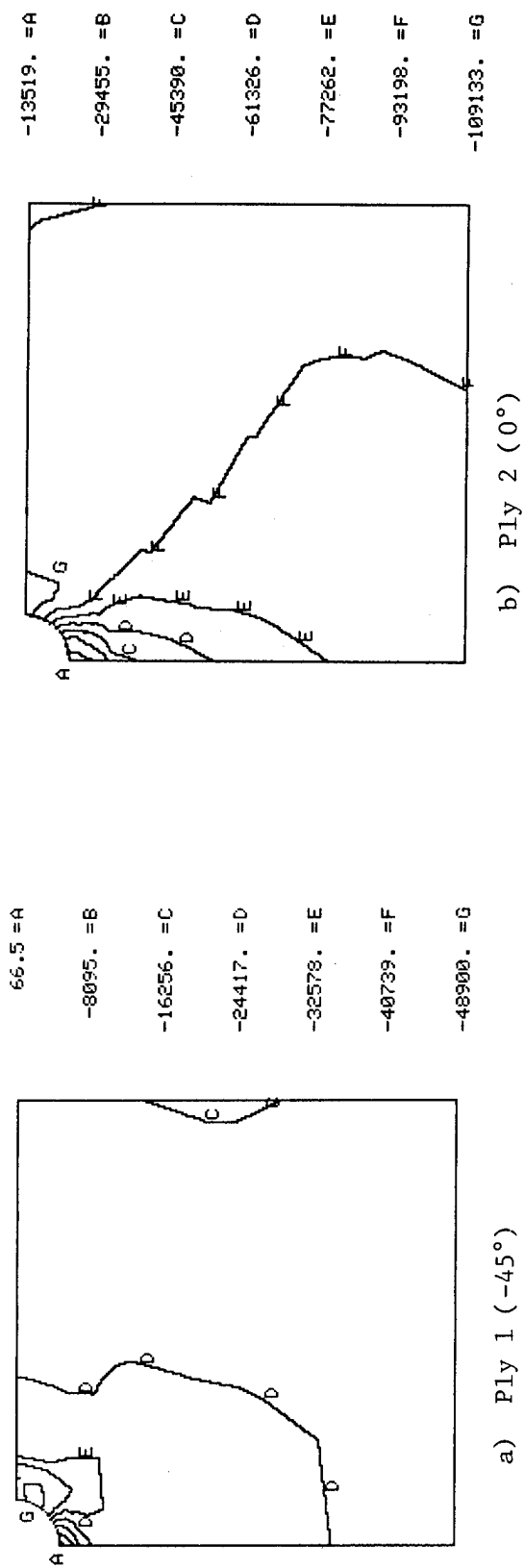
Figure 52. In-Plane Shear Stresses ( $\tau_{12}$ , psi) in Selected Plies after -42.7 ksi Axial Compressive Loading; No Moisture.

condition), corresponding to solution Increment 31. These are the stress contour plots presented here, again for Plies 1, 2, 4 and 8 only. The corresponding composite stress-strain response curve for this environmental condition was also relatively linear, as was that for the room temperature, dry condition. The RTW condition resulted in a slightly higher average stiffness, i.e., at a given stress level the corresponding strain was less. This is consistent with the experimental data [4], lower ultimate strains being recorded when moisture was present.

Axial stress ( $\sigma_{11}$ ) contours in Plies 1, 2, 4 and 8 are presented in Figure 53. As for the RTD case, the high compressive stresses occur in the  $0^\circ$  plies, as expected. The highest stress occurred in Ply 13 (-114.2 ksi), although the stress in all of the  $0^\circ$  plies was at least -109 ksi. It will be noted that although the applied stress is 28 percent higher here than for the RTD case, this stress is actually only 5 percent higher. That is, the addition of moisture reduced the axial stress concentration slightly. However, the RTW compressive ultimate strength is also lower, by about 7 percent (see Table 5).

The transverse stress ( $\sigma_{22}$ ) contours are shown in Figure 54. Again, the presence of moisture has reduced the stress levels, by partially offsetting the cooldown-induced thermal stresses. A secondary influence is the ply material stiffness reduction induced by the moisture (see Section 4), which tends to reduce the magnitudes of the stress concentrations. The highest transverse tensile stresses occur in the  $0^\circ$  plies, near the surface of the hole, the maximum value occurring in the  $0^\circ$  Plies 9, 10 and 11, viz, 11.0 ksi. Unlike for the axial compressive stresses, this is a higher stress concentration due to moisture absorption prior to mechanical loading, and is compounded by the fact that the transverse tensile ultimate strength is lower (see Table 5).

Figure 55 indicates the in-plane shear stress ( $\tau_{12}$ ) distributions in the selected plies. The highest stress occurs in the  $-45^\circ$  Ply 4 (9.9 ksi; see Figure 55c), although as for the RTD case the stress in the outside ( $-45^\circ$ ) ply is also high, viz, 9.2 ksi. This highest stress is only 62 percent of the 16.0 ksi ultimate shear strength at the RTW condition (Table 5).



b) Ply 2 (0°)

d) Ply 8 (90°)

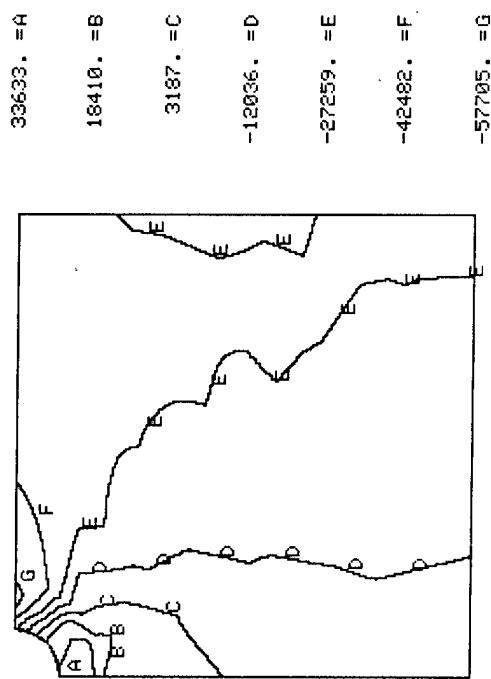


Figure 53. Longitudinal Stresses ( $\sigma_{11}$ , psi) in Selected Plies after -54.7 ksi Axial Compressive Loading; 1%M Moisture Absorption.



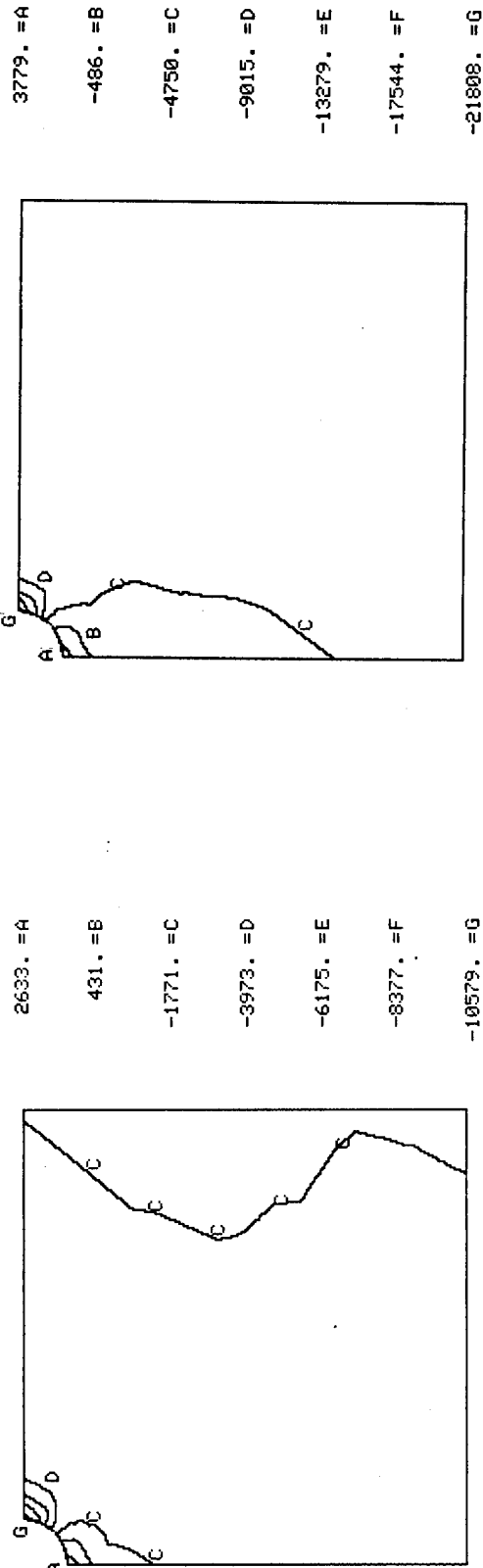
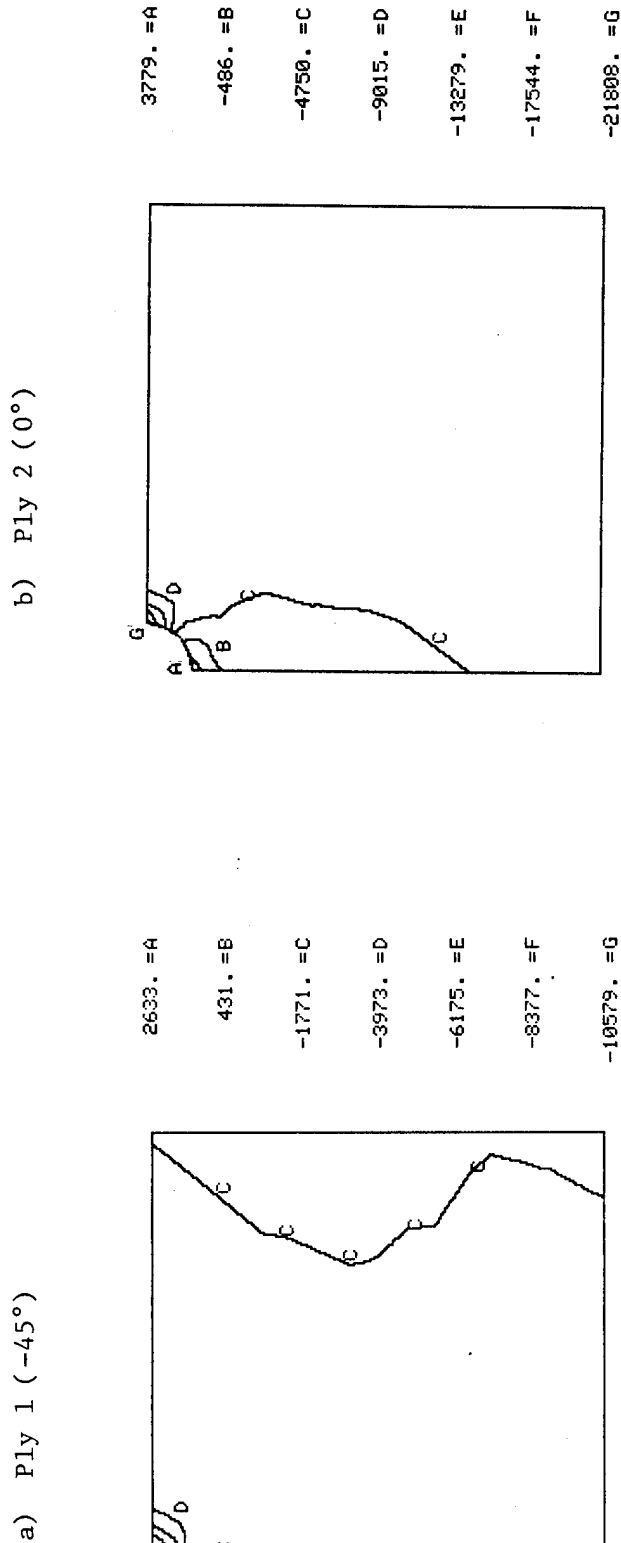
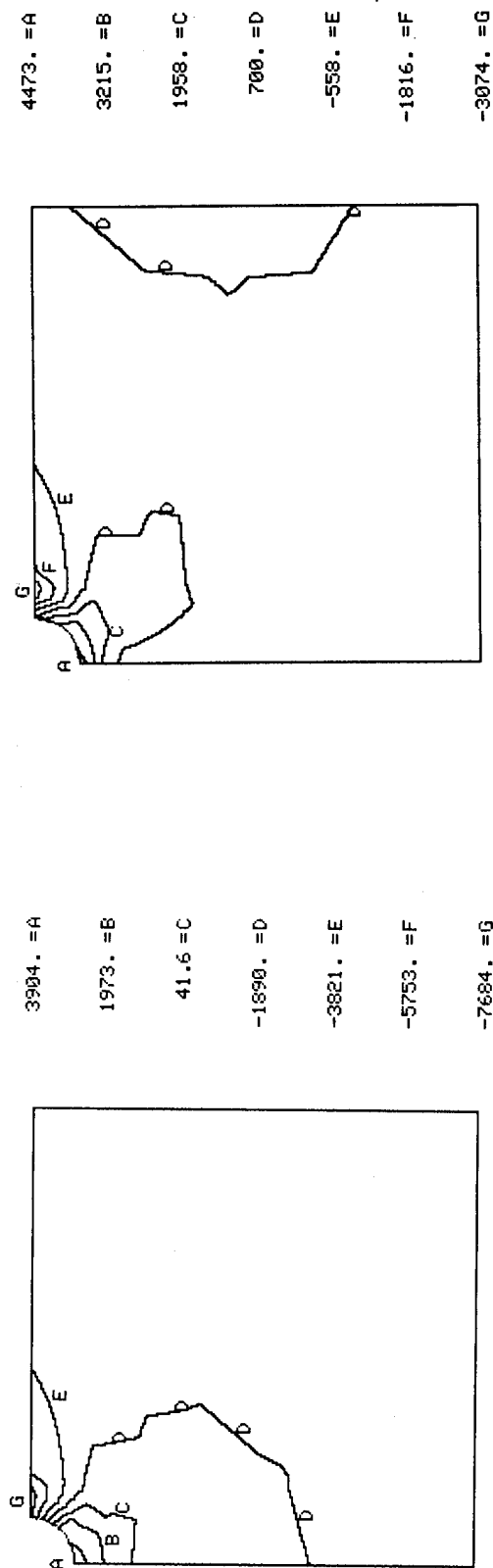


Figure 54. Transverse Stresses ( $\sigma_{22}$ , ksi) in Selected Plies after -54.7 ksi Axial Compressive Loading; 1%M Moisture Absorption.

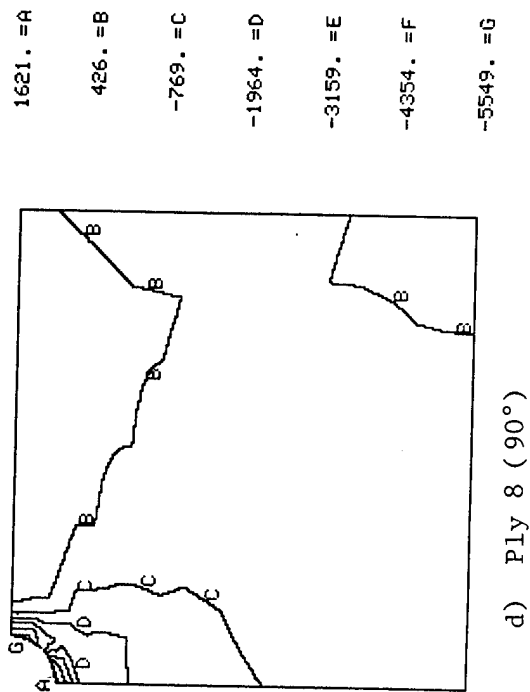
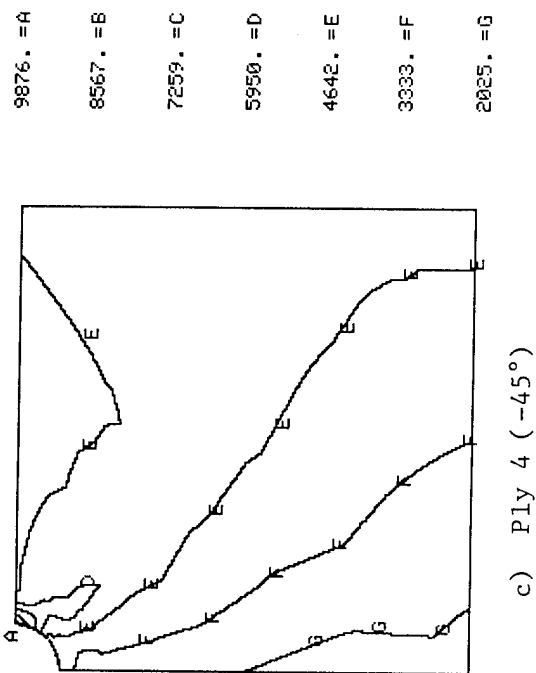
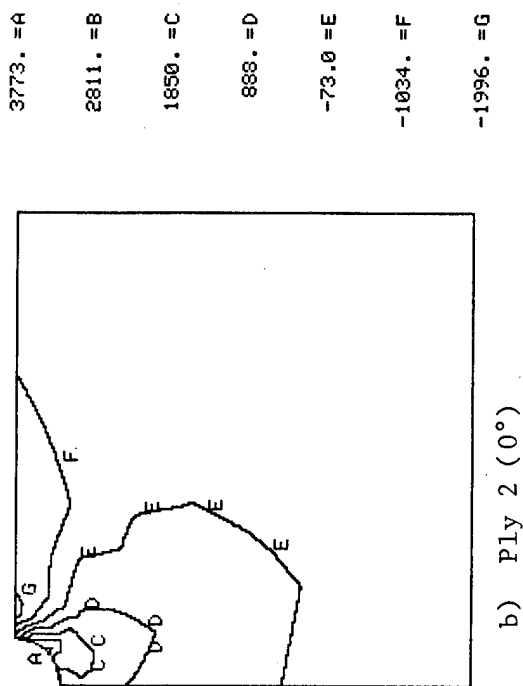
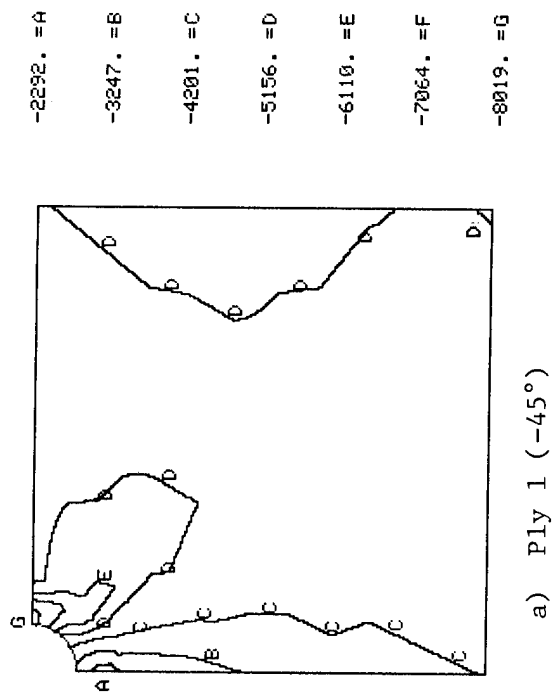


Figure 55. In-Plane Shear Stresses ( $\tau_{12}$ , psi) in Selected Plies after -54.7 ksi Axial Compressive Loading; 1%M Moisture Absorption.

To summarize, the addition of one weight percent moisture prior to loading results in lower axial compressive stresses, but higher transverse tensile stresses. The ultimate strengths are also lower. Hence, the ultimate strength of the composite laminate could remain about the same, or possibly be even slightly higher, as indicated by the experimental data of Reference [4].

## SECTION 8

### DISCUSSION OF ANALYTICAL/EXPERIMENTAL CORRELATIONS

Three distinct geometries have been modeled here, as presented in Sections 5, 6 and 7. These include 2.9 percent microporosity in the unidirectional ply material (Section 5), 0° ply drop-offs in the F-18 laminate (Section 6), and a hole in the F-18 laminate (Section 7). The latter two geometries were assumed to be axially compressive loaded at both RTD and RTW conditions. The microporosity model was subjected to longitudinal and transverse tensile and longitudinal shear loadings, but only at RTD conditions.

These various geometry, environmental, and loading conditions were selected to demonstrate the capabilities of the analyses currently available. Development of the analysis techniques themselves occupied most of the available time, this being an ongoing effort. Nevertheless, some correlations with available experimental data of the results predicted here can be made. These will be addressed separately for the three different geometries analyzed.

#### 8.1 Microporosity

Longitudinal and transverse tensile and longitudinal shear loadings were applied to models without and with porosity. These loadings were applied only for room temperature, dry (RTD) conditions, with cooldown-induced curing residual thermal stresses being included.

##### 8.1.1 Longitudinal Tensile Loading

In the absence of microporosity, local yielding was predicted to first occur at an applied longitudinal tensile stress of 120 ksi (Figure 20). A proportional limit stress was not included in any of the reports of experimental data (References [1-4]), presumably because none was observed, the unidirectional composite responding linearly up to the point of gross fracture. This is consistent with the present predictions, the matrix yielding being very localized and the fibers dominating the composite stress-strain response. At 250 ksi, no matrix

microcracking had yet occurred (Figure 20d), and at 318 ksi gross fracture was predicted to occur. This is somewhat higher than the experimental values of 235 ksi [1], 253 ksi [2], and 264 ksi [4] reported. However, the reason is obvious; a fiber tensile strength of 520 ksi was assumed in the present analysis (see Section 4 for values of fiber and matrix properties assumed). This is higher than experimental values reported previously, viz, 450 ksi [1], 466 ksi [2], and currently 516 ksi [4]. The predicted composite strength of 318 ksi essentially corresponds to the rule of mixtures prediction, as expected. Experimental values of this magnitude are currently being measured.

The addition of 2.9 percent microporosity was predicted to have essentially no influence on longitudinal tensile strength. However, the experimentally measured values indicated a 21 percent reduction due to 2.1 to 3.1 percent voids [3]. As indicated by the photomicrographs in Appendix B of Reference [3], this porosity was primarily in the form of macrovoids at prepreg ply interfaces. Whether modeling this macroporosity would result in a predicted longitudinal strength reduction is not known at present. This is proposed as a future investigation.

#### 8.1.2 Transverse Tensile Loading

As presented in Section 4, and discussed in Section 5, the tensile strength of the matrix used in the present analysis, i.e., 28.7 ksi, was based upon solid rod torsion (shear) testing of the neat Hercules 3501-6 epoxy matrix. Actual tensile testing results in much lower values, viz, about 8.8 ksi (see Section 5). This is a factor of 3.25 times less. The high value was used in the present analysis to be consistent with the concept of using octahedral shear yield and failure criteria, which implies that pure shear or uniaxial tensile input data should give equivalent results. The corresponding predictions of composite transverse strength imply that this is not true. Thus, for the present correlation purposes it is perhaps more realistic to reduce the composite strength predictions by a factor of 3.25 also, reflecting the use of a more realistic epoxy matrix tensile strength in the analysis. Thus, all volumes quoted here will be reduced by a factor of 3.25 from those given in Section 5.

First yielding of the matrix was predicted to occur at very low

levels of applied transverse tensile stress. However, for the nonporous composite model, first microcracking occurred at 4.70 ksi, at a fiber-matrix interface (Figure 22c). This crack continued to grow slowly around the interface with increasing applied stress. However, at 7.43 ksi it abruptly spread across the entire cross section, defining fracture of the composite.

Experimental values of the transverse tensile strength of a nonporous AS/3501-6 graphite/epoxy composite ranged from 5.48 ksi [3] to 10.4 ksi [2]. Three different sets of data given in Reference [1] resulted in averages of 6.02, 6.91 and 7.52 ksi, respectively, while another set in Reference [2] indicated 7.97 ksi. Hence, the predicted value of 7.43 ksi given here is within the scatter of the available experimental data and correlates well.

The porous composite model predicted first microcracking at 3.70 ksi, at the fiber-matrix interface near the pore (see Figure 23b). This cracking also extended slowly, with an abrupt total failure occurring at 6.77 ksi. Thus, the 2.9 percent microporosity induced a predicted 9 percent reduction in transverse tensile strength. The experimental data (see Table 9 of Reference [3]) indicated a 21 percent reduction, although as noted on Page 20 of Reference [3] this value was believed to be an overestimation, because of specimen gripping problems. The measured void volume was 2.12 percent as measured by chemical analysis, and 3.06 percent by image analysis.

The indication is that the present analysis of porosity does provide reasonable predictions. However, different pore geometries and porosities should be analyzed before detailed conclusions are drawn. Also, many more experimental data are needed, for a range of porosities, and for different environmental conditions. Presently only RTD test data were available for correlation purposes.

#### 8.1.3 Longitudinal Shear Loading

Since actual shear (solid rod torsion) test data for the Hercules 3501-6 epoxy were used as input to the analysis (as discussed in Section 4), no corrections should be necessary in making correlations with composite shear properties data.

For the nonporous composite, first yielding of the epoxy matrix was predicted to occur at very low values of applied longitudinal shear

stress. At 7.18 ksi extensive yielding and microcracking had occurred (Figure 25c). Complete fracture was predicted at 8.64 ksi. For reference (from Section 4), the matrix shear yield stress is 5.51 ksi, and the shear ultimate is 16.57 ksi.

Measured longitudinal shear strengths at the RTD condition were typically 18.1 ksi [1] to 18.9 ksi [2], with one set of data averaging 20.1 ksi being reported [2]. Thus, the present prediction of 8.64 ksi is only about one-half the average measured value. The reason for this difference is not known at present. However, it may be associated with the fact that the model predicts interface debonding at relatively low applied shear stress levels; this may not occur in the actual material. A different failure criterion which would retard this failure would lead to higher strength predictions.

It also will be noted that the measured composite shear strength (approximately 18.5 ksi) is higher than the matrix shear strength measured (16.6 ksi). This is possible, the fiber being assumed to be about 17 times stiffer in longitudinal shear than the matrix, and therefore capable of carrying a high percentage of the shear loading. Also, the inelastic stress concentrations should be low because of the high degree of nonlinear shear stress-strain response exhibited by the epoxy matrix (see Section 4). However, it is suspected that the high composite shear strength relative to the matrix shear strength is actually due to the influence of the triaxial stress state in the composite, which tends to suppress shear failure. Much of this stress is undoubtedly due to cooldown from the cure temperature, which primarily induces normal stresses rather than shear stresses.

The correlation of micromechanics predictions with experimental data for longitudinal shear loadings of Hercules AS/3501-6 graphite/epoxy, and S glass fibers in the same 3501-6 epoxy matrix, was previously attempted in Reference [5]. No crack propagation capability was available at that time; only first microcrack initiation could be predicted. The same analysis was also used in Reference [2] to model the compressive loading of  $[\pm 45]_{4s}$  AS/3501-6 graphite/epoxy laminates. This is also a longitudinal shear stress-dominated condition. In all cases, the micromechanics analysis predicted a relatively low stress to cause first failure. At the time it was assumed that significant additional

applied stress would be required to cause total failure. Now that it is possible to model total failure via crack propagation, as included here, it can be seen that this is not true.

Obviously, more work needs to be done. Fortunately, we now have the micromechanics analysis tools required to do so, and significant progress should be made in the near future. Currently, however, the micromechanics analysis clearly underpredicts unidirectional composite longitudinal shear strength.

The principal concern of the present discussion is how porosity in the composite affects shear strength. As discussed in Section 5, the micromechanics analysis predicts no effect. Unfortunately no direct shear testing of porous unidirectional composites was performed. However, tensile tests of  $[\pm 45]_{6s}$  laminates were included in the study of Reference [2], this being an indirect measure of shear response. As presented in Table 9 of Reference [3], the porous composite (1.49 percent porosity by chemical analysis, 2.31 percent by image analysis) was actually 11 percent stronger than a nonporous composite.

#### 8.1.4 Summary of Microporosity Results

The present micromechanics analysis does not predict the experimentally observed influence of porosity on longitudinal tensile strength. However, it does predict, at least qualitatively, its influence on transverse tensile and longitudinal shear strengths.

The present study has provided significant additional insight into the strengths and weaknesses of current micromechanics analyses, and has suggested directions for additional study. It is clear that steady progress is being made toward the goal of being able to accurately predict the strength of unidirectional composites for any combination of constituent materials, environmental conditions, and loadings. Micromechanics analyses are already very useful tools in understanding unidirectional composite response, and with continued development they will undoubtedly be capable of replacing much of the time consuming and costly testing which currently must be done.

#### 8.2 Laminate with Ply Drop-Offs

As presented in Section 6, a 3-D finite element analysis of the F-18 laminate containing two  $0^\circ$  ply drop-offs and subjected to an axial compressive loading was performed, for both RTD and RTW conditions.



For the RTD condition, the experimentally measured average axial compressive strength was -98.6 ksi (Table 5.2 of Reference [2]). The predicted internal stress states presented in Section 6 of the present report were for a loading of -41.6 ksi, i.e., about 42 percent of ultimate. As discussed in Section 6 of Reference [1], the predicted critical stress in the F-18 laminate not containing ply drop-offs was the  $\sigma_{11}$  stress in the  $0^\circ$  plies. As noted in Section 6 of the present report, in the presence of  $0^\circ$  ply drop-offs this was still predicted to be the case, the stresses in the  $45^\circ$  and  $90^\circ$  plies not dictating composite failure. Thus, scaling the analytically applied stress of -41.6 ksi up from the 42 percent level to ultimate results in the  $\sigma_{11}$  stresses in the  $0^\circ$  plies increasing from -101.3 ksi to about -202 ksi (taking into account the pre-existing -28.4 ksi curing residual stress). This is about 15 percent higher than the experimentally measured axial compressive strength of a unidirectional ply (see Table 5 in Section 6). This is also generally consistent with the rule-of-mixtures prediction presented in Table 19 of Reference [3]. That is, the presence of  $0^\circ$  ply drop-offs is predicted to not degrade the RTD longitudinal compressive strength of the F-18 laminate, just as was experimentally observed (see Figure 2.1 of Reference [2]).

For the RTW condition, the experimentally measured average axial compressive strength was -97.2 ksi, i.e., about the same as for the RTD condition. As discussed in Section 6.3.3.2, the moisture-induced residual stresses in the  $0^\circ$  plies were favorable for successive compressive loading, so that at failure the  $\sigma_{11}$  stresses were predicted to actually be about 20 ksi lower than for the RTD case. This explains why the RTW strength was equal to the RTD strength, even though the unidirectional ply axial compressive strength was about 7 percent lower than the corresponding RTD value (as indicated in Table 5).

It should be noted that the axial compressive stress in the neat resin pocket at the end of the dropped-off ply was predicted to be very high. However, since this material has low stiffness and strength, its failure early in the axial loading process would be expected to not influence composite gross failure.

Also, the interlaminar stresses induced by the ply drop-offs were predicted to be very low, further explaining why the simple rule-of-

mixture predictions of Reference [3] were so accurate.

In summary, the more detailed ply drop-off analysis performed here supports that of Reference [3] in predicting little influence of 0° ply drop-offs, and offers clear insights as to why they are not detrimental, which is one primary purpose of performing an analysis. The available experimental data, while correlating well with the analytical predictions, offer no insight as to what the influence of other drop-off patterns or loading conditions would be. This is the virtue of an analysis; once it has been correlated with available experimental data, it can be used to predict the response for other conditions, with good confidence.

### 8.3 Laminate with Hole

The experimental data indicated that the presence of a 0.188 inch diameter hole in the 2 inch wide F-18 laminate test specimen significantly reduced its axial compressive strength. Only F-18 laminates containing 0° ply drop-offs were tested, and only in the RTW condition, the hole when present being centered on the ply drop-off region [4]. For this condition, the ply drop-off laminate without a hole, and without porosity, exhibited an average stress in the 30-ply thick region of -104 ksi at failure (see Table 14 of Reference [4]). With a hole present, this stress was -67.9 ksi, a 35 percent reduction. Since the ply drop-off itself was shown to not reduce the laminate compressive strength, it will be assumed that this 35 percent strength decrease was due to the hole itself. This is further supported by the fact that in the presence of both ply drop-offs and porosity, the decrease due to a hole was also of this same magnitude (Table 14 of Reference [4]).

In the present analysis, only the hole was modeled, i.e., no ply drop-offs or porosity were included simultaneously.

The laminate containing a hole was loaded up to -54.7 ksi, as discussed in Section 7, which corresponds to 81 percent of the experimentally measured strength of -67.9 ksi. At this applied axial compressive stress, the highest  $\sigma_{11}$  stresses in the 0° plies were predicted to be -114.2 ksi. Scaled up to the measured applied stress, these stresses would be -142 ksi, which correlates reasonably well with the -163 ksi axial compressive strength of a unidirectional ply at RTW

conditions (Table 5). The transverse tensile stresses  $\sigma_{22}$  at the hole in these same  $0^\circ$  plies were also relatively high, predicted to be 13.7 ksi at the experimentally measured axial compressive strength of -67.9 ksi. As indicated in Table 5, the transverse tensile ultimate strength of this material at RTW conditions is only about 6 ksi.

Thus, the analysis predicts transverse tensile failures of the  $0^\circ$  plies near the surface of the hole as the initial failure. This would be immediately followed by fiber microbuckling in this same material due to the loss of lateral support and the high axial compressive stresses already present. The high shear stresses developed in the  $45^\circ$  plies would then cause these plies to fail.

Although no experimental data were available in Reference [4] for correlation, the present analysis predicts (see Section 7) essentially the same composite response for the RTD condition. The less favorable residual stresses lead to higher  $0^\circ$  ply stresses when an axial compressive loading is applied to the dry laminate, but the strength allowables are also higher.

In summary, the present analysis does adequately estimate the approximately 35 percent strength reduction of the F-18 laminate due to the presence of a hole, as determined experimentally, at least for the available experimental data for RTW conditions.

## SECTION 9

### CONCLUSIONS

Both 2-D and 3-D finite element analyses were used to predict composite response to microporosity, ply drop-offs and holes. It was demonstrated that, while much more development work needs to be done, even the existing analyses can provide valuable insights into the mechanisms of composite response, including failure models. The limitations of these present analytical models are well understood, and techniques for improving them are known. With additional time and effort, these analyses can be made as rigorous and as accurate as required for the application. This is true because the finite element approach models the physical problem directly. For example, if a mode of failure is fiber-matrix debonding, the model includes this failure mechanism directly, as the initiation and propagation of a crack. If a ply drop-off is present, the actual physical geometry is modeled, even to the extent of scaling dimensions from photomicrographs of cross sections.

The numerical results presented in this report, although somewhat cursory and making use of simple 3-D grid representations, have demonstrated the utility of these analyses. For example, the experimental observations of lack of sensitivity of laminate compressive strength to  $0^\circ$  ply drop-offs, and the strong sensitivity to the presence of a hole, were well supported by the respective analyses. The analysis of the ply drop-offs predicted little influence of their presence. It also predicted that the laminate containing the  $0^\circ$  ply drop-offs should have about the same compressive strength in either the room temperature wet or dry states, which was also correlated experimentally. This suggests that the analysis could also be used to predict composite response for other environmental conditions or other ply drop-off configurations of potential design interest, but which were not tested experimentally.

Likewise, since the predicted strength reduction due to the presence of a round hole in a specific laminate correlated well with available experimental data, there is reason to expect that the same analysis could be used with confidence to model other cutout geometries, laminate configurations, loading conditions, and environments.

The analysis of microporosity was perhaps the most interesting of all. It permitted a 2-D analysis and hence a very refined grid representation, and also crack initiation and propagation. Thus, it was a very physically realistic model. Only one assumed micropore geometry was studied here, as a demonstration of feasibility. Yet the predicted loss of transverse strength due to porosity correlated with the measured response very well. Likewise, neither the analysis nor available experimental data indicated a loss of longitudinal shear strength due to porosity.

In summary, while much more analytical work needs to be done, the preliminary results presented here clearly indicate the value of even the existing analytical tools in understanding the response of composites to variations of geometry, loading, and environment.

## SECTION 10

### REFERENCES

1. Grimes, G.C. and Adams, D.F., "Investigation of Compression Fatigue Properties of Advanced Composites," Northrop Technical Report NOR 79-17, Contracts N00019-77-C-0518 and N00019-77-C-0519 with the Naval Air Systems Command, October 1979.
2. Grimes, G.C., Adams, D.F. and Dusablon, E.G., "The Effects of Discontinuities on Compression Fatigue Properties of Advanced Composites," Northrop Technical Report NOR 80-158, Contracts N00019-79-C-0275 and N00019-79-C-0276 with the Naval Air Systems Command, October 1980.
3. Ramkumar, R.L., Grimes, G.C., Adams, D.F. and Dusablon, E.G., "Effects of Materials and Processes Defects on the Compression Properties of Advanced Composites," Northrop Technical Report NOR 82-103, Contracts N00019-80-C-0484 and N00019-80-C-0490 with the Naval Air Systems Command, May 1982.
4. Ramkumar, R.L. and Adams, D.F., "Compression Properties of Porous Laminates in the Presence of Ply Drop-Offs and Fastener Holes," Northrop Technical Report NOR 84-1, Contracts N00019-82-C-0156 and N00019-82-C-0063 with the Naval Air Systems Command, March 1984.
5. Crane, D.A. and Adams, D.F., "Finite Element Micromechanical Analysis of a Unidirectional Composite Including Longitudinal Shear Loading," Report UWME-DR-101-101-1, University of Wyoming, Department of Mechanical Engineering, February 1981.
6. Murphy, D.P. and Adams, D.F., "Energy Absorption Mechanisms During Crack Propagation in Metal Matrix Composites," Report UWME-DR-901-103-1, University of Wyoming, Department of Mechanical Engineering, October 1979.
7. Miller, A.K. and Adams, D.F., "Micromechanical Aspects of the Environmental Behavior of Composite Materials," Report UWME-DR-701-111-1, University of Wyoming, Department of Mechanical Engineering, January 1977.
8. Miller, A.K. and Adams, D.F., "Inelastic Finite Element Analysis of a Heterogeneous Medium Exhibiting Temperature and Moisture Dependent Material Properties," Fibre Science and Technology, Vol. 13, No. 2, March-April 1980, pp. 135-153.

9. Monib, M.M. and Adams, D.F., "Three-Dimensional Elastoplastic Finite Element Analysis of Laminated Composites," Report UWME-DR-001-102-1, University of Wyoming, Department of Mechanical Engineering, November 1980.
10. Adams, D.F., "Inelastic Analysis of a Unidirectional Composite Subjected to Transverse Normal Loading," Report No. RM-6245-PR, The Rand Corporation, May 1970.
11. Adams, D.F. and Tsai, S.W., "The Influence of Random Filament Packing on the Transverse Stiffness of Unidirectional Composites," Journal of Composite Materials, Vol. 3, July 1969, pp. 368-381.
12. "Hercules Magnamite Graphite Fibers," Hercules Incorporated, Wilmington, Delaware, 1978.
13. Adams, D.F., "Temperature and Moisture Induced Stresses at the Fiber/Matrix Interface in Various Composite Materials," Proceedings of the 24 National SAMPE Symposium and Exhibition, San Francisco, California, May 1979.
14. Unpublished Experimental Data for Hercules 3501-6 Epoxy Matrix, Composite Materials Research Group, Department of Mechanical Engineering, University of Wyoming.
15. Cairns, D.S. and Adams, D.F., "Moisture and Thermal Expansion of Composite Materials," Report UWME-DR-101-104-1, University of Wyoming, Department of Mechanical Engineering, November 1981.
16. Richard, R.M. and Blacklock, R.J., "Finite Element Analysis of Inelastic Structures," AIAA Journal, Vol. 7, No. 3, March 1969, pp. 432-438.
17. Boresi, A.P., Sidebottom, O.M., Seely, F.B., and Smith, J.O., Advanced Mechanics of Materials, Third Edition, John Wiley and Sons, New York, 1978.
18. Hill, R., The Mathematical Theory of Plasticity, Oxford University Press, London, England, 1950.
19. Forray, M.J., Variational Calculus in Science and Engineering, McGraw-Hill Book Co., New York, 1968.

DISTRIBUTION LIST

|   | <u>No. of Copies</u> |
|---|----------------------|
| Naval Air Systems Command<br>ATTN: Code AIR-5304C<br>Washington, DC 20361   | 8                    |
| Office of Naval Research<br>(Code 472)<br>Washington, DC 20350  | 1                    |
| Office of Naval Research, Boston<br>495 Summer St.<br>Boston, MA 02210<br>ATTN: Dr. L. H. Peebles   | 1                    |
| Naval Research Laboratory<br>Codes 6306 and 6120<br>Washington, DC 20350  | 2                    |
| Naval Surface Weapons Center<br>Code R-31<br>White Oak, Silver Spring, MD 20910   | 1                    |
| Naval Air Propulsion Test Center<br>ATTN: J. Glatz<br>Trenton, NJ 08628   | 1                    |
| Commander<br>U.S. Naval Weapons Center<br>China Lake, CA 92555  | 1                    |
| Naval Ship R&D Center<br>ATTN: Mr. M. Krenzke, Code 727<br>Washington, DC   | 1                    |
| Naval Sea Systems Command<br>Navy Dept. Codes 05R and 05D23<br>Washington, DC 20360   | 2                    |
| Commander<br>Naval Air Development Center<br>ATTN: Aero Materials Laboratory<br>Aero Structures Division<br>Radomes Section<br>Warminster, PA 18974 | 3                    |



DISTRIBUTION LIST (Cont'd)

Page 2 of 6

No. of Copies

|   |   |
|---|---|
| Air Force Materials Laboratory<br>ATTN: Codes LC (1 copy)<br>LN ( " " )<br>LTF ( " " )<br>LAE ( " " )<br>Wright-Patterson AFB, OH 45433 | 4 |
| Air Force Flight Dynamics Laboratory<br>ATTN: Code FDTC<br>Wright-Patterson AFB, OH 45433   | 1 |
| U.S. Applied Technology Laboratory<br>U.S. Army Development Laboratories (AVRADCOM)<br>ATTN: DAVDL-ATL-ATS<br>Fort Eustis, VA 23604     | 1 |
| Director<br>Plastics Technical Evaluation Center<br>Picatinny Arsenal<br>Dover, NJ 07801  | 1 |
| Department of the Army<br>Army Materials & Mechanics Research Center<br>Watertown, MA 02172   | 1 |
| NASA<br>Langley Research Center<br>Hampton, VA 23665  | 1 |
| NASA Headquarters<br>Code RV-2 (Mr. N. Mayer)<br>600 Independence Ave., SW<br>Washington, DC 20546                                      | 1 |
| AVCO Corporation<br>Applied Technology Division<br>Lowell, MA 01851   | 1 |
| Bell Aerospace Co.<br>ATTN: Mr. F. M. Anthony<br>Buffalo, NY 14240  | 1 |
| The Boeing Company<br>Aerospace Division<br>P.O. Box 3707<br>Seattle, WA 98124  | 1 |
| Boeing-Vertol Co.<br>P.O. Box 16858<br>ATTN: Dept. 1951<br>Philadelphia, PA 19142   | 1 |

DISTRIBUTION LIST (Cont'd)

Page 3 of 6

No. of Copies

Defense Ceramic Information Center  
Battelle Memorial Institute  
505 King Ave.  
Columbus, OH 43201

1

E. I. DuPont de Nemours & Co.  
Textile Fibers Dept.  
Wilmington, DE 19898

1

General Dynamics  
Convair Aerospace Division  
ATTN: Tech Library  
P.O. Box 748  
Ft. Worth, TX 76101

1

General Dynamics  
Convair Division  
ATTN: Mr. W. Sheck; Dept. 572-10  
P.O. Box 1128  
San Diego, CA 92138

1

General Electric  
R&D Center  
ATTN: Mr. W. Hillig  
Box 8  
Schnectady, NY 12301

1

General Electric Company  
Valley Forge Space Center  
Philadelphia, PA 19101

1

B. F. Goodrich Aerospace & Defense Products  
500 South Main St.  
Akron, OH 44318

1

Great Lakes Research Corporation  
P.O. Box 1031  
Elizabethton, TN

1

Grumman Aerospace Corp.  
ATTN: Mr. G. Lubin  
Bethpage, LI, NY 11714

1

Hercules Incorporated  
ATTN: Mr. E. G. Crossland  
Magna, UT 84044

1

HITCO  
1600 W. 135th St.  
Gardena, CA 90406

1

DISTRIBUTION LIST (Cont'd)

Page 4 of 6

No. of Copies

Illinois Institute of Technology  
Research Center  
ATTN: Dr. K. Hofer  
10 West 35 St.  
Chicago, IL 60616

1

Lockheed California Co.  
ATTN: Library  
Box 551  
Burbank, CA 91520

1

Lockheed-Georgia, Co.  
ATTN: Mr. L. E. Meade  
Marietta, GA 30063

1

Material Sciences Corporation  
Gwynedd Plaza II, Bethlehem Pike  
Spring House, PA 19477

1

McDonnell Douglas Corp.  
McDonnell Aircraft Co.  
ATTN: Library  
P.O. Box 516  
St. Louis, MO 63166

1

McDonnell-Douglas Corp.  
Douglas Aircraft Co.  
ATTN: Library  
3855 Lakewood Blvd.  
Long Beach, CA 90801

1

Northrop Corporation  
Aircraft Division  
One Northrop Avenue  
ATTN: Library; 3360/82  
Hawthorne, CA 90250

Rockwell International Corp.  
ATTN: Library  
12214 Lakewood Blvd.  
Downey, CA 90241

1

Stanford Research Institute  
ATTN: Library  
333 Ravenswood Ave., Bldg. 102B  
Marlo Park, CA 94025

1

TRW, Inc  
Systems Group  
One Space Park, Bldg. 01; Rm. 2171  
Redondo Beach, CA 90278

1

DISTRIBUTION LIST (Cont'd)

Page 5 of 6

|   | <u>No. of Copies</u> |
|---|----------------------|
| United Aircraft Corporation<br>Pratt & Whitney Aircraft Division<br>East Hartford, CT 06108                       | 1                    |
| United Aircraft Corporation<br>Sikorsky Aircraft Division<br>ATTN: Library<br>Stratford, CT 06602                 | 1                    |
| University of California<br>Lawrence Livermore Laboratory<br>ATTN: Library<br>P.O. Box 808<br>Livermore, CA 94550 | 1                    |
| University of Wyoming<br>Mechanical Engineering Dept.<br>ATTN: Dr. D. F. Adams<br>Laramie, WY 92071               | 1                    |
| Westinghouse R&D Center<br>ATTN: Library<br>1310 Beulah Road<br>Churchill Boro<br>Pittsburgh, PA 15235            | 1                    |
| Robert A. Signorelli<br>Mail Stop 106-1<br>NASA Lewis Research Center<br>Cleveland, OH 44135                      | 1                    |
| Dr. C. C. Chamis, Mat'ls & Struct. Div.<br>NASA Lewis Research Center<br>Cleveland, OH 44135                      | 1                    |
| LTV Aerospace Corp.<br>ATTN: Library<br>P.O. Box 5003<br>Dallas, TX 75222   | 1                    |
| Rockwell International<br>ATTN: Dr. L. M. Lackman<br>L. A. International Airport<br>Los Angeles, CA 90009         | 1                    |
| Air Force Flight Dynamics Lab.<br>ATTN: Dr. G. P. Sendekji/FBE<br>Wright-Patterson AFB, OH 45433                  | 1                    |

DISTRIBUTION LIST (Cont'd)

Page of 6 of 6

No. of Copies

Air Force Materials Lab.  
ATTN: Dr. J. M. Whitney/MBM  
Wright-Patterson AFB, OH 45433

1

Southwest Research Institute  
ATTN: Library  
Box 28510  
San Antonio, TX 78284

1

Vought Corporation  
Advanced Technology Center, Inc.  
ATTN: J. W. Renton  
P.O. Box 6144  
Dallas, TX 75222

1

Hughes Helicopter  
ATTN: Chief Librarian  
Centinela & Teale Sts.  
Culver City, CA 90230

1

Bell Helicopter  
ATTN: Library  
Fort Worth, TX 76101

1